UNIVERSIDAD NACIONAL AUTÓNOMA DE MÉXICO

PROGRAMA DE MAESTRÍA Y DOCTORADO EN INGENIERÍA
INGENIERÍA ELÉCTRICA - SISTEMAS ELÉCTRICOS DE POTENCIA

COORDINATED CONTROL SCHEME FOR VOLTAGE AND FREQUENCY SUPPORT IN MODERN POWER GRIDS VIA SMART MONITORING AND BATTERY-BASED POWER CONVERTERS

TESIS

QUE PARA OPTAR POR EL GRADO DE:

DOCTOR EN INGENIERÍA

PRESENTA

M.Eng GABRIEL EDUARDO MEJÍA RUIZ

TUTOR PRINCIPAL

Dr. MARIO ROBERTO ARRIETA PATERNINA, FI-UNAM

COMITÉ TUTOR

Dra. MARÍA HERLINDA MONTIEL SÁNCHEZ, ICAT-UNAM

Dr. VICENTE TORRES GARCÍA, FI-UNAM

Dr. RAFAEL ESCARELA PÉREZ, UAM

CIUDAD DE MÉXICO, SEPTIEMBRE 2022

JURADO ASIGNADO:

Presidente: DR. RAFAEL ESCARELA PÉREZ

Secretario: DRA. MARÍA HERLINDA MONTIEL SÁNCHEZ

1er. Vocal: DR. MARIO ROBERTO ARRIETA PATERNINA

2do. Vocal: DR. CLAUDIO ADRIÁN CAÑIZARES ESGUERRA

3er. Vocal: DR. JUAN RAMÓN RODRÍGUEZ RODRÍGUEZ

Lugares donde se realizó la tesis:
FACULTAD DE INGENIERÍA, UNAM, CIUDAD DE MÉXICO, MÉXICO.

TUTOR DE TESIS:

Dr. MARIO ROBERTO ARRIETA PATERNINA

FIRMA

Acknowledgments

Primarily, I would like to express my infinite gratitude to my beloved wife and my admirable son, their genuine love was the necessary source of energy to complete this chapter of my life. Your company and support have been an invaluable source of motivation. Thanks for your understanding in these 3 years of the effort, dedication and discipline needed to successfully achieve this great accomplishment.

I would like to express my most sincere gratitude to my research advisor, Dr. Mario R. Arrieta Paternina. In my opinion, He is a competent professional, as well as a friend. I greatly appreciate your support and teachings shared with patience and enthusiasm. His guidance has significantly enhanced my academic skills and research habits. I continue to be inspired by his meticulous attention to detail and systematic approach to solve problems, focusing effort on the results, but simultaneously promoting a deep understanding of the theoretical background. His contributions, useful discussions and pragmatism have helped many ideas become reality. Thanks to our joint efforts, we clarified several ideas, that later with hard work, we materialized into research results published in high-impact journals.

I would like to extend my gratitude to the committee members and assigned jury: Dra. Montiel, Dr. Cañizares, Dr. Rodríguez, Dr. Torres and Dr. Escarela, their critical and perspicacious, yet constructive comments were very helpful in guiding and improving my research. I would also like to thank Dr. Rafael Segundo and Dr. Petr Korba, who received me with kindness at the facilities of the Zurich University of Applied Science (ZHAW) for an academic stay.

Finally but not least, I thank to the program in Engineering-Doctorate at the National Autonomous University of Mexico (UNAM) and CONACYT for the scholarship under grant (1044979). Also, I acknowledge financial support from the Project Support Program for Research and Technological Innovation of UNAM (DGAPA, PAPIIT-2021) through the project TA101421.

Abstract

This research addresses the development of a novel optimal real-time control framework to provide voltage regulation in distribution networks and frequency/voltage support in transmission networks with a response time in a milliseconds-scale, exploiting the time-synchronized measurements and battery-based systems. This approach takes advantage of the fast and accurate injection of active and reactive power from battery-based systems and grid-connected power converters to provide ancillary services, enhancing the stability and reliability of modern power grids. In this control approach, battery-based systems are grouped according to their geographical location to cooperate with the power system operator and an optimal controller in a hierarchical and scalable scheme.

This proposal incorporates a new aggregator agent that executes logical rules to compute the active and reactive power commands to be injected for each battery-based system. These set-points are based on the operating constraints, the injection capacity of each battery system and the estimated optimal control action for each network area. The inclusion of these logical rules reduces the utilization of batteries extending its lifespan and locally mitigates imbalances between supply and demand, reducing disturbances in neighboring areas. At the same time, the proposed logic architecture reduces the latency and computational burden of the conventional central controller.

The eigensystem realization algorithm (ERA) is applied to estimate the linear model state-space representation for each network area to be controlled. This investigation also adopts a structure of the multi-input multi-output linear quadratic Gaussian (LQG) controller which is tuned considering the identified model by the ERA method, then this strategy allows to estimate the optimal active and reactive power to be injected by the clustered set of battery systems per area.

This manuscript reports the application of the proposed approach in several study cases, including the implementation of the proposed controller to support frequency and voltage in multi-area transmission networks, integrating battery energy storage systems (BESSs). For this purpose, simulated scenarios with significant load changes and three-phase three-cycle faults on a modified Kundur-system with four interconnected areas were implemented, mitigating with timeliness and accuracy frequency and voltage contingencies in less than 450ms.

This research also presents the application of the proposed control approach for the coordinated injection of reactive power from multiple off-board electrical vehicles (EVs) chargers to improve the voltage profile of highly unbalanced distribution grids (DGs). Simulated scenarios with unbalanced faults, latency in communications, and highly unbalanced loads conditions on the IEEE 13 and 123 nodes test feeders were employed to exhibit the coherency between the theoretical analyses and results. An additional study case evidences the application of the proposed control scheme to increase the operational flexibility of active DGs by exploiting the potential of EVs chargers to decongest the grid and increase the grid capacity.

The results and contributions reported in this research have been published in several papers and book chapters. Accordingly, this manuscript presents a compendium of these previously published and peer-reviewed writings.

Resumen

Esta investigación aborda el desarrollo un novedoso marco de control óptimo en tiempo real para proporcionar regulación de la tensión en las redes de distribución y soportar la frecuencia/tensión en las redes de transmisión con un tiempo de respuesta en una escala de milisegundos, aprovechando las mediciones sincronizadas en el tiempo y las fuentes de energia distribuidas basadas en baterías. Este enfoque se beneficia de la inyección rápida y precisa de potencia activa y reactiva de los sistemas de baterías basados en convertidores de potencia conectados a la red para proporcionar servicios auxiliares, mejorando la estabilidad y la confiabilidad de las redes eléctricas modernas. En este enfoque de control, los sistemas basados en baterías se agrupan según su ubicación geográfica para cooperar con el operador del sistema eléctrico y un controlador óptimo en un esquema jerárquico y escalable.

Esta propuesta incorpora un nuevo agente agregador que ejecuta reglas lógicas para calcular las consignas de potencia activa y reactiva a inyectar por cada sistema de baterías. Estas consignas se basan en las restricciones de funcionamiento, la capacidad de inyección de cada sistema de baterías y la acción de control óptima estimada para cada área de la red. La inclusión de estas reglas lógicas reduce la utilización de las baterías para prolongar su vida útil y mitigar localmente los desequilibrios entre la oferta y la demanda, reduciendo las perturbaciones en las areas vecinas. Al mismo tiempo, la arquitectura lógica propuesta reduce la latencia y la carga computacional en comparación con el controlador central convencional.

El algoritmo de realización del eigensistema (ERA) se aplica para estimar la representación del espacio de estados del modelo lineal para cada una de las areas de la red que se desea controlar. Esta investigación también adopta una estructura del controlador lineal cuadrático gaussiano (LQG) de múltiples entradas y múltiples salidas sintonizado con base en el modelo identificado por el método ERA, luego esta estrategia permite estimar la potencia activa y reactiva óptima a ser inyectada por el conjunto agrupado de sistemas de baterías en cada área.

Este manuscrito reporta la aplicación del enfoque propuesto en varios casos de estudio, dentro de los que se incluye la implementación del controlador propuesto para soportar la frecuencia y el voltaje en redes de transmisión multi-área, integrando sistemas de almacenamiento de energía en baterías (BESSs). Para ello, se implementaron escenarios simulados con cambios de carga significativos y fallas trifásicas en el sistema de prueba Kundur modificado con cuatro áreas interconectadas, mitigando con precisión las contingencias de frecuencia y tensión en menos de 450ms.

Esta investigación tambien presenta la aplicación del enfoque de control propuesto para la inyección coordinada de potencia reactiva desde múltiples cargadores de vehículos eléctricos para mejorar el perfil de tensión de las redes de distribución altamente desequilibradas. Para demostrar la coherencia entre los análisis teóricos y los resultados, se emplearon escenarios simulados con fallas trifasicas desequilibradas, latencia en las comunicaciones y condiciones de cargas altamente desbalanceadas en los alimentadores de prueba de 13 nodos y 123 nodos de la IEEE. Un estudio de caso adicional pone de manifiesto la aplicación del esquema de control propuesto para aumentar la flexibilidad operativa de las redes de distribución aprovechando el potencial de los cargadores de vehiculos electricos para descongestionar la red y aumentar su capacidad.

Los resultados y contribuciones reportados en esta investigación se han publicado en varios artículos y capítulos de libros. En consecuencia, este manuscrito presenta un compendio de estos escritos previamente publicados y revisados por pares academicos.

Contents

List of Figures

LIST OF FIGURES

LIST OF FIGURES

List of Tables

Nomenclature

Abbreviations

ADG	Active distribution grid	LQE	Linear quadratic estimator
AGC	Automatic generation control	LQG	Linear quadratic gaussian controller
ARE	Algebraic Riccati equation	LQR	Linear quadratic regulator
BESS	Battery energy storage system	MIMO	Multiple-input, multiple-output
BMS	Battery management system	OLTC	On-load tap changer
DAB	Dual active bridge	PCC	Point of common coupling
DER	Distributed energy resources	PLL	Phase-locked loop system
D-PMU	Distribution-level PMU	PMU	Phasor measurement unit
DS	Distribution grid	PSS	power system stabilisers
DSO	Distribution grid operator	SG	Synchronous generator
ERA	Eigensystem realisation algorithm	TSO	Transmission system operator
ESS	Energy storage system	V2G	Vehicle to grid
EV	Electric vehicle	VSC	Voltage source converter

LIST OF TABLES

Symbols

α_i	Weighting factor per each BESS	$\mathbf{P}_c$	Solution algebraic Riccati equation (ARE)
λ	Lagrange operator	p_{m0}	Initial mechanical power steam turbines
$\mathbf{A}, \mathbf{B}, \mathbf{C}, \mathbf{D}$	Power system model matrices by ERA	p_L	Power demand
AS_k	Binary command for requesting help from adjacent areas	Q_k	Total available capacity of the BESSs per area to inject reactive power
β_i	Amplitude of Chirp signal	S_i^{max}	Maximum apparent power injec. capacity
DB_f, DB_V	Permissible frequency and voltage deadbands	P_i^{ref}, Q_i^{ref}	Estimated optimum active and reactive power for each BESS
$\mathbb{E}$	Expectation operator	SOC_i	SOC computed for each BESS
f_s, f_e	Frequency bands limits of the chirp signal	SOC_{max}	Maximum operating SOC of each BESS
$f_j, \mid V \mid_j$	Remotely measurement of frequency and voltage amplitude in the k-th area	P_k^{ref}, Q_k^{ref}	Optimal active and reactive power estimated for each LQG controller
$\mathbf{G}$	Kalman gain	SOC_{min}	Minimum operating SOC of each BESS
$\mathbf{H}$	Scalar Hamiltonian function	SOC_{opt}	Optimal SOC at each BESS
$\mathbf{H}_0, \mathbf{H}_1$	Hankel matrix and shifted Hankel matrix	T	Lasting signal time of the Chirp signal
H_g	Inertia constant of the system	$\mathbf{u}$	Control actions
$\mathbf{H}_0$	Hankel matrix	v_d, v_q	Direct and quadrature voltage
i_d, i_q	Direct and quadrature current	V_{ref}, f_{ref}	Voltage amplitude and frequency set point
i	i-th BESS index	$\hat{\mathbf{x}}$	Full state estimation of $\mathbf{x}$
j	j-th remote sensor index	$\hat{\mathbf{y}}$	Full estimation of $\mathbf{y}$
J_c	Quadratic cost function of LQR controller	$\mathbf{y}$	Plant outputs, measurement variables
J_E	Quadratic cost function of LQE estimator	$\mathbf{y}^*$	Set-points of controlled variables
k	k-th area controlled index	T_p, T_s, T_z	Time constants of the SG
$\mathbf{Q}_c, \mathbf{R}_c$	Weighting matrices of the LQG controller	$\mathbf{x}$	State variables
$\mathbf{K}_c$	Optimal control gain	T_{max}, T_i	Maximum operating and actual temperature of each BESS
M_{on}	Binary command to execute the ERA identification routine	ω_o	Angular speed estimated by PLL system
n	Total number of BESSs grouped per area	ω_g	Machine angular frequency
$\mathbf{P}, \mathbf{Q}$	Unitary matrices used in ERA		

Chapter 1

Introduction

1.1 Background and Motivation

Dynamics in traditional power systems are primarily dominated by the actions of synchronous generators (SGs) [6, 7]. However, the increasing spread of distributed energy resources (DERs), renewable energy systems and the connection of nonlinear loads with fast time-constants trigger undesired dynamics that droop control and automatic generation control (AGC) systems are unable to handle, impacting the stability and reliability of modern power grids [8, 9, 10, 11, 12, 13]. This fact motivates the suitable combination of both SGs and energy storage systems (ESSs) acting in coordination through novel control schemes that prioritize, in an accurate and a fast way, the power dispatch. The ESSs can significantly improve the performance and security of transmission networks, improving the voltage and frequency transient responses [14, 15]. Likewise, it is also mandatory to bring both responses within the voltage and frequency limits, as shows in Fig. 1.1, according to the establishment in the standard ANSI [1, 16].

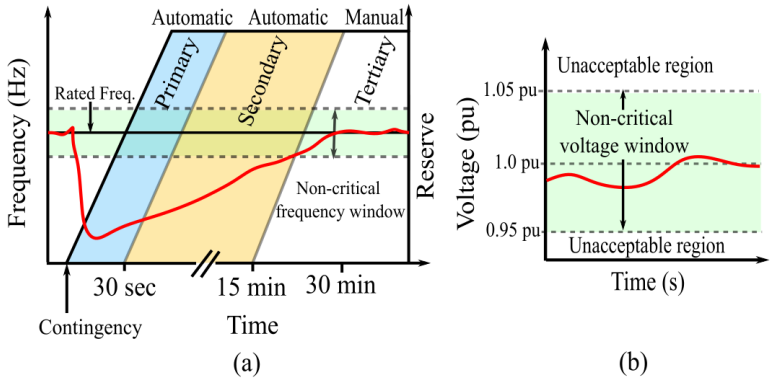

Figure 1.1: Operating windows for voltage and frequency (ANSI C84.1 limits) [1].

1.1. Background and Motivation

The voltage and frequency deviations can be partially mitigated at the operational planning stage [12]. However, in a short-time (within a millisecond scale), the system may be exposed to unsafe operating states caused by unforeseen events, such as unbalanced failures, rapid load changes, generation losses, among others [17]. Such operating conditions lead the system to abnormal voltage and frequency levels that can be tolerated for a short period. Still, it is imperative to quickly bring them within established limits [1, 16].

Recent contributions highlight the application of battery-based systems for frequency and voltage support in power transmission networks [18, 19]. In [6], a real-time controller that formulates the power command sets as an optimization problem is experimentally validated, this considers the converter capacity and battery energy storage systems (BESS) safety constraints to provide ancillary services towards power grids. In [20] and [21], closed-loop control systems are proposed leveraging the BESSs to enhance the inertia of the power system even under conditions of high penetration of photovoltaic plants. In [22], an open source tool for dynamic co-simulation of transmission and distribution networks with high penetration of DERs and their influence on frequency and voltage regulation is presented. A scheme based on linear control loops, static compensators and BESSs to improve the voltage and frequency stability and energy transport capacity in an interconnected multi-generator system is investigated in [15]. In [10], a central primary controller based on coordinated BESSs is proposed to mitigate voltage and frequency deviations of transmission networks.

In [23], the benefits of a novel method of coordinated control to reduce the secondary frequency droop using a BESS are presented, where the controller allows minimizing the BESS utilization. However, despite the positive results presented, this strategy neglects the regulation of the voltage profile in the network. Similarly, in [24] are reported experimental results verifying the effectiveness of the control method based on frequency and voltage deviations. Although this technique exhibits a response time of less than 30s, the frequency and voltage regulations present significant deviations with respect to the steady-state control commands. In [25], a hierarchical control method for frequency and voltage regulation based on the integration of distributed energy resources and indirect measurement of control variables from load flows is proposed. The algorithm is able to mitigate the contingency in 7s, but causing oscillations in the active power injection of some generators and retaining a steady-state error in controlled variables until the frequency and voltage deviation computations are updated.

In [26], several strategies to provide frequency support under low grid inertia conditions using BESSs are proposed. The presented techniques consider the simultaneous injection of active and reactive power up to the BESS operating limits. A quantitative analysis of the impact of BESS for frequency regulation in low inertia networks based on stochastic models of demand and production is presented in [27]. The results only deal with the hourly estimates, preventing the evaluation of the dynamic response of the control schemes in a short time frame (on a scale of seconds). In addition, this work does not report strategies that consider

the operational constraints of the electronic converters and batteries which constitute the BESSs.

Several control schemes for frequency and voltage support by power injection from the BESS are summarized in Table 1.1. Most of these works address the dynamic analysis from off-line simulations performed in Matlab & Simulink™software. All reviewed controllers do not jointly consider the BESS operating constraints, the propagation of contingencies between network areas and the optimal calculation of control set points. From Table 1.1, it can be observed that all the reviewed controllers present a response time larger than 5s.

Although applications of BESSs in power systems have been widely addressed in previous research [15, 22, 20, 21, 29], two research gaps in the existing literature on real-time control of BESSs can be highlighted: (*i*) the formulation of optimal control strategies with very fast response time (in the scale of milliseconds), which coordinates the injection of power from clustered BESSs aiming to provide ancillary services and working cooperatively with

Table 1.1: Comparison of works that exploit the BESSs to mitigate voltage and frequency deviations.

Cite	**Simulator**	**Network**	**Timeline**	**Response time**	**Controller type**	**Validation via**
[9]	Matlab & Simulink™	3-LCA 9-machine/5-LCA 68-bus	Seconds	9 s	Coordinated controller	Off-line simulations
[20]	–	IEEE 9-bus system	Seconds	5.8 s	Droop control, lead-lag	Off-line simulations
[21]	PSCAD/EMTDC	IEEE 14 bus system	Hours	30 m	Droop control	Off-line simulations
[27]	Matlab & Simulink™	IEEE 39-bus	24 hours	hours	droop-based PLL-free controller	RT simulations
[26]		particular 5-bus system, Eyre Peninsula in Australia	Seconds	10 s	Prioritization active/reactive power	Off-line simulations
[25]	Matlab & Simulink™	33-bus, 9 machines	Seconds	7 s	Prioritization active/reactive power	Off-line simulations
[23]	Matlab & Simulink™	Particular system, 2-bus, 3 machines, 1 BESS, 1 PMSG	Seconds	15 s	Coordinated Controller	Off-line simulations
[24]	Matlab & Simulink™	particular system, 3 bus, 1 SG, 1 wind power plant and 1 BESS	Seconds	20 s	APLL-Based controller	RT simulations
[28]	Matlab & Simulink™	particular system, 4-area, 4 machines with WPP and BESS	Hours	1 m	Coordinated controller	Off-line simulations
Proposed	Matlab & Simulink™	Modified Kundur system with 4 areas, 8 machines and 7 BESSs	Seconds	**450ms**	Hierarchical coordinated controller	Off-line simulations

the traditional controllers in the transmission network, and (*ii*) the integration of algorithms that enhance battery utilization and include the operational constraints of BESS, increasing your operational safety.

Charging systems and batteries for electric vehicles (EVs) can also provide ancillary services to the distribution network. The massive introduction of EVs in distribution systems (DSs) can contribute to improve stability and reliability of the modern electrical grids [30]. In turn, EVs chargers working in vehicle-to-grid (V2G) mode can extend the benefits of EVs in electrical power systems, such as voltage support through reactive power injection [31, 32, 33].

In the past, electromechanical devices, such as shunt capacitor banks and on-load tap changers (OLTCs) have been widely used to perform Volt/Var Control (VVC) in distribution networks [34, 35]. Nonetheless, they exhibit discrete changes and slow response to rapid voltage fluctuations. Conversely, electronic power converters, as EV chargers, can act in a short-time scale due to its intrinsic nature, enabling them to protect sensitive loads and devices against significant voltage variations throughout the grid. Despite most of these DERs can control their energy production, the high penetration of these resources can increase the probability of conflict between their control actions and the conventional control devices installed in DSs, making necessary the development of sophisticated control systems that coordinates the injection of reactive power with intelligent measurements devices to ostensibly improve the dynamic performance of the grid voltage profile [36, 37].

Alternatively, distribution grids may introduce an intelligent hierarchical control system, that in coordination with the distribution system operator (DSO), they can harness the resources available on the network to regulate the voltage variations. Thereby, the reactive power injection can be optimally controlled to improve the power quality, the reliability and energy efficiency of the grid operation. The hardware of EVs chargers has the potential to inject reactive power enhancing the voltage profile and providing ancillary services to the DSs without degrading the batteries lifetime, even when EVs are disconnected; this is possible thanks to the DC/AC power electronic converters. However, uncoordinated reactive power injections can exacerbate the stability and grid security problems, increasing voltage spikes and operating cost of DSs [36, 38, 13]. In this context, the proper voltage regulation largely depends on the smart measurement strategies, the fast response of EVs chargers, the knowledge of the dynamic behavior of the power network and the optimization of control actions [37, 39, 13]. An integrated and descriptive scheme composed of a set of EV chargers represented by parking lots and distribution-level phasor measurement units (D-PMUs) connected to the active distribution grid can be noticed in Fig. 1.2.

Although there is a rich literature for EVs active power optimal programming, the coordinated hierarchically reactive power delivery in the short-time scale has not been addressed adequately. In [3], a modeling framework for charging analysis of EVs in residential

distribution systems is presented by proposing controlled loading schedules. Nevertheless, this work only deals with the hourly breakdown of the demand changes, preventing the analysis of the distribution network dynamic response. Besides, it proposes that all decisions and control actions are calculated by DSO, loading it up with an enormous flow of information, when the grid has thousands of connected EV chargers.

Another approach consisting of a three-stage algorithm that coordinates the EV chargers operation, making VVC possible is proposed in [40]. However, the control actions are daily updated in the first stage and every five minutes for the second and third stages, respectively. Within five minutes, voltage variations can exceed the allowable limit for sensitive loads, or even they can destabilize the system. The advantages of the V2G operation mode for reactive power compensation are presented in [31]. Nevertheless, the impact of multiple connected chargers on the grid is not taken into account. This work neither analyzes the control actions on the grid side to provide reactive power support. In [36], the benefits of a hierarchical coordination framework that manages the dispatch of active and reactive power from EVs at the distribution level are demonstrated. Nonetheless, the efficacy analysis of chargers to quickly compensate the voltage variations in the network is not reported.

Most of the previous works are limited to analyze the grid operation programming in a 24-hour time horizon, obviating the short-time dynamic response [3, 40, 36]. Thus, this work proposes a hybrid Volt/Var regulation framework for highly unbalanced distribution grids, by exploiting the advantages of central and local controllers embedded into a hierarchical

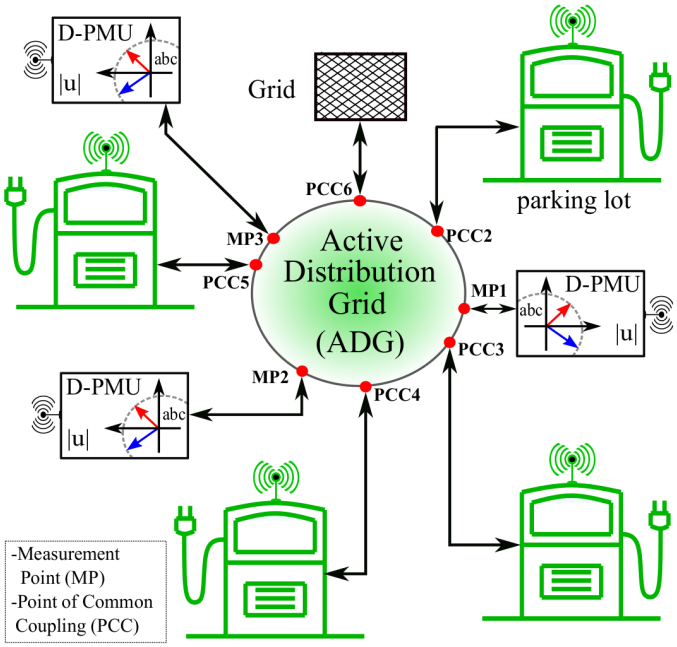

Figure 1.2: Distribution grid concept with ancillary services supplied by EV battery chargers and remote measurements.

and coordinated closed-loop optimal control scheme. This approach is founded on the eigensystem realization (ER)-based identification technique and a linear quadratic Gaussian (LQG) control structure [41, 42]. The proposed framework incorporates the advance in time-synchronized measurement devices to compensate for the voltage in DSs remotely [43].

1.2 Research Objectives

The general objective of this research is to develop an optimal control strategy exploiting smart monitoring and battery-based systems for the provision of ancillary services to the grid.

The specific objectives of this dissertation are stated as follows:

- To establish the functional specifications of the controller, metering systems and battery-based converters for the provision of ancillary services to the grid.
- To propose a novel grid voltage and frequency support strategy to increase power system stability and reliability.
- To perform experimental tests validating the advantages of the proposed theoretical assumptions in comparison with those reported in the technical literature.

1.3 Outline of the Contents

This dissertation has been submitted for assessment in partial fulfillment of the doctoral degree. An abbreviated compendium of the results obtained in the doctoral project is presented in this dissertation. These results have also been published in journal papers, book chapters and conference papers. These results are used directly or indirectly in this dissertation.

This thesis is organized as follows:

- **Chapter 2** reports the mathematical foundations of eigensystem realization algorithm and linear quadratic Gaussian controller.
- **Chapter 3** presents the development of a novel hierarchical controller to support the frequency and voltage in a multi-area transmission systems, integrating battery energy storage systems. The design is based on the prioritization of coordinated power injection from the battery-based systems over conventional synchronous generators. Two hierarchical schemes are included, one physical and one logical, which include operating rules to reduce disturbances in neighboring areas caused by local control actions, and also increase the operational safety and lifetime of the batteries.

  This chapter is based on two papers published in refereed journals.
- **Chapter 4** reports the application of the proposed hybrid controller to enhance the voltage profile and to increase the operational flexibility of highly unbalanced active distribution networks by optimally coordinating the reactive power injection of multiple off-board electric vehicle chargers. The logical and scalable hierarchical scheme in coordination with the distribution system operator is presented. This chapter develops the rules of a new aggregating agent that coordinates the power injection of electric vehicle chargers to accurately and timely regulate the dynamic voltage response in each subarea of the whole distribution network.

  This chapter is based on an journal published in a refereed journal, a book chapter and a peer-reviewed conference.
- **Chapter 5** reports the contributions and future research works.

Chapter 2

Theoretical Foundations

In this chapter, the theoretical foundations for synchronous generators, the differential-algebraic equations (DAE) of non-linear power system, battery energy storage systems, EV chargers, the black-box identification method known as eigensystem realization algorithm (ERA) and the linear quadratic Gaussian (LQG) optimal control scheme are presented.

2.1 Synchronous Machine Model

modelo de 4 orden con exitador tipo I, las ecuaciones 1 a 4 son las del generador, y las 3 ultimas son las del exitador. The two-axis model represented in the differential-algebraic equations for the power system of m machines is given by [44]

$$T'_{doi}\frac{dE'_{qi}}{dt} = -E'_{q_i} - \left(X_{di} - X'_{di}\right) I_{di} + E_{fdi} \quad i = 1, \ldots, m \tag{2.1.1}$$

$$T'_{qoi}\frac{dE'_{di}}{dt} = -E'_{di} + \left(X_{qi} - X'_{qi}\right) I_{qi} \quad i = 1, \ldots, m \tag{2.1.2}$$

$$\frac{d\delta_i}{dt} = \omega_i - \omega_s \quad i = 1, \ldots, m \tag{2.1.3}$$

$$\frac{2H_i}{\omega_s}\frac{d\omega_i}{dt} = T_{Mi} - E'_{di}I_{di} - E'_{qi}I_{qi} - \left(X'_{qi} - X'_{di}\right) I_{di}I_{qi} - D_i\left(\omega_i - \omega_s\right) \quad i = 1, \ldots, m \tag{2.1.4}$$

$$T_{Ei}\frac{dE_{fdi}}{dt} = -\left(K_{Ei} + S_{Ei}\left(E_{fdi}\right)\right)E_{fdi} + V_{Ri} i = 1, \ldots, m \tag{2.1.5}$$

$$T_{Fi}\frac{dR_{fi}}{dt} = -R_{fi} + \frac{K_{Fi}}{T_{Fi}}E_{fdi} \quad i = 1, \ldots, m \tag{2.1.6}$$

$$T_{Ai}\frac{dV_{Ri}}{dt} = -V_{Ri} + K_{Ai}R_{fi} - \frac{K_{Ai}K_{Fi}}{T_{Fi}}E_{fdi} + K_{Ai}\left(V_{\text{ref}i} - V_i\right) i = 1, \ldots, m \tag{2.1.7}$$

where T'_{doi} and T'_{qoi} are D-axis and Q-axis transient time constants, T_{Ei} and T_{Mi} are the electromagnetic and mechanical torque, respectively. T_{Fi} is a friction windage torque. E'_{qi} and E'_{di} are D-axis and Q-axis transient stator voltages, respectively. E_{fdi} is the field voltage.X_{di} and X_{qi} are D-axis and Q-axis leakage reactances. X'_{di} and X'_{qi} are transient D-axis and Q-axis leakage reactances. I_{di} and I_{qi} are D-axis and Q-axis stator currents. ω_s and δ_i are synchronous speed and the machine angle, respectively. V_{Ri} is the voltage scaled to system power base and V_i is the voltage regulator input voltage. R_{fi} is the stabilizer feedback variable, K_{Fi} is the exciter feedback constant, K_{Ai} is the amplifier gain in the voltage regulator and K_{Ei} is the self-excited constant. Detailed parameters of each SG are listed in Table 3.1.

2.2 Multi-machine power system model

The nature of power systems is highly nonlinear and is conventionally modeled by a set of differential-algebraic equations of the form [44]:

$$\begin{aligned} \dot{\mathbf{x}} &= f(\mathbf{x}, \mathbf{y}, \mathbf{u}) \\ 0 &= g(\mathbf{x}, \mathbf{y}) \end{aligned} \tag{2.2.1}$$

where $\mathbf{x}$ and $\mathbf{u}$ respectively stand for the state and input vectors, meanwhile $\mathbf{y}$ represents a set of algebraic variables related to voltage and currents. From (2.2.1), traditional power system linear models equipped with synchronous generators can be derived around multiple equilibrium points and they can be then evaluated regarding feasible operating points for $\mathbf{x^0}$, $\mathbf{y^0}$ and $\mathbf{u^0}$. Then, the application of linearization techniques results in the descriptor of the system, as follows [45].

$$\begin{aligned} \Delta\dot{\mathbf{x}}_s &= \mathbf{A}_s\Delta\mathbf{x}_s + \mathbf{B}_s\Delta\mathbf{U}_s \\ \Delta\mathbf{y}_s &= \mathbf{C}_s\Delta\mathbf{x}_s + \mathbf{D}_s\Delta\mathbf{U}_s \end{aligned} \tag{2.2.2}$$

where the subscript "s" denotes the model associated with traditional synchronous generators, $\mathbf{A}_s$ is the state matrix, $\mathbf{B}_s$ is the input matrix, $\mathbf{C}_s$ is the output matrix and $\mathbf{D}_s$ is the direct transition matrix.

With the advent of more renewable energy sources, actuators and non-conventional equipment (inverter-based generators, FACTS, BESS, HVDC); other dynamics have been incorporated to the system, increasing its complexity and challenging its modelling. Nevertheless, its state-space representation considering all these new features still prevails as depicts in the following:

$$\begin{aligned} \Delta\dot{\mathbf{x}}_T &= \mathbf{A}_T\Delta\mathbf{x}_T + \mathbf{B}_T\Delta\mathbf{U}_T \\ \Delta\mathbf{y}_T &= \mathbf{C}_T\Delta\mathbf{x}_T + \mathbf{D}_T\Delta\mathbf{U}_T \end{aligned} \tag{2.2.3}$$

Now, the subscript "T" denotes the model associated with synchronous generators spanned with other emergent technologies. Where the state and input vectors now include the presence of other actuators which are symbolized with the subscript "o", such that $\Delta\dot{\mathbf{x}}_T = [\Delta\dot{\mathbf{x}}_s, \Delta\dot{\mathbf{x}}_o]^T$, $\Delta\mathbf{x}_T = [\Delta\mathbf{x}_s, \Delta\mathbf{x}_o]^T$, $\Delta\mathbf{u}_T = [\Delta\mathbf{u}_s, \Delta\mathbf{u}_o]^T$, $\Delta\mathbf{y}_T = [\Delta\mathbf{y}_s, \Delta\mathbf{y}_o]^T$. Meanwhile, matrices $\mathbf{A}_T$, $\mathbf{B}_T$, $\mathbf{C}_T$ and $\mathbf{D}_T$ can be shaped as:

$$\begin{aligned} \mathbf{A}_T &= \begin{bmatrix} A_s & 0 \\ 0 & A_o \end{bmatrix} \quad \mathbf{B}_T = \begin{bmatrix} B_s & 0 \\ 0 & B_o \end{bmatrix} \\ \mathbf{C}_T &= \begin{bmatrix} C_s & 0 \\ 0 & C_o \end{bmatrix} \quad \mathbf{D}_T = \begin{bmatrix} D_s & 0 \\ 0 & D_o \end{bmatrix} \end{aligned} \tag{2.2.4}$$

where submatrices $\mathbf{A}_o$, $\mathbf{B}_o$, $\mathbf{C}_o$ and $\mathbf{D}_o$ correspond to the linear representation for other equipments connected besides the synchronous generators.

2.3 BESS topology model and circuit level control

Power electronic converters are the primary technology for the integration of BESS into power grids [46, 47]. Their principal role is interfacing the batteries with the grid, controlling the active and reactive power flow. At the same time, they must ensure a safe battery operation and compliance with grid codes. The literature reports many topologies, among them, the simplicity and high efficiency of the 2-level VSC presented in Fig. 2.1(a), stands out [46]. This topology operates in the four quadrants of the $P-Q$ plane, allowing bidirectional power flow. Its key components are the battery pack, the DC/AC converter, the filters at DC and AC terminals, the protection circuits and the step-up transformer. The transformer is used to boost the voltage from hundreds of volts in the output of the DC/AC converter up to thousands of volts at the point of common coupling (PCC) of the power network. The DC

low-pass filter reduces voltage and current ripples, improving battery operation. The AC filter, consisting of 3 inductors (L_gx3), minimizes the high frequency harmonics caused by the commutation of the power switches [48, 49].

The control system detailed in Fig. 2.1(b) is implemented using PI controllers tuned with the pole-localization method. The small-signal average model of the VSC is defined in (2.3.1) [18, 14]. The regulation of the direct current (i_d) and quadrature current (i_q) facilitates the power flow control in the BESS through the instantaneous power calculation. The synchronization of the VSC with the grid is achieved thanks to the PLL [49].

$$\begin{cases} \frac{di_d}{dt} & = L_g w_o i_q + v_d \\ \frac{di_q}{dt} & = -L_g w_o i_d + v_q \end{cases} \tag{2.3.1}$$

$$\begin{cases} P_k^{ref} & = \frac{3}{2}\left(v_d i_d + v_q i_q\right) \\ Q_k^{ref} & = \frac{3}{2}\left(v_q i_d - v_d i_q\right) \end{cases} \tag{2.3.2}$$

where v_d and v_q symbolize the direct and quadrature voltage in the synchronous reference frame, respectively. ω_o is the angular speed sensed by the PLL system [49].

At battery level, the Shepherd's model is adopted [50]. In this, the open circuit voltage (V_{OC}) for the charge and discharge of li-ion battery pack is determined by

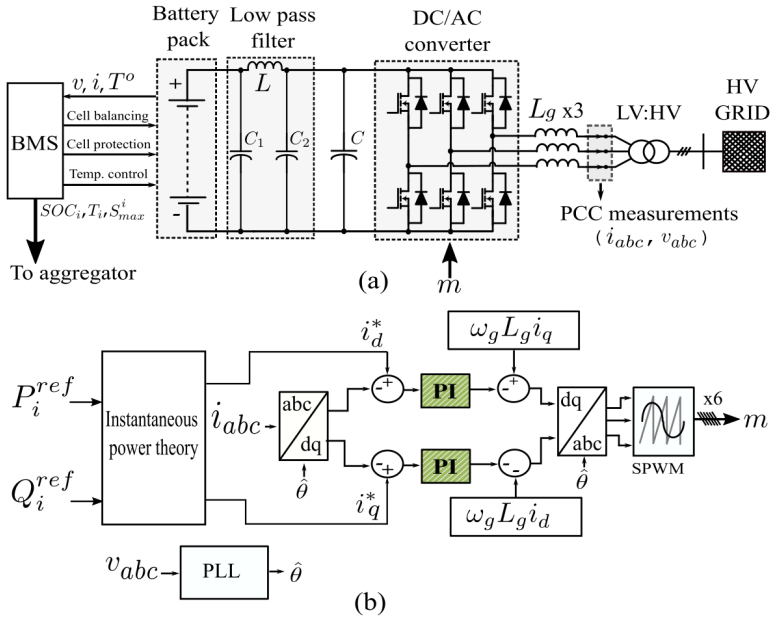

Figure 2.1: BESSs' diagram and its control architecture. (a) Topology. (b) PI controllers in *dq0* reference frame.

$$\begin{cases} V_{OC,\text{charge}} = V_0 - K\frac{Q}{i_t - 0.1Q}i^* - K\frac{Q}{Q-i_t}it + Ae^{-Bi_t}; i^* < 0 \\ V_{OC,\text{dis}} = V_0 - K\frac{Q}{Q-i_t}\left(i_t + i^*\right) + Ae^{-Bi_t}; i^* > 0 \end{cases} \tag{2.3.3}$$

where V_0 is the constant battery voltage, Q is capacity of the battery, i is the dynamic battery current at the time t, and i_t is the discharge capacity, A represents the voltage amplitude in the exponential zone of the discharge curve of the battery, B specifies the exponential capacity, K is polarization constant and i^* is low frequency current dynamics. The cut frecuency f_c of the low pass filter of fig. 2.1(a) is represented by $f_c = \frac{1}{2\pi\sqrt{LC}}$, where $C_1 = C_2 = C$.

2.4 EV-charger model and circuit-level controller

The hardware of each EV battery chargers, summarized in Fig 2.2, is composed of two primary electronic converters: (*i*) a three-phase VSC; and (*ii*) an isolated Dual Active Bridge (DAB) converter. These topologies have been extensively studied by the scientific community, operating in the four quadrants of the $P-Q$ plane and enabling the bidirectional power flow [51, 52, 19]. In this topology, the VSC facilitates the active and reactive power exchange between the DC link capacitor (C) and the utility grid. The DAB regulates active power flow between the DC link and the battery pack inside the EVs. The ripple on the current injected into the network at the PCC is reduced by the inductance filter (L) [19, 8].

The VSC and DAB control system is achieved using PI controllers, Fig. 2.2. This system comprises the following charger operation modes: V2G and Grid-to-Vehicle (G2V). The battery charges employing both Constant Current and Constant Voltage (CC-CV) modes. The VSC is commanded in the $d-q$ reference frame, controlling the direct current (i_d) and the quadrature current (i_q). This controller synchronizes the charger with the grid through the PLL. Meanwhile, the DAB power flow is regulated by two controllers: the first one manages the charge or discharge current (i_{bat}) and the second one controls the battery voltage (v_{bat}). The DAB and VSC average small-signal models are derived from [51, 52, 19]. These models are respectively defined in (2.4.1) and (2.4.2), being used to tune the PI controllers' parameters inside the charger via the pole location method.

$$\frac{d}{dt}\begin{bmatrix}\Delta v_o^0 \\ \Delta i_t^{1R} \\ \Delta i_t^{1I}\end{bmatrix} = \begin{bmatrix}\frac{-1}{RC} & \frac{-4sin(D\pi)}{\pi C} & \frac{-4cos(D\pi)}{\pi C} \\ \frac{2sin(D\pi)}{\pi L_t} & \frac{-R_t}{L_t} & w_s \\ \frac{2cos(D\pi)}{\pi L_t} & -w_s & \frac{-R_t}{L_t}\end{bmatrix}\begin{bmatrix}\Delta v_o^0 \\ \Delta i_t^{1R} \\ \Delta i_t^{1I}\end{bmatrix} + \begin{bmatrix}\frac{4}{C}\left(I_0^I sin(\pi D) - I_0^R cos(\pi D)\right) \\ \frac{2V_o^0}{L_t}cos(\pi D) \\ \frac{-2V_o^0}{L_t}sin(\pi D)\end{bmatrix}\Delta d \tag{2.4.1}$$

$$\frac{di_d}{dt} = Lw_0 i_q - Ri_d - \hat{v}_{sd} + v_{td} \quad , \frac{di_q}{dt} = -Lw_0 i_d - Ri_d - \hat{v}_{sq} + v_{tq} \tag{2.4.2}$$

The Shepherd's model for the li-ion batteries represented in (3.4) is adopted in this work [50].

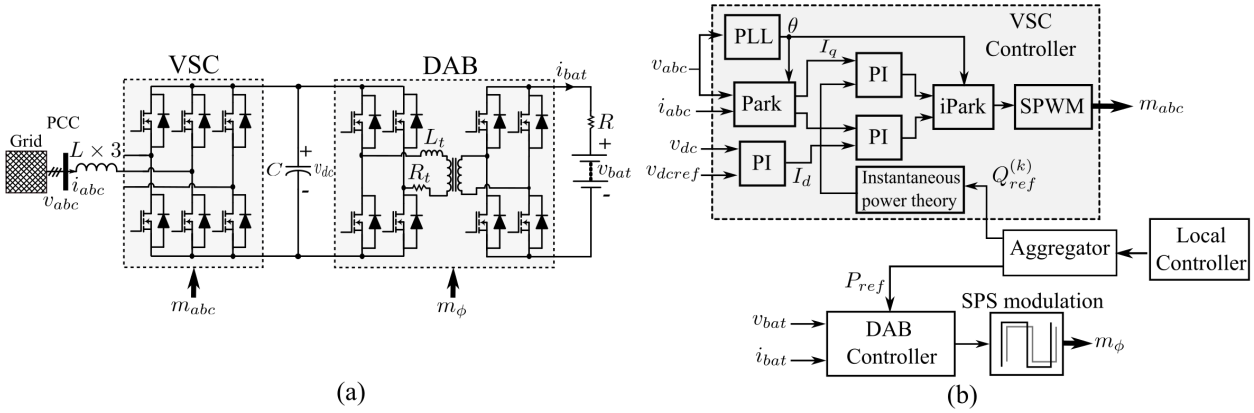

Figure 2.2: Diagram of the EVs battery chargers and its control architecture. (a) VSC-DAB-based EV Battery charger. (b) PI controllers for VSC and DAB converters.

2.5 System Identification by the ERA

A system identification problem is stated to formulate the eigensystem realization, taking into consideration input and output sequences. The input sequence is assumed as known $u(0), u(1), \cdots, u(N)$. The corresponding output sequence stems from time-domain simulations or even actual raw data from the system response. Thus, assuming a measured series composed of discrete-time input/output pairs, it is possible to generate the output sequence as:

$$\begin{aligned} y(0) =& \mathbf{D}u(0) \\ y(1) =& \mathbf{CB}u(0) + \mathbf{D}u(1) \\ y(2) =& \mathbf{CAB}u(0) + \mathbf{CB}u(1) + \mathbf{D}u(2) \\ &\vdots \\ y(N-1) =& \mathbf{CA}^{N-1}\mathbf{B}u(0) + \cdots + \mathbf{CB}u(N-2) + \mathbf{D}u(N-1) \end{aligned} \tag{2.5.1}$$

where matrices $\mathbf{A}$, $\mathbf{B}$, $\mathbf{C}$, and $\mathbf{D}$ are the Markov parameters for the realization, and they are assumed as unknown [53]. Such an output sequence is generalized by

$$\mathbf{y}(k) = \mathbf{CA}^{k-1}\mathbf{B} \tag{2.5.2}$$

The Markov parameters also establish the linear time-invariant state-space model in discrete-time, as follows

$$\begin{aligned} \mathbf{x}(k+1) &= \mathbf{Ax}(k) + \mathbf{Bu}(k) \\ \mathbf{y}(k) &= \mathbf{Cx}(k) + \mathbf{Du}(k) \end{aligned} \tag{2.5.3}$$

Then, the state vector in discrete-time is also inferred by multiplying by $\mathbf{C}^{-1}$ the output sequence $\mathbf{y}(k)$ in (2.5.3) and assuming $\mathbf{D} = 0$, which results in

$$\mathbf{x}(k) = \mathbf{A}^{k-1}\mathbf{B} \tag{2.5.4}$$

Now, if the output sequence is defined by a Hankel representation, then we respectively have for k and $k+1$

$$\mathbf{H}(k) = \begin{bmatrix} y(k) & y(k+1) & \cdots & y(k+N) \\ y(k+1) & y(k+2) & \cdots & y(k+N+1) \\ \vdots & \vdots & \ddots & \vdots \\ y(k+N) & y(k+N+1) & \cdots & y(k+2N) \end{bmatrix} \tag{2.5.5}$$

and

$$\mathbf{H}(k+1) = \begin{bmatrix} y(k+1) & y(k+2) & \cdots & y(k+N+1) \\ y(k+2) & y(k+3) & \cdots & y(k+N+2) \\ \vdots & \vdots & \ddots & \vdots \\ y(k+N+1) & y(k+N+2) & \cdots & y(k+2N+1) \end{bmatrix} \tag{2.5.6}$$

Which in terms of the generalized output sequence is given by

$$\mathbf{H}(k) = \begin{bmatrix} \mathbf{CA}^{k-1}\mathbf{B} & \mathbf{CA}^{k}\mathbf{B} & \cdots & \mathbf{CA}^{k-1+n}\mathbf{B} \\ \mathbf{CA}^{k}\mathbf{B} & \mathbf{CA}^{k+1}\mathbf{B} & \cdots & \mathbf{CA}^{k+n}\mathbf{B} \\ \vdots & \vdots & \ddots & \vdots \\ \mathbf{CA}^{k-1+n}\mathbf{B} & \mathbf{CA}^{k+n}\mathbf{B} & \cdots & \mathbf{CA}^{k-1+2n}\mathbf{B} \end{bmatrix} \tag{2.5.7}$$

Then, the generalized Hankel representation (2.5.7) in matrix form becomes

$$\mathbf{H}(k) = \underbrace{\begin{bmatrix} \mathbf{C} \\ \mathbf{CA} \\ \vdots \\ \mathbf{CA}^{n} \end{bmatrix}}_{\boldsymbol{\xi}} \mathbf{A}^{k-1}[\mathbf{B} \quad \mathbf{AB} \quad \cdots \mathbf{A}^{n}\mathbf{B}] \tag{2.5.8}$$

where $\boldsymbol{\xi}$ in (2.5.8) stands for the reachability and the term $\mathbf{A}^{k-1}\mathbf{B}$ represents the controllability.

If only $k = 1$ and $k = 2$ are taken into account in (2.5.8), then we have

$$\begin{aligned} \mathbf{H}(1) &= \boldsymbol{\xi}\mathbf{B} \\ \mathbf{H}(2) &= \boldsymbol{\xi}\mathbf{AB} \end{aligned} \tag{2.5.9}$$

Finally, it is possible to estimate the Markov parameters from (2.5.9) by means of the singular value decomposition applied to $\mathbf{H}(1) \in \Re^{N\times N}$ and its truncation up to the r-th singular values (with $r < N$), ensuring a full rank for the system. This can be notated as

$\mathbf{H}(1) = \mathbf{P}\mathbf{S}^{1/2}\mathbf{S}^{1/2}\mathbf{Q}^T$, which derives that $\boldsymbol{\xi} = \mathbf{P}\mathbf{S}^{1/2}$ and $\mathbf{B} = \mathbf{S}^{1/2}\mathbf{Q}^T$ in (2.5.9), leading to estimate the discrete system matrices as

$$\begin{aligned}\mathbf{A} &= \mathbf{S}^{-1/2}\mathbf{P}^T\mathbf{H}(2)\mathbf{Q}\mathbf{S}^{-1/2}\\ \mathbf{B} &= \mathbf{S}^{1/2}\mathbf{Q}^T\\ \mathbf{C} &= \mathbf{P}\mathbf{S}^{1/2}\\ \mathbf{D} &= y(0)\end{aligned} \tag{2.5.10}$$

Once the identified linear model for one output channel is available, this is extended to multiple output sequences in the following.

2.5.1 Identification for multiple outputs

For multiple outputs channels, the matrix $\mathbf{Y}_m \in \Re^{N\times j}$ is shaped by j column arrays corresponding to single channels, as follows

$$\mathbf{Y}_j = [\mathbf{y}^{\{1\}}\ \mathbf{y}^{\{2\}}\ \cdots\ \mathbf{y}^{\{q\}}\ \cdots\ \mathbf{y}^{\{j\}}] \tag{2.5.11}$$

where the $q-th$ column is represented by $\mathbf{y}^{\{q\}} = [y(0)\ y(1)\ \cdots\ y(N-1)]^T$. Thus, the multivariate representation is defined by

$$\begin{bmatrix}\mathbf{Y_0}\\ \mathbf{Y_1}\\ \vdots\\ \mathbf{Y_k}\end{bmatrix} = \begin{bmatrix}[y_0^{\{1\}} & y_0^{\{2\}} & \cdots & y_0^{\{j\}}]^T\\ [y_1^{\{1\}} & y_1^{\{2\}} & \cdots & y_1^{\{j\}}]^T\\ \vdots & \vdots & \vdots & \vdots\\ [y_{N-1}^{\{1\}} & y_{N-1}^{\{2\}} & \cdots & y_{N-1}^{\{j\}}]^T\end{bmatrix} \tag{2.5.12}$$

Similarly to (2.5.1), the input/output measurement pairs allow expressing the output sequence for multiple channels as

$$\begin{aligned}\mathbf{Y}_0 &= \tilde{\mathbf{D}}\\ \mathbf{Y}_1 &= \tilde{\mathbf{C}}\tilde{\mathbf{B}}\\ \mathbf{Y}_2 &= \tilde{\mathbf{C}}\tilde{\mathbf{A}}\tilde{\mathbf{B}}\\ &\vdots\\ \mathbf{Y}_{N-1} &= \tilde{\mathbf{C}}\tilde{\mathbf{A}}^{N-1}\tilde{\mathbf{B}}\end{aligned} \tag{2.5.13}$$

It is noteworthy that (2.5.13) follows the same sequence as in (2.5.2) for the Markov parameters of multiple channels termed as $\tilde{\mathbf{A}}$, $\tilde{\mathbf{B}}$, $\tilde{\mathbf{C}}$, and $\tilde{\mathbf{D}}$. Thereby, the Hankel matrix can be also stated for multiple output channels as $\tilde{\mathbf{H}}(k) = \tilde{\boldsymbol{\xi}}\tilde{\mathbf{A}}^{k-1}\tilde{\mathbf{B}}$. Afterwards, the block Hankel matrix in (2.5.5) becomes as

$$\tilde{\mathbf{H}}(k) = \begin{bmatrix}\mathbf{Y}_k & \mathbf{Y}_{k+1} & \cdots & \mathbf{Y}_{k+N}\\ \mathbf{Y}_{k+1} & \mathbf{Y}_{k+2} & \cdots & \mathbf{Y}_{k+N+1}\\ \vdots & \vdots & \ddots & \vdots\\ \mathbf{Y}_{k+N} & \mathbf{Y}_{k+N+1} & \cdots & \mathbf{Y}_{k+2N}\end{bmatrix} \tag{2.5.14}$$

By assuming $k = 1$ and $k = 2$ into (2.5.14), the Hankel matrices $\tilde{\mathbf{H}}(1)$ and $\tilde{\mathbf{H}}(2)$ can be derived as in (2.5.9).

Now, $\tilde{\mathbf{B}}$ can be obtained from $\tilde{\mathbf{H}}(1) \in \Re^{j(N/2-1)\times(N/2-1)}$, and $\tilde{\mathbf{A}}$ is derived from $\tilde{\mathbf{H}}(2) \in \Re^{j(N/2-1)\times(N/2-1)}$. Therefore, the Markov parameters for multiple output channels have the following form:

$$\begin{aligned}\tilde{\mathbf{A}} &= \tilde{\mathbf{S}}^{-1/2}\tilde{\mathbf{P}}^T\tilde{\mathbf{H}}(2)\tilde{\mathbf{Q}}\tilde{\mathbf{S}}^{-1/2}\\ \tilde{\mathbf{B}} &= \tilde{\mathbf{S}}^{1/2}\tilde{\mathbf{Q}}^T\\ \tilde{\mathbf{C}} &= \tilde{\mathbf{P}}\tilde{\mathbf{S}}^{1/2}\\ \tilde{\mathbf{D}} &= \mathbf{Y}_0\end{aligned} \tag{2.5.15}$$

Until now, the distribution grid linear model represented for matrices $\tilde{\mathbf{A}}$, $\tilde{\mathbf{B}}$, $\tilde{\mathbf{C}}$, and $\tilde{\mathbf{D}}$ can be identified for multiple voltage channels coming from different locations thanks to the availability of time-synchronize voltage measurements provided by D-PMUs.

2.5.2 Probing signals via Chirp input modulations

In this section, the input sequence is rendered by assuming probing signals represented by an exponential Chirp function that modulates the reference power at every energy storage system. Thereby, the chirp function allows making a frequency sweep [54]. The probing signal stimulates the battery-based system dynamics and it is defined by

$$u_i(t) = \alpha_i \sin\left(\frac{2\pi f_s(r_f^t - 1)}{\ln(r_f)}\right) \tag{2.5.16}$$

$$r_f = \left(\frac{f_e}{f_s}\right)^{1/T} \tag{2.5.17}$$

where α_i is the amplitude, T is the lasting signal time, f_s and f_e are respectively the starting and ending frequencies of the chirp signal.

2.5.3 Output sequence data preparation

A time output sequence represented by the synchrophasor voltage magnitudes is required by the ER formulation, being generated via time-domain simulations in response to the chirp modulations. That is, the system response is captured after the steady-state is reached. Afterwards, Fourier spectra are applied to the output sequence signals, $\text{fft}(y_j)$, resulting in the frequency response $Y_j(s)$, for the *j-th* output signal. Finally, a time output sequence per signal correlated with the *i -th* input is obtained taking the inverse Fourier transform of the impulse response as [54]

$$y_j(t) = \mathscr{F}^{-1}\left(\frac{Y_j(s)}{U_i(s)}\right) \tag{2.5.18}$$

where $U_i(s)$ =fft(u_i).

Once the distribution system linear model is drawn, it is is embedded into the optimal control strategy presented in Section 4.3.

2.6 Optimal Controller Design

In this work, a LQG controller is proposed due to its simplicity, ubiquitous application, well-defined quadratic cost functions and the existence of known optimal solutions. Thus, the fundamentals of optimal control theory that shape the linear quadratic regulator (LQR) design are discussed. Afterwards, the state estimation using linear quadratic estimator (LQE) is formally introduced. Thus, both LQR and LQE are discussed in brief.

2.6.1 Linear quadratic regulator

Bellman's principle provides a solution to minimize the error and effort, by optimizing the state-feedback control action that modifies the dynamics of the system. Thus, to balance aggressive regulation of $\mathbf{x}$ with the cost of control action $\mathbf{u}$, a quadratic cost function J is proposed [55]

$$J(t) = \frac{1}{2}\int_0^{\tau} \left(\mathbf{x}^T\mathbf{Q}\mathbf{x} + \mathbf{u}^T\mathbf{R}\mathbf{u}\right) dt \tag{2.6.1}$$

where, $\mathbf{Q}$ and $\mathbf{R}$ are real, symmetric, diagonal and constant matrices. The values assigned to $\mathbf{Q}$ and $\mathbf{R}$ set the dynamic behavior of the controller. $\mathbf{Q}$ is a positive semi-definite, i.e. $\mathbf{Q} \geq 0$ and $\mathbf{R}$ is a positive definite, i.e. $\mathbf{R} > 0$. Matrices $\mathbf{Q}$ and $\mathbf{R}$ weight the cost of state deviations from zero and the cost of actuation, respectively. In these matrices, the tuning of the diagonal elements allows to change the importance assigned between the error and effort of actuation, prioritizing precision or energy saving. For example, if we increase the inputs of $\mathbf{Q}$ by a factor of 10 and keep $\mathbf{R}$ the same, then the precise regulation of the states is weighted more heavily, and the control will be more aggressive [56]. The goal is to develop a control strategy that minimizes $\lim_{\tau\to+\infty} J(t)$ [55].

Accordingly, this approach in (2.6.1) estimates the optimal command $\mathbf{u}$, controlling the plant outputs ($\mathbf{y}$) to approximate it to the desired values ($\mathbf{y}^*$) [55].

The cost function is related to the linear dynamical system represented by (2.5.15). If the system in (2.5.15) is controllable, then a proportional controller can be designed that follows the optimal state feedback control vector defined in (2.6.2).

$$\mathbf{u} = -\mathbf{K}\mathbf{x} \tag{2.6.2}$$

The optimization problem is solved through the scalar Hamiltonian function ($\mathbf{H}$). It is determined by the cost function (2.6.1) and the constraints imposed by the system model in (2.5.15) [8, 57, 55].

$$\mathbf{H} = \mathbf{x}^T\mathbf{Q}\mathbf{x} + \mathbf{u}^T\mathbf{R}\mathbf{u} + \lambda(\mathbf{A}\mathbf{x} + \mathbf{B}\mathbf{u}) \tag{2.6.3}$$

Where λ is Lagrange operator. If $-d\mathbf{H}/d\mathbf{x} = -\mathbf{Q}\mathbf{x} - \mathbf{A}^T\lambda = 0$ in (2.6.3), $\mathbf{u}$ is redefined as $\mathbf{u} = -\mathbf{R}^{-1}\mathbf{B}^T\lambda$. Where, $\lambda = \mathbf{P}\mathbf{x}$. Thus, the optimal control gain $\mathbf{K}$ that minimizes (2.6.1) is defined as follows

$$\mathbf{K} = \mathbf{R}^{-1}\mathbf{B}^T\mathbf{P} \tag{2.6.4}$$

$\mathbf{P}$ is a unique symmetric and positive semidefinite solution of the algebraic Riccati equation (ARE). It is derived from (2.6.3) and (2.6.2). ARE is given by

$$\mathbf{A}^T\mathbf{P} + \mathbf{P}\mathbf{A} - \mathbf{P}\mathbf{B}\mathbf{R}^{-1}\mathbf{B}^T\mathbf{P} + \mathbf{Q} = 0 \tag{2.6.5}$$

By substituting the resulting $\mathbf{u}$ in (2.5.15), the closed-loop system is stable and is represented by

$$\dot{\mathbf{x}} = (\mathbf{A} - \mathbf{B}\mathbf{K})\mathbf{x} \tag{2.6.6}$$

2.6.2 Linear quadratic estimator

The above optimal LQR controller requires information on the complete state of the system. Nevertheless, for many applications, full-state measurements are technologically unfeasible or prohibitively expensive to both acquire and process. In practice, it is frequently required to estimate the full state $\mathbf{x}$ from the restricted noisy measurements of $\mathbf{y}$. This estimation approach balances information from a state prediction model with available measurements. Thus, it is possible to develop a stable estimator that converges to an estimate of the full state, which can be used in conjunction with the optimal feedback LQR control law outlined above [56, 55].

Considering the proposed LQR presented in Section 2.6.1, a LQE based on the Kalman filter theory is used to complete the estimation in this work.

Let's now consider a full state estimator that yields an estimate $\hat{\mathbf{x}}$ for the full state $\mathbf{x}$ using only knowledge of the measurements $\mathbf{y}$, the actuation input $\mathbf{u}$, and a model of the process dynamics in (2.5.15). If the system is observable, it is feasible to compute an estimator with a filter gain ($\mathbf{G}$) [56, 55], as follows

$$\begin{cases} \dot{\hat{\mathbf{x}}} &= \mathbf{A}\hat{\mathbf{x}} + \mathbf{B}\mathbf{u} + \mathbf{G}(\mathbf{y} - \hat{\mathbf{y}}) \\ \hat{\mathbf{y}} &= \mathbf{C}\hat{\mathbf{x}} + \mathbf{D}\mathbf{u} \end{cases} \tag{2.6.7}$$

where $\hat{\mathbf{y}}$ is the prediction of the expected output from the full state estimation $\hat{\mathbf{x}}$.

For the observable system in (2.5.15), it is feasible to arbitrarily place the eigenvalues of the dynamics of the estimator $\mathbf{A} - \mathbf{G}\mathbf{C}$, guaranteeing the stable convergence of the estimate $\hat{\mathbf{x}}$ to the actual state $\mathbf{x}$. Thus, the estimation error $\mathbf{e} = \mathbf{x} - \hat{\mathbf{x}}$ is introduced. The dynamic error $\dot{\mathbf{e}}$ is described by

$$\dot{\mathbf{e}} = (\dot{\mathbf{x}} - \dot{\hat{\mathbf{x}}})(\mathbf{A} - \mathbf{G}\mathbf{C}) \tag{2.6.8}$$

The Kalman filter is a full-state optimal estimator that minimizes the following cost function

$$J_K(t) = \lim_{t \to +\infty} \mathbb{E}\left((\mathbf{x} - \hat{\mathbf{x}})^T (\mathbf{x} - \hat{\mathbf{x}})\right) \tag{2.6.9}$$

where $\mathbb{E}$ is the expectation operator. The optimal Kalman filter gain G is given by

$$\mathbf{G} = \mathbf{V_n} \mathbf{C}^T {\mathbf{P_o}}^{-1} \tag{2.6.10}$$

where $\mathbf{P_o}$ is the solution of another ARE represented in (2.6.11). $\mathbf{V_n}$ is a diagonal matrix whose entries contain the variance of the noise terms in the measurements [55].

$$\mathbf{A}^T \mathbf{P}_o + \mathbf{P}_o \mathbf{A} - \mathbf{P}_o \mathbf{C} \mathbf{V}_n^{-1} \mathbf{C}^T \mathbf{P}_o + \mathbf{V}_d = 0 \tag{2.6.11}$$

$\mathbf{V_d}$ contains the variance of the disturbance terms. Thus, if the Kalman gain $\mathbf{G}$ is chosen such that the system $(\mathbf{A} - \mathbf{GC})$ is asymptotically stable, then $\mathbf{e}$ will tend to $\mathbf{0}$.

2.7 Summary

This chapter focuses on reporting the mathematical foundations of the ERA system identification method and the linear quadratic Gaussian controller. In contrast to the phenomenological derivation of the model based on its physical parameters, the ERA approach presents a system identification procedure with a practical application approach where measurements are directly taken at the system's inputs and outputs to be identified. The inputs are represented by the active-reactive power injections of the battery-based systems and the outputs are represented by the frequency and voltage measured by PMUs. Since a black box model identification algorithm is performed, detailed knowledge of the internal parameters and physical laws relating to the network variables can be neglected, which makes this methodology suitable for the identification of multi-area networks, providing a reduced order model but with sufficient accuracy for its application in the controller. This chapter also presents the basic theoretical concepts for the development of LQG controllers that are used to estimate the optimal control action for each area of the network that minimizes the amount of energy needed to achieve voltage and frequency regulation, considering that the actuators are battery-powered systems whose lifetime depends on charge and discharge cycles. This chapter also reports the models used in experimental tests for the BESSs, EV chargers, batteries and synchronous generators and multi-machines power systems.

Chapter 3

Coordinated Controller for Voltage and Frequency Support in Transmission Networks

This chapter presents the implementation of a hierarchical control system to regulate frequency and voltage in transmission networks by taking advantage of active and reactive power injections from battery energy storage systems. This control scheme is tested in several simulated scenarios with significant load changes and three-phase faults. The proposed control approach is tested on a Matlab & Simulink™ model of the modified Kundur network with 4 areas and 8 synchronous generators.

3.1 Real-Time Hierarchical Control Architecture and BESS Topology

The proposed control framework takes advantage of emerging communication technologies and the integration of advanced metering infrastructure in a real-time control scheme with a fast-response time. Optimal and timely regulation of grid frequency and voltage can be achieved by the controlled injection of active and reactive power from several BESSs installed at different geographical locations, but working in a cooperative and coordinated way [49].

The controller framework comprises two hierarchical categories: (*i*) a logical hierarchy for information management and (*ii*) a physical hierarchy with dynamic allocation of power injection points. The former includes four hierarchical levels to distribute the computations in multiple elements of the system, reducing communication latency, computational burden

and optimizing the batteries utilization. Meanwhile, the second hierarchical category reduces the spread of voltage or frequency disturbances towards neighboring areas, since the proposed scheme initially injects power only from the BESSs in the area where the contingency takes place. If the available capacity of these BESSs is not sufficient to compensate this contingency, a logical signal is sent to the surrounding areas to request support, activating the local BESSs, thus a cooperative compensation is achieved. A detailed description of the system components and their operation is given below [49].

The overall diagram of the proposed control scheme is depicted in Fig. 3.2. In this framework, The transmission system operator (TSO) schedules the grid operation on a 24-hour horizon and the regular execution of the system identification routines. The prioritization levels, operative limits and slope of the ramp-down process is assigned by the TSO. The LQG controller, hinged on the Bellman's principle, computes the optimal active and reactive power needed to compensate the contingency in each area. The aggregator implements a complete set of rules from the logical and physical hierarchical schemes, adding intelligence to the controller. Moreover, the element is used to compute the active and reactive power set points for each BESSs grouped in the area [49].

In this application, the BESSs work as actuators allowing to modify the frequency and voltage dynamics in the transmission network by injecting active and reactive power. Each BESS consists of a battery pack, an electronic voltage source converter (VSC), a controllers that regulate battery charge/discharge and reactive power injection, a battery management system (BMS), a phase-locked loop (PLL) synchronization system and a set of electronic filters. The phasor measurement units (PMUs) allow to remotely sense frequencies (f_j) and voltage amplitudes ($|V|_j$), transmitting their information in real time to TSO, LQG controllers and aggregators [49].

The proposed control structure reflects the scalability for larger transmission networks through the implementation of the layered information flow scheme in which the computational burden is distributed over multiple elements, taking advantage of modern digital communication systems (see Fig. 3.1). Thus, these computational elements can be implemented in a low-cost platforms with real-time communication. Additionally, the proposed physical hierarchy scheme allows the system to control each area through an independent controller that interacts with adjacent areas only in case the contingency spreads to these areas[49].

3.1.1 Logical hierarchical structure

The advocated logic controller consists of four levels of information flow, as detailed in Figs 3.1 and 3.3. In this scheme, the computational tasks are distributed to be executed on multiple aggregators and controllers. Thus, it reduces the computational burden, decreases the risk of total controller failure and increases the scalability of the control scheme for multi-area

networks [49].

First logical level

Here, the operation is scheduled on a 24-hour horizon by the TSO at the central controller, where the operating limits and the target values for frequency and voltage are defined

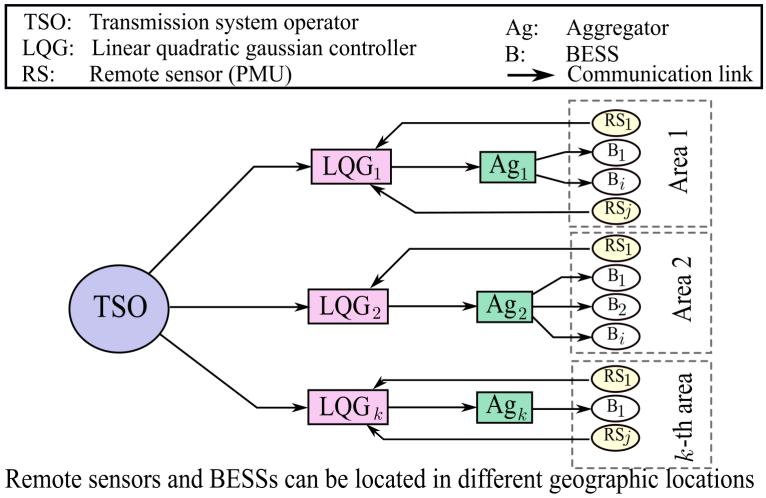

Figure 3.1: Proposed logical control architecture for information flow management.

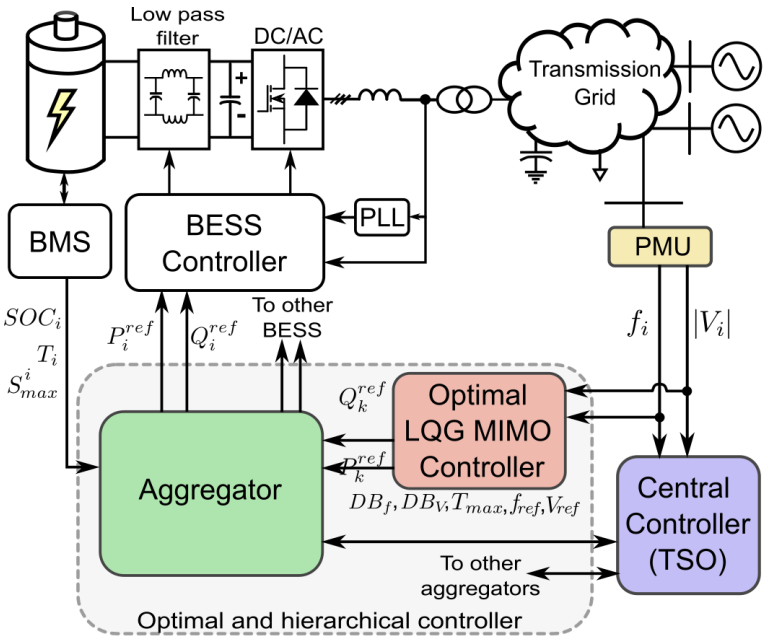

Figure 3.2: Overall diagram of the controller for frequency-voltage support.

as V_{ref} =1pu, f_{ref} =60Hz, respectively. Additionally, the TSO sets maximum operating temperature (T_{max}), SOC limits (SOC_{max} and SOC_{min}) and the weighting factor α_i for each BESS, depending on the injection capacity and chemistry of the batteries and electronic converter of each BESS. Furthermore, this controller is responsible of issuing the binary command M_{on} for the aggregator to execute the system identification routine [49].

Second logical level

In this level, the multiple-inputs multiple-outputs (MIMO) LQG controller optimizes the calculation of control actions (P_k^{ref} and Q_k^{ref}), minimizing the error and the energy needed to drive the controlled variables to the desired values in each area. At this level, the LQG control system compares the frequency (f_j) and voltage amplitude ($|V|_j$) measurements of each PMU with the set point signals provided by TSO (f_{ref} and V_{ref}). The design of the LQG controllers are detailed in Sections 3.2 [49].

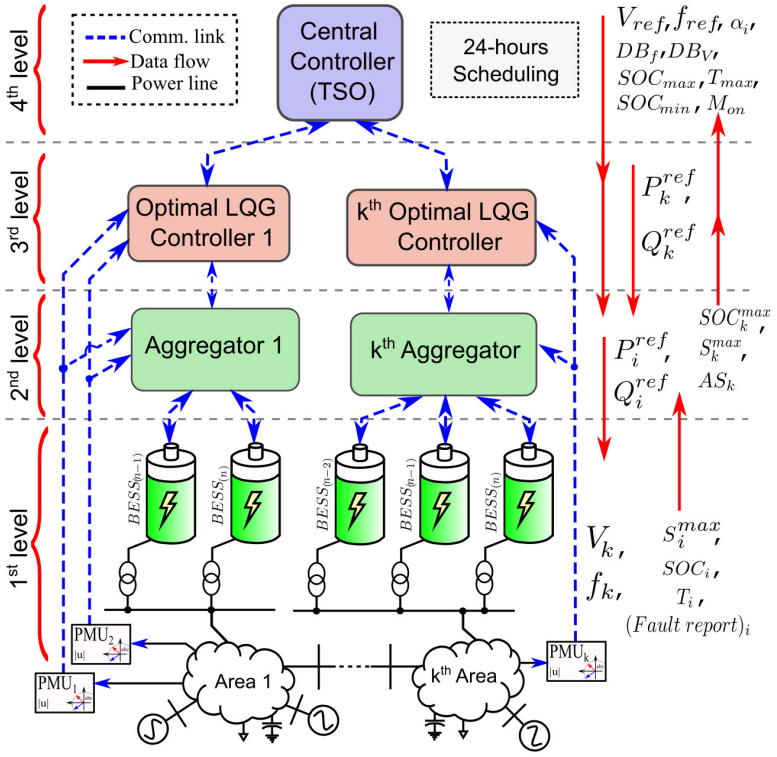

Figure 3.3: Logical architecture of the hierarchical control system.

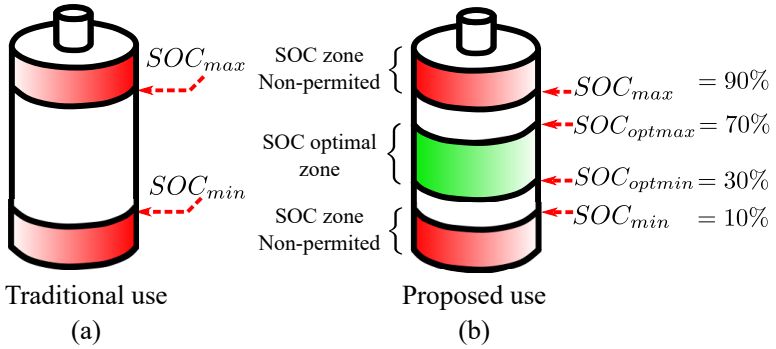

Figure 3.4: Logical architecture of the hierarchical control system.

Third logical level

In this level, the aggregating agents behave as intermediaries between each of the LQG controller and the total number of aggregated BESSs per area, reducing the computational burden of the TSO and adding intelligence to the controller in each area via **Algorithm 1**. The optimal control actions computed by the corresponding LQG controller and the security constraints of the BESSs are also incorporated into the algorithm running in the aggregator [49].

In this proposed scheme, the aggregator requests more power from the BESSs whose SOC is closer to the optimal level shown in Fig. 3.4, maximizing the utilization of the batteries in their optimum zone and balancing the capacity of BESSs per area according to their S_i^{max} and their current SOC_i. Thus, the TSO can prioritize the use of $S_i^{\max}$ or SOC_i through the proper choice of the weighting factor α_i $(0 \leq \alpha_i \leq 1)$, depending on the chemistry of the batteries and the operative limits of the power converter. The magnitude of active power to be injected for each BESS is determined according to (3.1.1).

Previous research has demonstrated that the SOC limits set for charging and discharging processes reduce batteries' service life and increase the risk of accidents for BESS operators [28, 58]. Manufacturers usually recommend the use of lithium batteries within the range 10%≤SOC≤90%. However, recent studies propose more moderate limits for their application in BESSs, e.g. 30%≤SOC≤70% [28, 58]. Thus, this concept is exploited in this work to assign optimal limits for the SOC at each BESS (SOC_{optmin} and SOC_{optmax}, respectively).

$$P_i^{ref} = \begin{cases} \left(\frac{\alpha_i S_i^{\max}}{\sum S_i^{max}} + \frac{(1-\alpha_i) SOC_i}{\sum SOC_i} \right) P_k^{ref} & ,\forall \quad P_k^{ref} > 0 \\ \left(\frac{\alpha_i S_i^{\max}}{\sum S_i^{max}} + \frac{(1-\alpha_i)(1-SOC_i)}{\sum (1-SOC_i)} \right) P_k^{ref} & ,\forall \quad P_k^{ref} \leq 0 \end{cases} \tag{3.1.1}$$

where P_i^{ref} denotes the active power required for each BESSs and P_k^{ref} is the optimum active power estimated by the LQG controller for the k-th area. This logical control structure

also prioritizes the injection of active power towards the grid ($P_k^{ref} > 0$) from BESSs with high SOC and the absorption of power from the grid ($P_k^{ref} \leq 0$) towards the BESS batteries with low SOC, encouraging the charging or discharging of the batteries to keep the SOC in the optimal zone (Fig. 3.4), while simultaneously BESSs provide frequency and voltage support to the transmission network [49].

On the other hand, the total available capacity of the BESSs per area to inject reactive power can be expressed as follows

$$Q_k = \sqrt{(\sum S_i^{max})^2 - (P_k^{ref})^2} \tag{3.1.2}$$

The requested reactive power (Q_i^{ref}) of each BESS is proportionally calculated considering the available capacity, such that

$$Q_i^{ref} = \left(\frac{Q_i^{max}}{Q_k}\right) Q_k^{ref} \tag{3.1.3}$$

The aggregator also incorporates a routine that shifts the power injection commitment from the BESSs to the SGs, reducing the battery usage. The ramp operation is shown in Fig. 3.5. When the contingency occurs, deviations of frequency and voltage of the power system outside the established operating limits are detected, as is depicted at time t_1 in Fig. 3.5 (a). In response to the contingency, the proposed hierarchical control system requests power from the BESSs and the AGC system requests power from the SGs, as shows in Figs. 3.5 (b) and (c), respectively. Due to the high inertia of SGs, the most significant power injection between t_2 and t_3 is provided by the BESSs. When the frequency and voltage return within the admissible operating limits at t_3, the BESS starts a reduction of power injection in ramp-down, whose slope is assigned by the TSO. Between t_3 and t_4, the batteries usage is gradually reduced until their power injections reach zero at t_4, giving enough time for the SGs to assume the power injection required to support the change in demand with their turbine control systems [45], as depicted in Fig. 3.6. In this scheme, the conventional speed controller is enhanced by incorporating a linear control (highlighted in green in Fig. 3.6) to reduce the error between the machine angular frequency (ω_g) and the expected angular frequency ($\omega_o = 2\pi f_{ref}$). Where p_{m0} and p_L stand for the initial mechanical power output of the steam turbines and power demand, respectively. The time constants of the SGs (T_p, T_s and T_z) and the inertia constant of the system (H_g) determine the inertial behavior and the primary frequency response of each synchronous generator [49].

As additional safety precaution against short-circuits, the proposed controller waits for 6 cycles of the fundamental frequency of the grid (between t_1 and t_2) and continuously checks the voltage amplitude to prevent the injection of active power that may aggravate this type of contingency. If the short-circuit is ruled out, then the process of network support through the BESSs can continue [49].

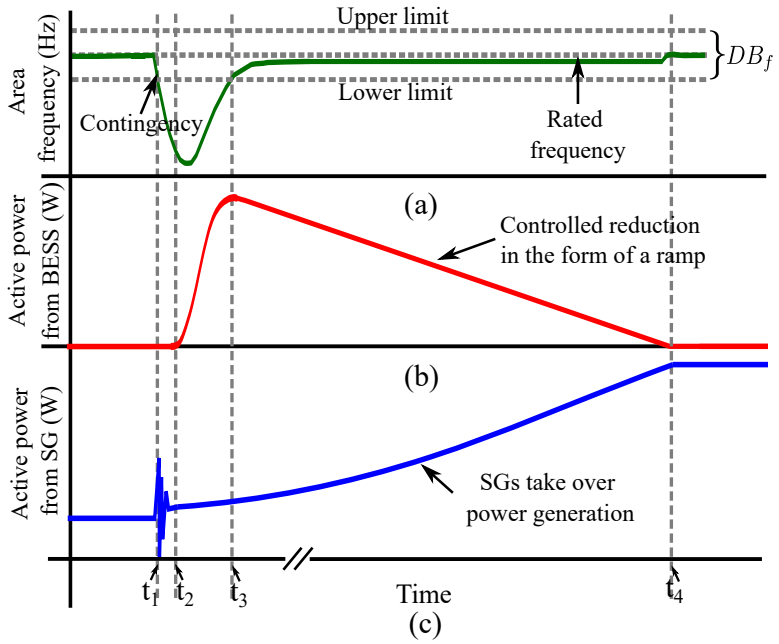

Figure 3.5: Ramp to transfer voltage and frequency support from BESSs to SGs.

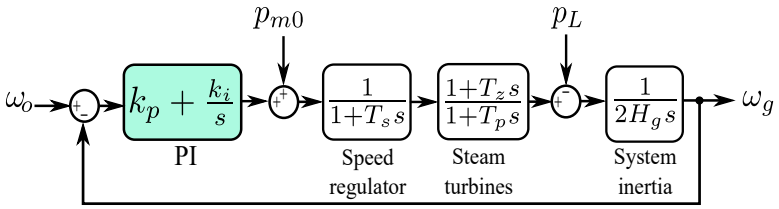

Figure 3.6: Block diagram of the enhanced speed controller.

In addition, the aggregator has the ability to run the model identification algorithm of the power system [49].

Fourth logical level

In the fourth level, all BESSs aggregated per area provide simultaneous injection of active and reactive power into the grid, responding to the power commands sent by the aggregator located on the second level. Meanwhile, the BMS of each BESSs transmits to the aggregator the operating temperature information (T_i), the maximum apparent power injection capacity (S_i^{max}), the state of charge (SOC_i) and the fault report per BESS. Nowadays, the maximum capacity of BESSs is hundreds of MVAr [59]. However, the combined action of several BESSs working in coordination allows reaching a capacity of GVA [28], which is harnessed in our proposal [49].

Our hierarchical and smart controller is able to recognize a contingency when the

Algorithm 1 Aggregator routine.

Input: P_k^{ref},Q_k^{ref}, f_{ref}, V_{ref}, f_k, V_k, S_i^{max}, SOC_i, T_i, T_{max} and α_i
Output: P_i^{ref}, Q_i^{ref}, AS_k
Initialisations: $S_{total} = 0$; $SOC_{total} = 0$
$S_k^{ref} = \sqrt{(P_k^{ref})^2 + (Q_k^{ref})^2}$
$\Delta f = f_k - f_{ref}$; $\Delta V = V_k - V_{ref}$
for $i = 1$, $i++$ to $i = n$ **do**
    if $0.3 \leq SOC(i) \leq 0.7$ && $T(i) < T_{max}$ **then**
        S_{total}=$S_{total} + S^{max}(i)$
        SOC_{total}=$SOC_{total} + SOC(i)$
    end if
end for
if $S_k^{ref} \leq S_{total}$ **then**
    $P_k = P_k^{ref}$; $Q_k = Q_k^{ref}$; $AS_k = 0$
else if $P_k^{ref} \leq S_{total}$ **then**
    $P_k = P_k^{ref}$; $Q_k = \sqrt{(S_{total})^2 - (P_k)^2}$; $AS_k = 1$
else
    $P_k = S_{total}$; $Q_k = 0$; $AS_k = 1$
end if
for $i = 1$, $i++$ to $i = n$ **do**
    if $SOC_{optmin} \leq SOC(i) \leq SOC_{optmax}$ &&
     $T(i) < T_{max}$ && ($\mid \Delta f \mid \leq DB_f \parallel \mid \Delta V \mid \leq DB_V$) **then**
        Execute eq. (3.1.1)
        if $\mid P(i) \mid \leq S^{max}(i)$ **then**
            Execute eq. (3.1.2)
            $Q_{total} = Q_{total} + Q^{max}(i)$
        else
            $Q^{max}(i) = 0$;
        end if
        Execute eq. (3.1.3)
    else
        Start ramp function.
    end if
end for
if $M_{on} == 1$ **then**
    To execute the ERA identification routine.
end if

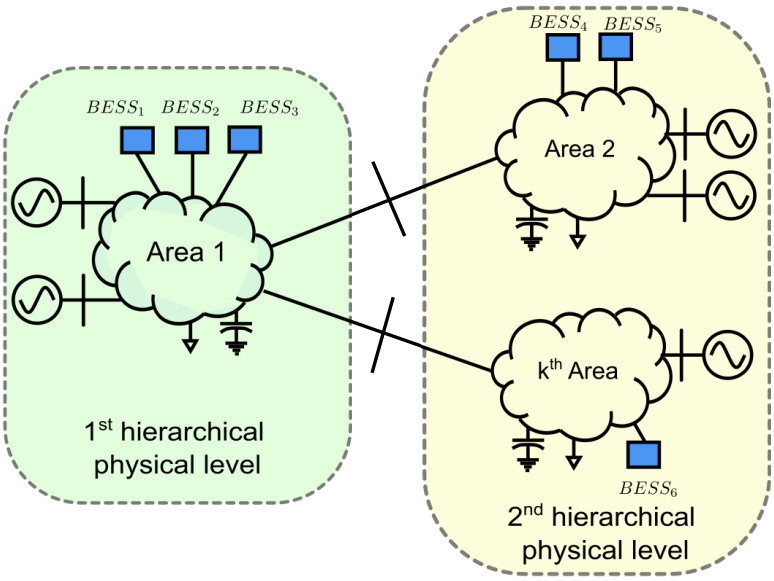

Figure 3.7: Assignment of physical hierarchy level.

measured values for frequency or voltage are outside the permissible dead bands (DB_f and DB_V stand for frequency and voltage deviations respectively). Note that these dead bands are primarily necessary for two purposes, which are: (*i*) to establish the requirements of the grid code [1, 16]; and (*ii*) to reduce unnecessary control actions and battery usage and in turn, increasing its operational safety.

3.1.2 Physical Hierarchical Structure

At this level, the proposed control scheme considers a finite set of non-overlapping control areas. These areas could be the same as the operator defined for the automatic generation control. Each area contains synchronous generators, BESSs and metering devices such as PMUs [49].

When a contingency is sensed in any area, the first hierarchical physical level is assigned to this area and the adjacent neighboring areas sharing interconnection lines are mapped to the second hierarchical physical level, as shown in Fig. 3.7. Areas that share tie-lines with the second hierarchical level are referred to as the third hierarchical physical level and so on. Active and reactive power injections from the BESSs are prioritized in the area where the contingency is detected, i.e. at the lower hierarchical level [49].

If the power injection capacity of the BESSs aggregated in the contingency area is less than the requested power by the LQG controller and the contingency is spreading to the adjacent areas, then all BESSs belonging to the next hierarchical level are activated contributing symbiotically to the regulation. This strategy mitigates power imbalances locally inside the

contingency area with minimal disturbance to the dynamics of the rest of the system [49].

3.2 LQG and ERA Algorithms

The pseudo-code implemented for ERA and LQG approaches are summarized in **Algorithm 2** and **Algorithm 3**. The theoretical foundations of these methods are formally addressed in Chapter II [49].

For implementation purposes, the ERA system identification routine takes less than 10 seconds and it is only executed when structural changes take place in the network. Since the system is operating when this routine is running, voltage amplitudes and frequencies

---

Algorithm 2 Eigensystem Realisation Algorithm.

Require: Input sequence (u_i) corresponding to the chirp stimulation for each BESS and output sequence (y) corresponding to voltage amplitude and frequency. Both sequences with N samples.

Ensure: $r = \frac{N}{2} - 1$. ▷ r defines the dimension of the Hankel matrix and ensures that it is greater than the number of non-zero singular values in $\mathbf{H}_0$

1: To apply Fourier spectra to both input and output sequences, such that ▷

$$y^{\{j\}}(t) = \mathscr{F}^{-1}\left(\frac{Y(s)}{U_i(s)}\right) \tag{3.2.1}$$

where $U_i(s)$ =fft(u_i) and $Y(s)$ =fft(y).

2: To construct the Hankel matrix $\mathbf{H}_0$ and its shifted Hankel matrix $\mathbf{H}_1$ using $y^{\{j\}}(t)$, as in (2.5.5) for k=1 and k=2.

3: Singular value decomposition $\mathbf{H}_0 = \mathbf{U}\boldsymbol{\Sigma}\mathbf{V}^T$ (3.2.2) ▷
$\mathbf{U}$ and $\mathbf{V}$ respectively stand for left and right singular vectors in matrix form, satisfying $\mathbf{U}\mathbf{U}^H = I$ and $\mathbf{V}\mathbf{V}^H = I$.

4: To separate $\mathbf{H}_0$ into two components, a n large (nonzero in the case of noiseless measurements) and s small (zero in the case of noiseless measurements) singular values

$$\mathbf{H}_0 = \begin{bmatrix}\mathbf{U}_n & \mathbf{U}_s\end{bmatrix}\begin{bmatrix}\boldsymbol{\Sigma}_n & 0\\ 0 & \boldsymbol{\Sigma}_s\end{bmatrix}\begin{bmatrix}\mathbf{V}_n^T\\ \mathbf{V}_s^T\end{bmatrix} \tag{3.2.3}$$ ▷

5: To approximate the high-rank Hankel matrix $\mathbf{H}_0$ by a reduced-rank n matrix ▷

$$\mathbf{H}_0 \approx \mathbf{U}_n\boldsymbol{\Sigma}_n\mathbf{V}_n^T \tag{3.2.4}$$

6: To compute the state-space model in discrete-time formed by matrices matrices $\mathbf{A}$, $\mathbf{B}$, $\mathbf{C}$, $\mathbf{D}$ as

$$\begin{aligned}&\mathbf{A} = \boldsymbol{\Sigma}_n^{-\frac{1}{2}}\mathbf{U}_n\mathbf{H}_1\mathbf{V}_n^T\boldsymbol{\Sigma}_n^{-\frac{1}{2}};\ \ \mathbf{B} = \boldsymbol{\Sigma}_n^{\frac{1}{2}}\mathbf{Q}^T\\ &\mathbf{C} = \mathbf{P}\boldsymbol{\Sigma}_n^{\frac{1}{2}};\ \ \mathbf{D} = y(0)\end{aligned} \tag{3.2.5}$$

where unitary matrices $\mathbf{P}$ and $\mathbf{Q}$ produce $\mathbf{H}_1 = \mathbf{P}\boldsymbol{\Sigma}_n\mathbf{Q}^T$.

return $\mathbf{A}$, $\mathbf{B}$, $\mathbf{C}$, $\mathbf{D}$.

Algorithm 3 LQR and LQE offline process.

Input: $[\mathbf{A}, \mathbf{B}, \mathbf{C}, \mathbf{R}, \mathbf{Q}]$
Output: $[\mathbf{K}, \mathbf{G}]$
$\mathbf{V}_n = \mathbf{R}$ and $\mathbf{V}_d = 0$
$\mathbf{P} \leftarrow [\mathbf{A}, \mathbf{B}, \mathbf{R}, \mathbf{Q}]$
$\mathbf{K} \leftarrow [\mathbf{P}, \mathbf{B}, \mathbf{R}]$
$\mathbf{P}_o \leftarrow [\mathbf{A}, \mathbf{C}, \mathbf{V}_n, \mathbf{V}_d]$
$\mathbf{G} \leftarrow [\mathbf{P}_o, \mathbf{C}, \mathbf{V}_n]$
for i=1, i++ **do**
    if (Is the system performance ok?) **then**
        Break for
    else
        Update $\mathbf{R}$ and $\mathbf{Q}$
        if ($\mathbf{Q} \geq 0$ and $\mathbf{R} > 0$) **then**
            Update $\mathbf{K}$ and $\mathbf{G}$
        end if
    end if
end for
Return: $[\mathbf{K}, \mathbf{G}]$

experiment a maximum variation of less than 3%. This means that the short duration of the identification process and the reduced variations of inputs do not significantly disturb the network operation.

3.3 Implementation and Simulation Results

To validate the effectiveness of the proposed hierarchical control system for frequency and voltage support in transmission networks, a modified Kundur's system with four interconnected areas is simulated (see Fig. 3.8). Dynamic time-domain simulations are performed in the Matlab & Simulink™ environment, using a fixed step size and the Ode5 solver. The Kundur's transmission grid is widely used for studies on dynamic stability, power exchange, oscillation damping, among others. The modified system contains twenty-two buses and eight generators, each having a rating of 900 MVA, 20 kV and working with a fundamental frequency of 60 Hz.

The four areas are interconnected with weak tie-lines of 100km between buses 9, 10, 11 and 12. Four loads and four shunt capacitors are applied to the system at same buses. Each SG is equipped with controllers for the governors and power system stabilizers (PSS). The detailed model is introduced in the textbook of Prabha Kundur [2].

The test power grid is equipped with 7 BESSs, as shown in Fig. 3.8. Each BESS has the topology diagram shown in Fig. 2.1 and the rated parameters detailed in Table 3.3.

3.3.1 Simulation scenarios

Scenario 1. In this case, the performance of the power grid in response to a load increase

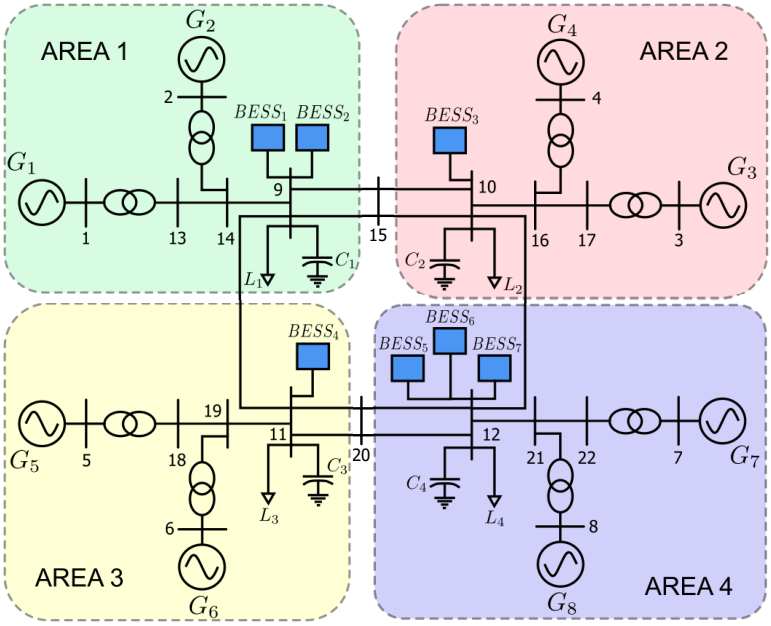

Figure 3.8: Modified equivalent Kundur's transmission network [2].

of 1000MW and 50MVAr at load L_1 is presented. The simulations are carried out with the proposed optimal hierarchical controller acting in open loop (Fig. 3.9), compared to the

Table 3.1: Synchronous generator parameters.

All parameters in p.u.							
x_d	x'_d	x''_d	x_q	x'_q	x''_q	x_l	R_s
1.8	0.3	0.25	1.7	0.55	0.25	0.2	0.0025
All parameters in seconds					**Rated values**		
T'_{do}	T''_{do}	T'_{qo}	T''_{qo}	–	S	V_{L-L}	f
8	0.03	0.4	0.05	–	900 MVA	20 kV	60 Hz
Inertia values in seconds							
H_1		H_2		H_3		H_4	
6.5		6.5		6.175		6.175	

Table 3.2: Simulation parameters of each BESS.

Parameter	**Value**
Rated battery voltage	800V
Lithium cells in series for battery packs	220 cells
BESS DC link capacitor bank (C)	3600μF
BESS grid-side inductance filter (L_g)	600 mH $\times$3
BESS DC-side inductance filter (L)	160 μH $\times$2
BESS DC-side capacitor filter (C_1, C_2)	120μF, 200μF
BESS controller Parameters (k_p and k_i)	k_p=1, k_i=5
Grid-side step-up transformer ratio	420V/230 kV$_{rms}$
Grid-side rated voltage	230 kV$_{rms}$
Simulation sample time	100μs

Table 3.3: BESSs capacity and initial SOC.

	Area 1		Area 2	Area 3	Area 4		
BESS number	1	2	3	4	5	6	7
Max. capacity (MVA)	450	450	150	150	450	400	300
Initial SOC (%)	40	60	40	40	40	60	50
Max. temp. (^{o}C)	150	150	150	150	150	150	150
α_i	0.6	0.5	0.5	0.6	0.5	0.4	0.6

closed loop system response (Fig. 3.10). In both simulations, the governor's controller and PSS of each SG are acting.

Scenario 2. This case simulates a three-cycle three-phase fault at node 15. The optimal hierarchical controller, governor's controllers and PSSs of each SG are working in closed loop. In this case, all loads and capacitor banks are maintained at their rated values.

Scenario 3. This case presents the behavior of the optimal hierarchical controller when the maximum BESSs capacity of the area is reached, in presence of a load increase contingency of 1000MW and 50MVAr at load L_1. These simulations showcase the coordinated power contribution provided by the BESSs of the neighboring areas. In this simulation the capacities

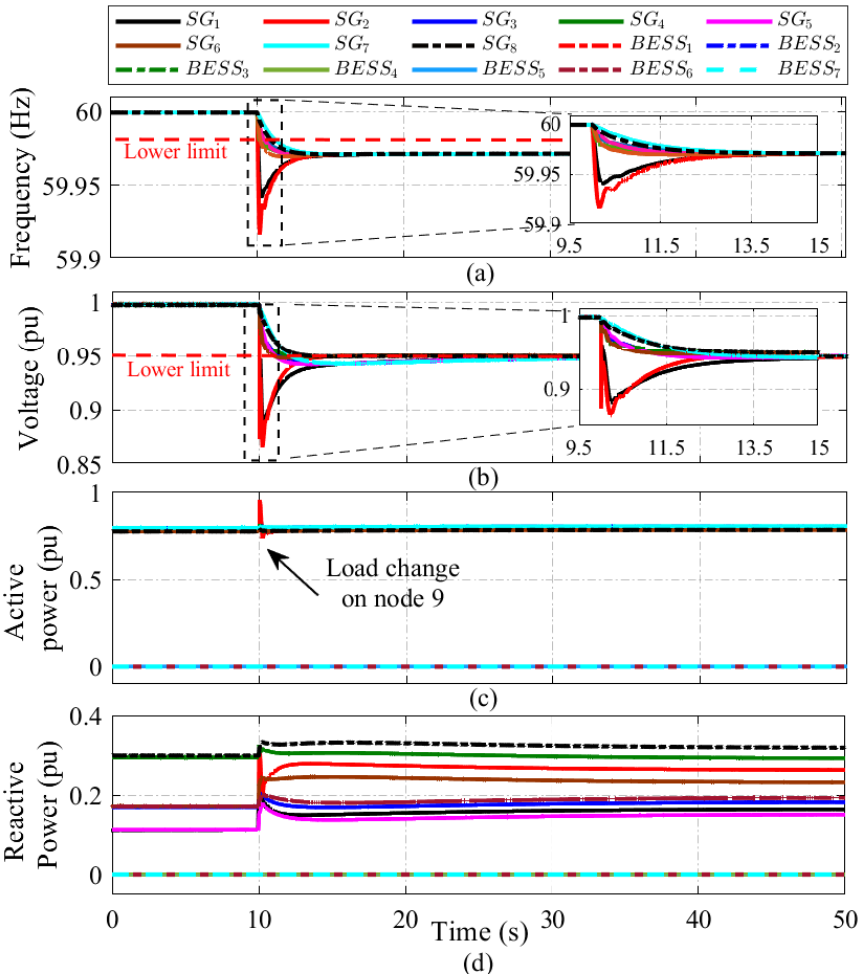

Figure 3.9: Simulation results for the open loop response in (*Scenario 1*). (a) Frequency response. (b) Voltage response. (c) Active power. (d) Reactive power.

of BESSs 1 and 2 are reduced to 150MVA, with respect to the parameters reported in Table 3.3.

3.3.2 Results

After running *scenario 1*, voltage and frequency responses of the grid are presented in Figs. 3.9 and 3.10. At 10 seconds, the load change contingency takes place causing frequency and voltage excursions throughout the entire network. In the open loop response, all frequency and voltage measurements indicate values below lower limits established for DB_V and DB_f, as points out the red dotted line in Fig. 3.9. In contrast, when the power grid is driven by the hierarchical controller in closed loop and a contingency is detected, all BESSs installed in area

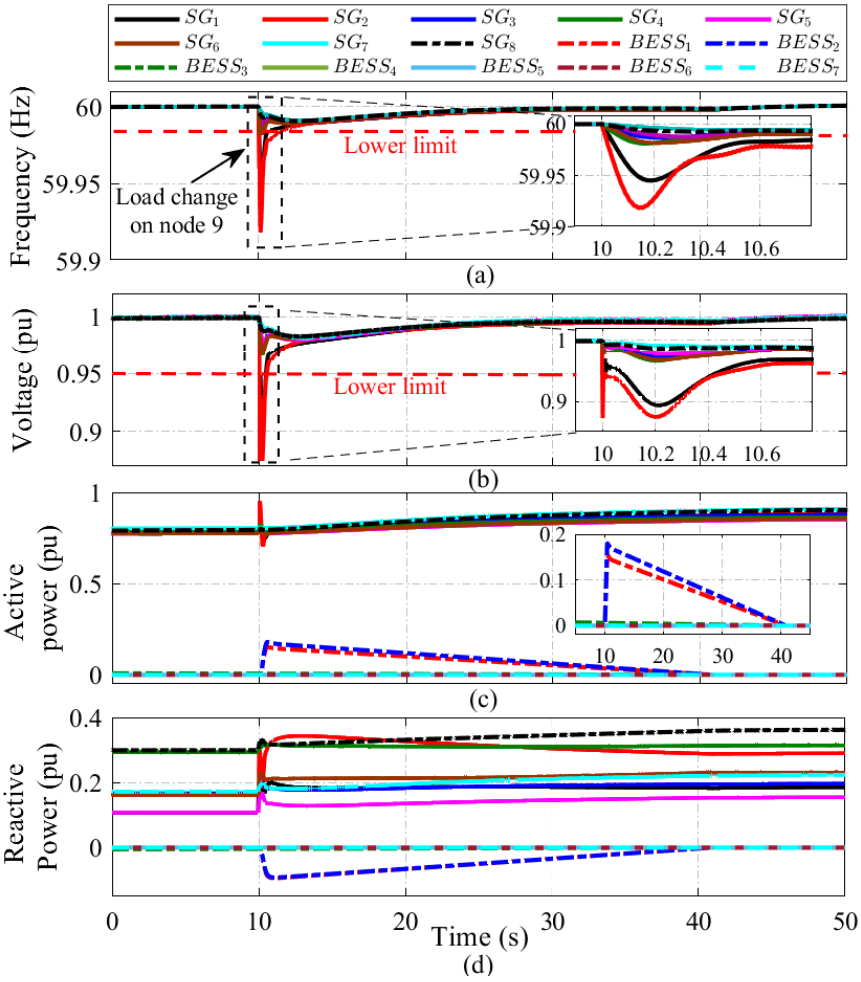

Figure 3.10: Simulation results for the closed loop with the power grid in (*Scenario 1*). (a) Frequency response. (b) Voltage response. (c) Active power. (d) Reactive power.

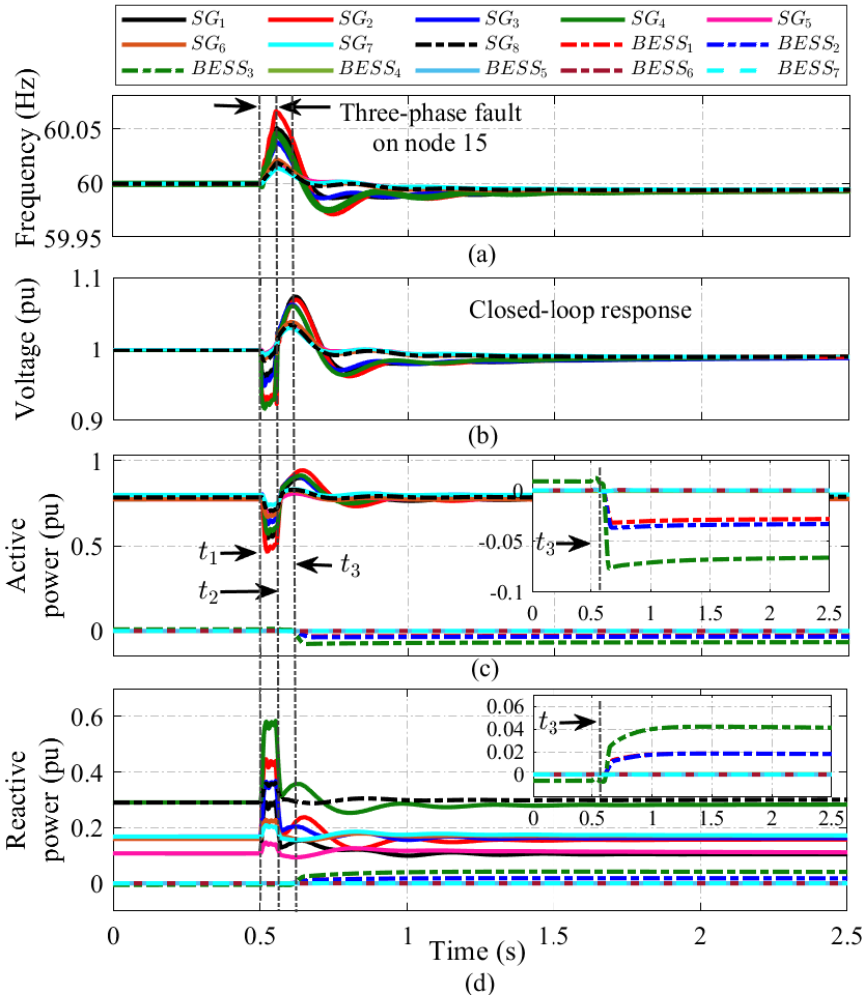

Figure 3.11: Dynamic response when a 3-cycle three-phase fault takes place at node 15 in (*Scenario 2*). (a) Frequency response. (b) Voltage response. (c) Active power. (d) Reactive power.

1 respond by fast injection of power to ostensibly improve the voltage and frequency profiles putting them back within the limits of the dead bands and close to reference values (V_{ref} and f_{ref}). For the closed-loop operation, the controller waits for 6 cycles of the fundamental frequency of the grid, verifying that the contingency does not correspond to a sustained short-circuit, subsequently starts the injection of active and reactive powers to compensate for the disturbance until the frequency and voltage return to the DB_V and DB_f limits, in less than 450ms. From that state, the power injection of all BESSs starts to ramp down, giving enough time for all SGs handling the power injection, which is completed in 32s.

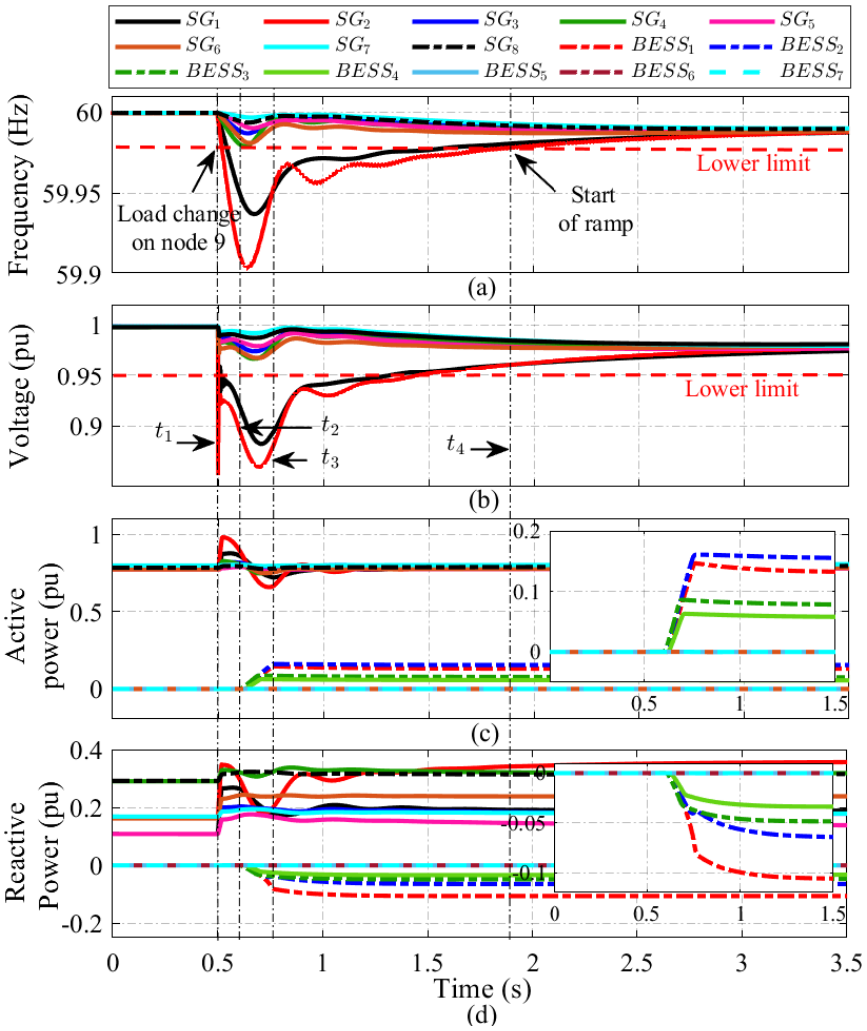

Figure 3.12: Power contribution provided by all BESSs of neighboring areas in the presence of a contingency caused by a load change at node 9 (*Scenario 3*). (a) Frequency response. (b) Voltage response. (c) Active power. (d) Reactive power.

Figure 3.11 details the dynamic responses for frequency and voltage throughout the network under the presence of a 3-cycle three-phase fault at node 15 in *Scenario 2*. At t_1, the fault event begins changing the voltage level and frequency significantly at all monitored points in the grid. The hierarchical control system starts the verification of 6-cycle to discard a sustained short-circuit. At t_2, the fault event ends, causing additional frequency and voltage deviations. At t_3, the short-circuit verification period ends and all BESSs react quickly injecting active and reactive powers to bring the frequency and voltage within the DB_f and DB_V limits, mitigating the effects of the fault. The steady state is reached in less than 1.5s. Subsequently, all power injected by the BESSs is ramped down.

Figure 3.12 displays the operation of the hierarchical control system in *Scenario 3*. At t_1, a frequency and voltage contingency is triggered by a load variation at node 9. The most significant voltage and frequency variations are in the area where the contingency takes place, i.e. Area 1. The hierarchical control system initiates the 6-cycle check to discard a persistent short-circuit, elapsing the time t_2, that is, when the optimal LQG controller calculates P_i^{ref} and Q_i^{ref} to request the injection of active and reactive powers from the BESSs in the Area 1. Likewise, the hierarchical controller (according to **Algorithm 3**) determines that the maximum capacity of the BESSs in Area 1 is less than the amount of power requested by the LQG controller and activates the power injection from the neighboring areas (Areas 2 and 3).

At t_3, the power requested by the LQG controller is reached from the BESSs. In the interval between t_3 and t_4, the power injection remains constant and below the maximum operating limits of the BESSs. In this period, the frequency and voltage variations are reduced, getting closer to f_{ref} and V_{ref}, respectively. At the instant t_4, the contingency disappears and frequency and voltage measurements on all buses are within DB_f and DB_f. At this instant, the ramp for the gradual reduction of the power injection from the BESSs starts. Under these conditions, the time required to compensate the contingency (from t_1 to t_4) is equal to 1.4s.

3.4 Discussions

Computational burden and complexity: the proposed control strategy represents an enhancement in terms of cost or computational burden compared to centralized control schemes, since this proposed hierarchical and layered control framework separates the computational tasks into several processing elements. These elements can be strategically located in the geographical space of the network area to reduce latencies in the digital communication process. As a reference of the computational load, Fig. 3.13 shows the execution time of the aggregator and LQG controller algorithms on a host computer with a 1GHz AMD Razor 5 processor, 20 GB of RAM and a 64-bit WIN10 operating system. Matlab & Simulink™ 2019a version was used for the simulations.

Despite the advantages of the proposed system mentioned above, the interconnection of multiple processing devices and the deployment of digital communication networks in real-time control schemes add complexity to the control system. In this scheme, the transmitted data should be encrypted to guarantee the flow's security. Data such as measurements results from the computation of the control actions, operating limit settings, among others. However, the distribution of computational tasks also reduces the risk of total collapse of the proposed support scheme, considering that some of the computational or communication elements are not operating in a given area, devices installed in neighboring areas could provide support in contingency events. This type of strategy also can be implemented using redundant execution of algorithms on multiple devices, thus reducing the risk of total system collapse.

Practicality: the design of the control schemes to be executed in each area is based on the identified low-order model provided by the ER algorithm. This identification and control scheme is advantageous because it allows scaling of the system to large multi-area networks. Since the control action with feedback, the scheme provides acceptable robustness to model accuracy and system parameter variation. However, the power system operator can request automatic execution of the identification algorithm with the desired regularity

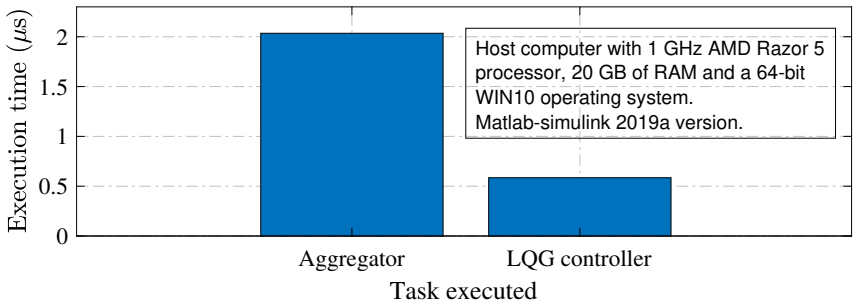

Figure 3.13: Execution time of aggregator and LQG controller algorithms.

or when considerable structural changes occur in the system. The proposed control scheme can also be tuned to the most complete and accurate models when they are available. The proposed localized control loops per area consider local frequency and voltage measurements. In addition, the strategic geographical location of the measurement, control and actuation elements, together with the application of high bandwidth communication systems, will reduce the latency, reducing its impact on the response of the control system. This control scheme imposes limits on the flow of potentially confidential information between areas and the system operator, reducing the exposure of sensitive information on the communication network. All control action calculations for the active and reactive power settings in each area are performed locally, reducing the interaction required to coordinate the different area controllers.

Initial investment cost: the battery-based systems represent the highest initial investment cost for the implementation of the proposed control scheme. Measurement, communication and processing devices have a relatively low acquisition cost compared to the actuating elements. Battery-based systems with capacities between 50MW and 450W are being built in the United States, Australia, Germany and Japan. As a reference of the possible cost of this type of project, Lithuania will build a battery storage system in which it plans to invest US$117 million to install four BESSs with at least 200MWh of storage capacity. The two largest lithium-ion battery projects announced will be deployed in California, USA. These are the Crimson Energy Storage (450 MW) and the Vistra Moss Landing Energy Storage (300 MW). Data provided by the U.S. Department of Energy database [59].

Although the recycling and reuse of batteries used for electric car traction is an issue receiving attention from governments, vehicle manufacturers and electric system operators, there is still an open discussion about what might be the best strategy. Some authors argue that one of the promising second-life applications for recycled automotive batteries may be the creation of battery energy storage systems to provide ancillary services to the grid. The practical implementation of this strategy requires additional studies for the modeling of battery degradation, determining the feasibility of a second life from an economic and technical point of view [60, 61, 62].

Identification challenges: the power system linear model from ERA technique is usually derived considering the impulse response, aiming to capture the system dynamics to be identified. However, in practice, the generation of an impulse signal is impossible to achieve. In this work, a pragmatic approach based on capturing the system dynamics using small amplitude and easy to generate Chirp signals is applied. Related functions are selected to stimulate the power system dynamics, preventing system disturbances and the excitation of non-linearities while running the identification algorithm.

3.5 Summary

The scope of this chapter is to present a novel hierarchical optimal control framework for frequency and voltage support in multi-area transmission systems integrating BESSs. The design is based on the coordinated active and reactive power injection of BESSs over conventional synchronous generator-based control for fast and timely mitigation of voltage and frequency deviations. The principle of this novel idea is to use two hierarchical schemes, one physical and one logical. The first scheme prioritizes the injection of energy from the BESSs installed in the zone where a contingency occurs, thus reducing the disturbance of the dynamics in neighboring zones. In the second scheme, operational rules are incorporated for the BESSs aggregated in each of them, increasing the operational security of the asset. The proposed approach exploits the advantages of time-synchronized measurements, the eigensystem realization identification technique, the linear quadratic Gaussian optimal controllers, and an aggregating agent that coordinates the power injection of the BESSs in a hierarchical and scalable scheme to precisely regulate frequency and voltage in modern transmission networks, increasing their reliability and stability. The feasibility and robustness of the proposal are demonstrated using simulated scenarios with significant load changes and three-phase faults in a modified Kundur system with four interconnected zones, mitigating frequency and voltage contingencies in less than 450ms. The concepts and results presented in this chapter have been published in the paper [49].

Chapter 4

Coordinated Controller for Voltage Profile and Decongestion Support in Active Distribution Networks

In this chapter, the development of an optimal hierarchical controller for voltage profile support and decongestion of distribution networks by injecting reactive power from electric vehicle chargers is presented. The effectiveness of this controller is verified in study cases with simulated scenarios under conditions of load changes, three-phase faults, input noise and communication signal latency. The stability and performance of the proposed scheme are tested in Matlab & Simulink™ models of the standard IEEE 13-node and 123-node test feeders.

4.1 Hierarchical Control Architecture and EV Charger Topology

Distribution networks are in a continuous transformation from passive to active networks, harnessing the rapid development of emerging communication technologies and the integration of advanced metering infrastructure [63]. In this promising and novel paradigm, a considerable rising in measurement devices, such as D-PMUs and other smart meters are expected to enhance the observability and understanding of the dynamic grid behavior. Furthermore, frequent changes in network configuration, including commercial-off-the-shelf converters for which manufacturers do not provide any behavioral model, make no feasible the theoretical or phenomenological modeling. Proliferating the use of system identification-based techniques which are chosen as the best option to identify the changing model of the

grid interfaced with power electronic converters [64, 12, 8].

Due to the high penetration levels of DERs and expected dynamic loads, traditional slow-change distribution grids are gradually turning to a multi-source grid with faster dynamics. Consequently, new challenges arise and must be addressed, taking advantage of the dynamic control structures; among them, ADGs must be optimally operated by applying the sophisticated control capabilities provided by DERs, such as EV chargers [40, 19]. The operation of ADGs can be classified into: (*i*) real-time operation, when control actions and commands takes place in short periods and they are transmitted using communication systems; (*ii*) scheduled operation, in which power generation is planned gathering the forecasting demand for one or more days [12, 8].

During the last decade, the increasing attention has been paid to the real-time monitoring of reactive powers and voltages in ADGs [64, 65]. Although there are promising and attractive control architectures such as distributed control [64], the bibliographic review shows that a high percentage of the previous works propose centralized and local control architectures [12]. In this way, this work proposes a hybrid hierarchical control framework for greater flexibility, combining local and centralized controllers advantages. The proposed control approach consists of multiple and remote measurement points provided by D-PMUs [43, 66, 67]. Numerous parking lots (a set of EV chargers) at different geographic locations work together (Fig. 4.2), to promptly regulate the voltage through the reactive power handling. In this context, the proposed control system can effectively interact with traditional voltage controllers present in the DSs, such as capacitor banks, on-load tap changers, and PV inverters. The proposed controller responds to the voltage measured variations at the observable nodes, complementing the control actions of the traditional voltage controllers. Thus, traditional voltage controllers contribute to the proposed approach, reducing the power required to be injected by the parking lots [1, 8].

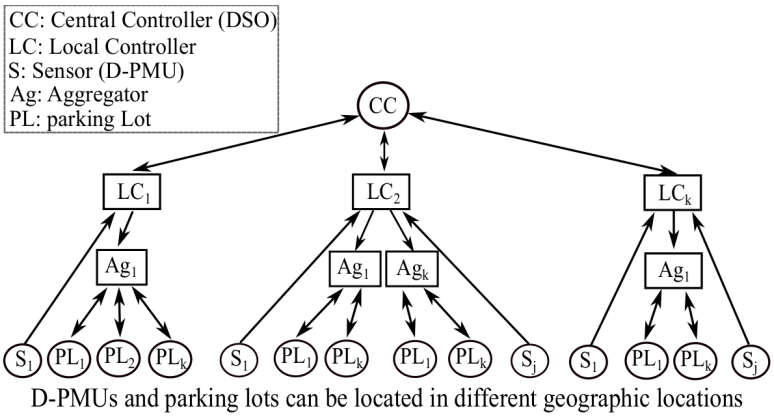

Figure 4.1: Proposed Voltage control architecture.

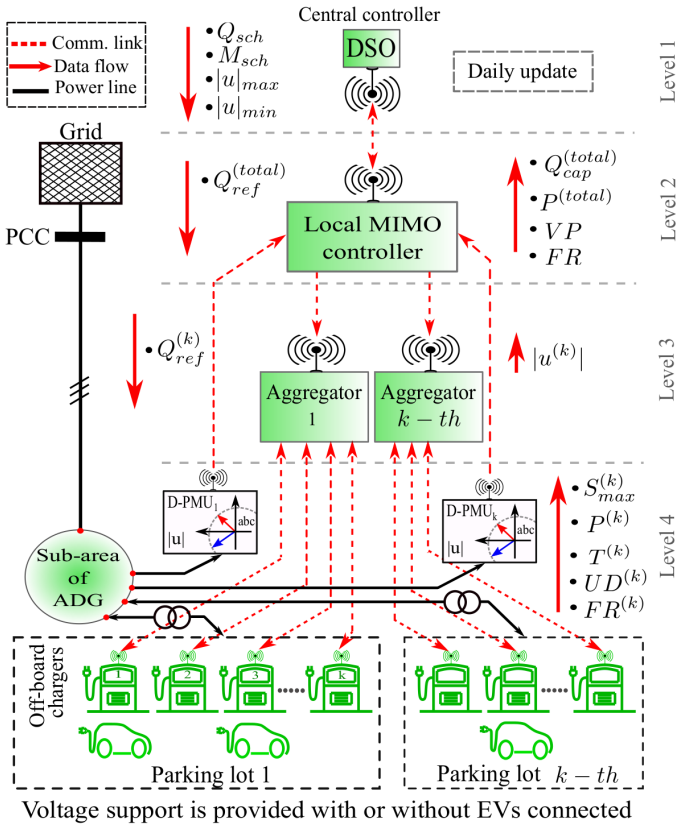

Figure 4.2: Parking lot architecture with EV battery chargers and D-PMUs.

4.1.1 Logical hierarchical architecture

The proposed approach has four levels of information flow, as detailed in Figs 4.1 and 4.2. In the first level, the central controller performs day-ahead scheduling of operation for each local network controller to estimate the voltage regulation capacity for grid support, meanwhile, the EV owners and grid constraints are satisfied. This central controller schedules and updates the reactive power limits (Q_{max}) and the reference voltage levels ($|u|_{max}, |u|_{min}$) for the entire DG, by coordinating the operation of each local controller that regulates the voltage at each sub-area in the DG. The establishment of these limits is aimed to prevent the compensation made by the local controller from negatively affecting the operation of neighboring local controllers in other sub-areas. Additionally, this controller is in charge of issuing the binary command so that the local controller executes the system identification routine in the controlled sub-area (M_{sch}). This kind of controllers has been extensively studied in the technical literature [12]; consequently, our proposal focuses on the development of the local controller and its interaction with the central controller [8].

In the three lower levels, the elements of local controllers are located. These controllers timely and precisely regulate the voltage level at each sub-area in the DG, making the system

scalable and flexible. In this work, the operation of local controllers is foreseen in real-time, considering a latency or delay round-trip of data (D_{rt}) less than $50ms$. The communication technologies LTE-M2M, HSPA-M2M and Precision Time Protocol (PTP) IEEE Std 1588, based on ethernet networks allow achieving an average latency between $100\mu s$ and $40ms$ with a wide spatial coverage range, and a large number of smart devices connected using various heterogeneous networks topologies. The total signal latency can be defined by $T = T_s + T_b + T_p + T_r$, where T_s is the serial delay, T_b stands for the packet delay, T_p corresponds to the propagation delay, and T_r represents the routing delay [68, 69, 70, 71, 8].

In the second level, the local controller compares the voltage magnitude ($|u^{(k)}|$) measured by each D-PMU with the reference signals from the central controller ($|u|_{ref} = 1$), calculating in closed-loop the control action ($Q_{ref}^{(total)}$) necessary for each set of EV chargers grouped by the aggregator. This local controller sends the following information to the DSO: the available reactive power injection capacity ($Q_{cap}^{(total)}$), the active power used in the eventual charging of batteries ($P^{(total)}$), the consolidated fault report (FR), and the network voltage profile (VP). Additionally, the local controller can automatically execute the model identification routines with the regularity programmed by the central controller, exciting the system dynamics with the chirp modulated signals.

Algorithm 4 Aggregator routine.

Input: $S_{max}^{(k)}$, $P^{(k)}$, $T^{(k)}$, T_{max}, n, $UD^{(k)}$ and $Q_{ref}^{(total)}$
Output: Q_{ref}^{k}
$Q_{cap}^{(total)} = 0$
$Q_{ref}^{k} = 0$
for $k = 1$, $k++$ to $k = n$ **do**
    if $UD^{(k)} = 1$ && $T^{(k)} < T_{max}$ **then**
        $Q_{cap}^{(k)} = \sqrt{(S_{max}^{(k)})^2 - (P^{(k)})^2}$
        $Q_{cap}^{(total)} = Q_{cap}^{(total)} + Q_{cap}^{(k)}$
    end if
end for
if $Q_{ref}^{(total)} > Q_{cap}^{(total)}$ **then**
    $Q_{ref}^{(total)} = Q_{cap}^{(total)}$
end if
for $k = 1$, $k++$ to $k = n$ **do**
    if $UD^{(k)} = 1$ && $T^{(k)} < T_{max}$ **then**
        $Q_{ref}^{(k)} = (Q_{cap}^{(k)}/Q_{cap}^{(total)})Q_{ref}^{(total)}$
    end if
end for

In the third level, the aggregator agents are located. They execute the routines in which receiving and processing the following information from each EV charger: the current active power injected $P^{(k)}$ and the apparent power capacity of each EV charger $S^{(k)}_{max}$; the operating temperature ($T^{(k)}$) of each charger; the decision of the parking lot administrator ($UD^{(k)}$), that is, whether or not to allow the provision of V2G services; and the report of failures ($FR^{(k)}$) of each charger. With this information, the aggregator runs the **Algorithm 1** to calculate the reactive power that each charger must inject ($Q^{(k)}_{ref}$) in direct proportion to its current power supply capacity ($Q^{(k)}_{cap}$), where n is the number of EV chargers grouped by the $k-th$ aggregator. In this approach, the aggregator acts as an intermediary between the chargers and the local controller, reducing the computing load for the local and central controllers [8].

In the fourth level, the remote measurement devices and the off-board EV chargers grouped at each parking lot are located. These devices are expected to be available in modern distribution grids [43, 19]. The D-PMU measurements are streamed in real-time to the local controller. Otherwise, each charger receives the $Q^{(k)}_{ref}$ command from the aggregator, and in turn, this regulates in a closed-loop the individual reactive power injected into the controlled sub-area of the DG [8].

4.2 Simulation tests

This work adopts the ERA-based system identification technique to estimate the state-space linear model representation for distribution grids. To this end, voltage magnitudes stemming from different D-PMUs are established as the output sequence; meanwhile, the input sequence is set by the exponential chirp function that modulates the reference reactive power (Q_{ref}) at every parking lot. The voltage controller that regulates the reactive power supplied by the EV chargers adopts a system identification provided by the eigensystem realization to feed a control structure driven by a LQG controller. This control structure maintains high flexibility for adapting to the state-space system in (2.5.15). It is composed of a LQR that compensates the voltage sag/swell, taking into consideration the distribution system model drawn by the ER method through a frequency sweep in a selected frequency range. Thus, Bellman's principle of optimality that makes up the LQR design is tackled in the following.

The control inputs of EV chargers are feedback by the control actions that respond to the voltage magnitude variations measured by the D-PMUs, providing a remotely controlled system. Furthermore, the ER-based system identification routine takes less than 2 seconds for running and only runs once. When the identification routine is running $Q^{(total)}_{ref}$ is replaced by a CMS with a frequency range within [1Hz - 1kHz] and the maximum amplitude of 5MVar. In turn, the aggregator coordinates the injection of reactive power for each EV charger, and the voltage amplitude is monitored through the D-PMUs, exhibiting a maximum variation

of amplitude less than 3% in compliance with the ANSI Standard [1]. That is, the short time duration of the data-driven model identification process and the reduced amplitude does not significantly disturb the grid operation from normal conditions. Then, the LQG design is conducted by solving the discrete-time ARE to achieve the state feedback gain ($\mathbf{K}$) and Kalman gain ($\mathbf{G}$) matrices in (2.6.4) and (2.6.10), respectively. This is carried out using the Markov parameters provided by the ER-based identification and the Matlab function *dlqr*. Dynamic time-domain simulations are performed in the Matlab & Simulink™ environment, using a fixed step size and the ODE5 solver.

The effectiveness and feasibility of the proposed hierarchical optimal controller, applied on active distribution feeders, are verified by means of two case studies: *(i)* the voltage regulation action is depicted in section 4.3 and *(ii)* the increase of operational flexibility by decongesting the distribution lines is shown in section 4.4.

4.3 Case 1: Vol/Var Control in Active Distribution Feeders

The straightforward implementation for the hierarchical voltage control scheme with the architecture in Fig. 4.2 is established through the block diagram in Fig. 4.3.

4.3.1 System description

The feasibility and robustness of the proposed hierarchical control structure are assayed employing two IEEE test distribution feeders. They are the 13-bus and 123-bus feeders in [3] and [4, 5], respectively. Their one-line diagrams are depicted in Fig. 4.5 and Fig. 4.16, respectively. Both test systems are created and approved by the Distribution System Analysis (DSA) subcommittee, they represent reduced-order models of an actual distribution

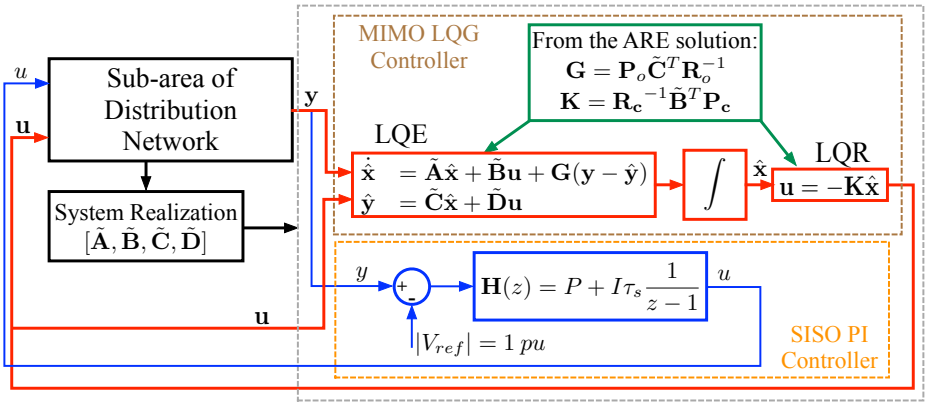

Figure 4.3: Block diagram for the voltage controller implementation based on ER and LQG.

Table 4.1: Simulation parameters used for voltage regulation.

Parameter	***Value***
Nominal voltage and rated battery capacity	380V, 5.4x70Ah
DC link reference voltage (v_{dcref})	800V
DC link capacitor bank (C)	3600μF
DAB leakage inductance (L_t)	1.5 μH
DAB transformer ratio	400/800 V_{rms}
VSC inductance filter (L)	600 μH $X3$
Grid side transformer ratio	480/4160 V_{rms}
Simulation sample time	50μs

circuit, operating at 4.16 kV. The 13-bus feeder is characterized by being short, relatively highly loaded, a single voltage regulator at the substation, overhead and underground lines, shunt capacitors, and unbalanced loading [72]. The 123-bus feeder is considered since it provides voltage drop problems and it is ideal for the voltage regulators and shunt capacitor testing, also making it suitable for dynamic voltage control that is the objective of this investigation. This feeder is distinguished by overhead and underground lines, on-load tap changers, multiple switches, shunt capacitor banks, and unbalanced loads represented by constant current, impedance and power models [4, 5]. As stated by Section 4.1 and Fig. 2.2, every charger is equipped by a VSC and a DAB. Both VSC and DAB are implemented under the parameters in Table 4.1, yielding in Fig. 4.4 the waveforms corresponding to the voltages, currents, and powers of the EV battery charger under changes in their references for reactive $Q_{ref}^{(k)}$ and active $P_{ref}^{(k)}$ powers. These changes are illustrated in Fig. 4.4(a), where the PI controllers track the changes on the reference requested by the aggregator, injecting both powers into the PCC. The step-type changes in $P_{ref}^{(k)}$ exhibit the charge and discharge of the battery bank. Similarly, the step-type changes in $Q_{ref}^{(k)}$ confirm the charger's ability to inject inductive and capacitive reactive powers, working in the four quadrants of the $P-Q$ plane. Meanwhile, the currents at the DC bus (i_{dc}) and at the battery (i_{bat}) proportionally change concerning the active power, as shown in Figs. 4.4(b)-(c). Likewise, the VSC regulates the voltage on the DC link, keeping it around the point of operation (800V), Fig. 4.4(b).

For the simulation analysis, four scenarios are managed. The first three scenarios seek to test the performance of the local controller on the 13-node test feeder, and the fourth scenario demonstrates the hierarchical control system performance scaled to the 123-node

Table 4.2: parking lots reactive power capacity.

Test feeder	**Parking Lot (PL)**	**Number of EV chargers**	**Nominal reactive power (MVar)**
13 nodes	PL1	20	7
	PL2	12	4.2
123 nodes	PL1 - PL7	5 (35)	1.75 (12.25)

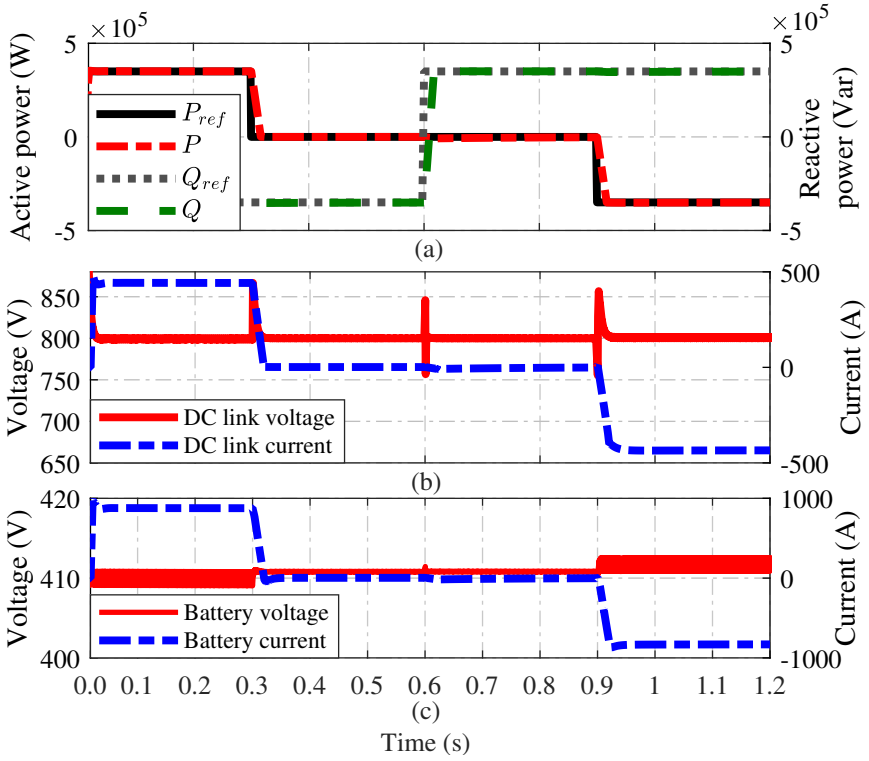

Figure 4.4: Waveforms of voltages, currents and powers for the EV battery charger.

test feeder and three local controllers working cooperatively. The 13-node test feeder, shown in Fig. 4.5, comprises two D-PMUs and two parking lots. The parking lot 1 can inject up to 7MVar (upon request) based on the connection of 20 EV-chargers in shunt connection. Similarly, the parking lot 2 contains 12 EV-chargers with the capacity to provide up to 4.2MVar (upon request). The 123-node test feeder is composed of three sub-areas whose voltage levels are regulated by three local controllers, as shown in Fig. 4.16. Controllers in areas **I** and **II** include two D-PMUs and two parking lots; meanwhile controller in area **III** comprises two D-PMUs and three parking lots. In the 123-node test feeder, all parking lots can inject up to 1.75MVar. Every charger installed at the parking lots can supply 350kVar at $420V_{LL}$. The parameters for each charger are presented in Table 4.1. At the PCC, a step-up power transformer adapts the voltage levels from $420V_{LL}$ up to $4160V_{LL}$, between the parking lots and the network feeder. As a reference, V3 supercharger from Tesla Motors can supply between 250kW and 350kW [73]. Similarly, the manufacturer ABB offers high power chargers up to 350kW [74].

4.3.2 Scenarios description

Scenario 1. In this case, both parking lots and both D-PMUs are respectively used as actuators and sensors for the control system in the 13-bus feeder, as exhibited in Fig.

4.5. Simulation is conducted with the MIMO LQG controller acting in closed-loop with the network in comparison with the open-loop system response.

Scenario 2. A performance analysis of PI and SISO LQG controllers in closed-loop concerning the open-loop response is devoted in this scenario by evaluating their responses in the 13-bus feeder. Parking lot 1 and D-PMU$_1$ represent the actuator and the sensor for the control system, respectively. Parking lot 2 and D-PMU$_2$ are not considered in this case, as displayed in Fig. 4.5. In this scenario a 570kVar capacitor bank is added at node 9.

Scenario 3. This case encompasses parking lots one and two and D-PMUs one and two. The simulation is conveyed employing the MIMO LQG controller, and it is contrasted with the open-loop system response in the 13-bus feeder.

Scenario 4. The dynamic response and scalability of the hierarchical system are tested on the IEEE 123-node test feeder by employing three local controllers and the DSO as a central controller. Simulations are executed with the MIMO LQG controllers working in closed-loop in comparison with the open-loop response.

In *Scenarios 2* and *3*, the load connected at node ten is increased 20 times to verify the robustness of the proposed control system for regulating the network voltage in the presence of extreme load disturbances, even when the system identification drawn by the ER is achieved under nominal operating conditions.

4.3.3 Results

The network voltage profile for the conditions in *Scenario 1* is presented in Fig. 4.6. When the system operates in open-loop, all buses, except the source, indicate lower voltage amplitudes than those suggested by the ANSI C84.1 standard [1], as exhibited by the dotted red line. When the closed-loop controller is enabled, the voltage profile improves significantly, settling its amplitude within limits established by the standard [1]. Voltage amplitude almost attains 1pu at the smart measurement location (D-PMUs installed at nodes 4 and 9).

The proposed hierarchical controller can improve the voltage profile of the distribution network, even in the presence of unbalanced voltages/currents, as illustrated in Fig. 4.7. Both measurement channels corresponding to the D-PMU$_1$ are polluted by adding a constant amplitude noise of $\pm 10\%$ to corroborate the noise tolerance in the proposed approach. The embedded FIR filter in the D-PMU$_1$ effectively rejects the electrical noise, and the measurement signal used in the control system is noise-free, as depicted the voltage amplitude by the dotted green line in Fig. 4.7. The unbalance voltages and phase shift between current and voltage in phase C, are due to the unbalanced reactive loads connected along with the network. However, the maximum variation of the voltage magnitudes is 0.93% (recalling that 5% is the upper limit reported in the ANSI C84.1 norm [1]).

Figure 4.8 depicts the reactive power profile for all buses in the network. The reactive

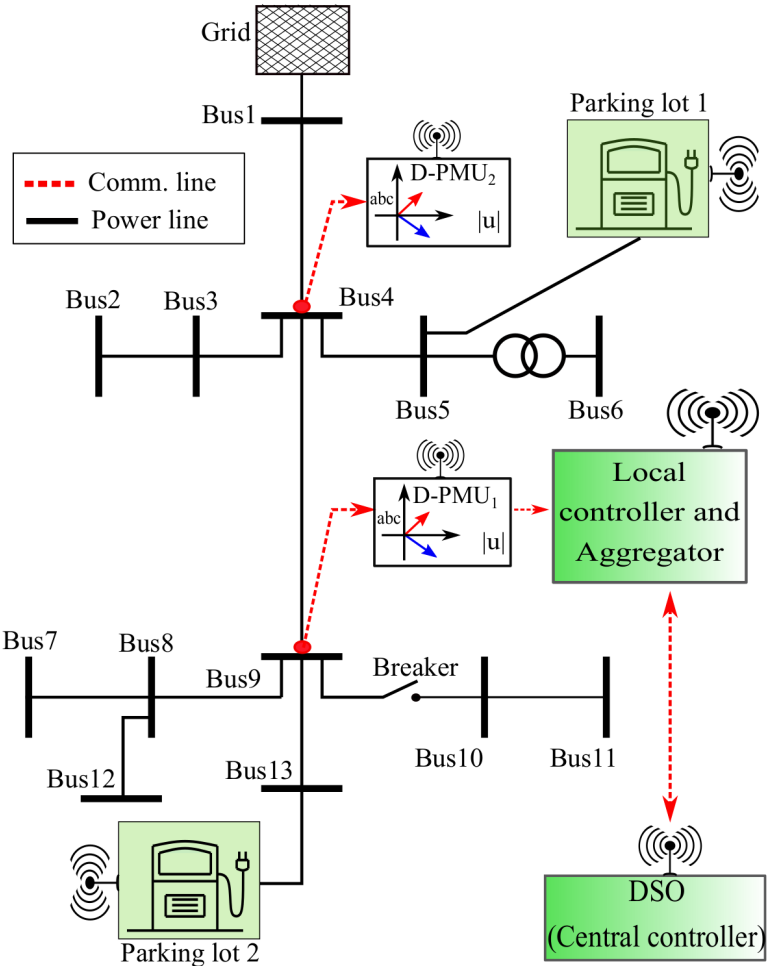

Figure 4.5: IEEE 13-node test feeder in *Scenarios 1-3* [3].

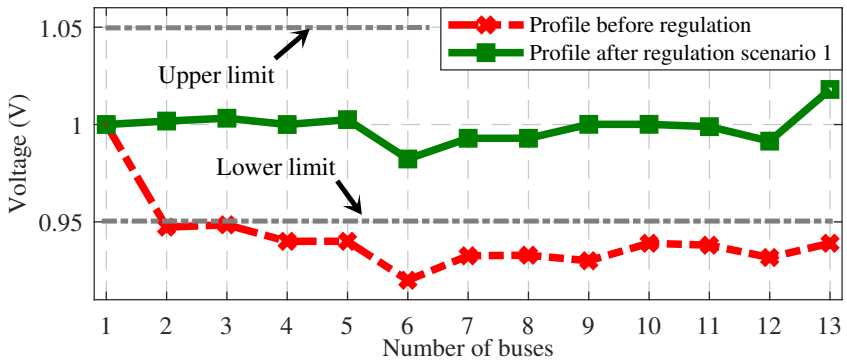

Figure 4.6: Voltage profile in *Scenario 1* for the closed-loop with MIMO LQG controller and open-loop system responses.

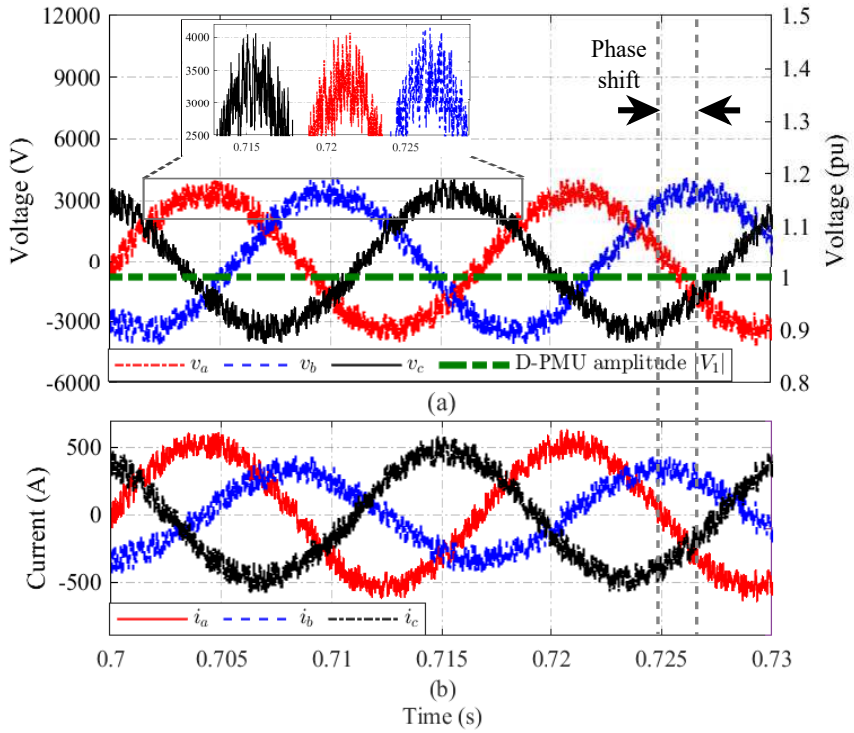

Figure 4.7: Noisy signals with unbalanced conditions at bus 9 in *Scenario 1.* (a) input/output D-PMU voltages (b) Currents

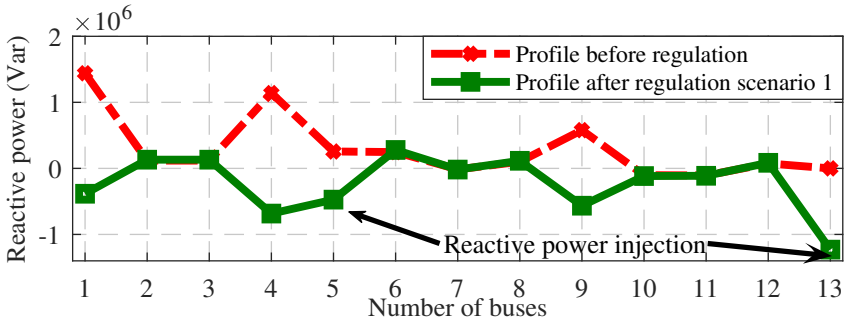

Figure 4.8: Reactive power profile before and after regulation in *Scenario 1.*

power is injected at nodes 5 and 13, as depicted in Figs. 4.8 and 4.9, causing that the voltage amplitude in those buses becomes more significant than that of the other buses (see Fig. 4.6). Simultaneously, the controlled injection of reactive power increases the network capacity to distribute active power, improving the power factor, as indicated at buses 4 and 9 in Figs. 4.9(a) and 4.9(b), and implying active power decongestion.

The dynamic response for the PI and the SISO LQG controllers concerning the DS open-loop response at node 9, with a significant change in load, is displayed in Fig. 4.10. At 0.5s, the circuit breaker is closed modifying the operating conditions of the network by adding load. Without a controller, the system operates outside the reliability enforcing limits established

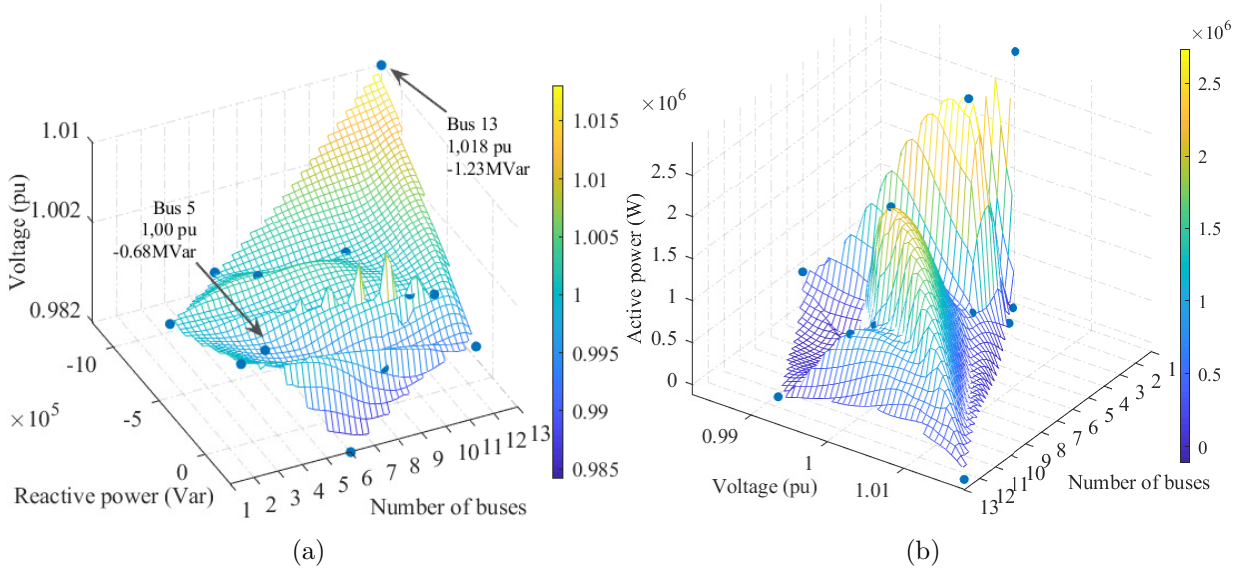

Figure 4.9: Power profile before and after regulation in *Scenario 1*.(a) Reactive power impacts. (b) Active power decongestion.

in the ANSI C84.1 standard (below 0.95 pu) [1], as shown by the red dotted line. At full load, the voltage drop of 14% is noticed. In contrast, the closed-loop system responses are illustrated by the black and green lines, respectively. With both controllers, the system is driven to the desired operating value (1pu). In these operating conditions, the LQG controller takes 205ms to reach the steady-state, and the PI controller takes 375ms. Simultaneously, the controlled reactive power injection increases the capacity in the network to distribute active power, improving the power factor, as shown at buses 4 and 9 of Fig. 4.13. It is important to remark that the settling time of the closed-loop system is largely dependent on the selected tuning parameters. The LQG controller is optimized to reduce the error between the measured signals and the desired value, whereas the PI controller is tuned using the pole-placement technique.

The voltage and reactive power at all buses during the highest load condition are depicted in Figs. 4.11 and 4.12, respectively. Under open-loop system conditions, the voltage profile throughout the network is below the standard limits [1], exhibiting high levels of reactive power at buses 4 and 9. This is a consequence of the connected loads on the adjacent branches. Whereas, the voltage profile in *Scenarios 2* and *3*, when the system operates in closed-loop with LQG controllers, is ostensibly improved by injecting reactive power from both parking lots. However, the LQG controller in case 2 only injects reactive power into node 5 supporting the voltage magnitude, which increases the voltage level close to this bus. The MIMO control strategy used in *Scenario 3* is more useful to improve the network voltage

profile (about 1 pu), injecting reactive power at buses 5 and 13.

The optimal way to structure the communications network remains a major challenge for future smart grid systems. However, previous studies show that latency can be reduced to values of the order of μs [69, 68]. The round-trip delay simulation, sketched in Fig. 4.14, considers a constant magnitude of the response latency to the measurement ($|u^{(k)}|$) and the control signal ($Q_{ref}^{(k)}$) between $0ms$ and $50ms$, as a whole, the round-trip delay can be up to $100ms$ in the feedback process. This latency takes into account the overhead of the control protocol, re-transmissions, and traffic congestion. The simulation results in Fig. 4.14 illustrates that although latency causes an increase in the overshoot of the measured and control signals, this overshoot does not negatively impact the voltage support that the local control system performs on the sub-area of the distribution network.

Figure 4.15 details the voltage and reactive power dynamic responses at each bus under a 3-cycle single-phase fault in the line a to ground at node 9, and a change of 20 times the nominal load. At t_1, the fault event starts by changing the voltage level of all nodes in the network significantly. The local control system and EV chargers quickly react by injecting reactive power up to their established operating limit to mitigate failure. At t_2, the fault event ends and the control system regulates the grid voltage profile within the standard limits in less than $220ms$ [1]. At t_3, the circuit breaker between bus 9 and bus 10 closes, supplying power to the loads connected at nodes 10 and 11. To confirm the robustness of the control system when its identified operating point is away from the region in which it works, the load is increased up to 20 times its nominal value. Under these conditions, the control system reacts by increasing the injection of reactive power at nodes 13 and 5 through the parking lots, to finally reach the steady state in less than $220ms$.

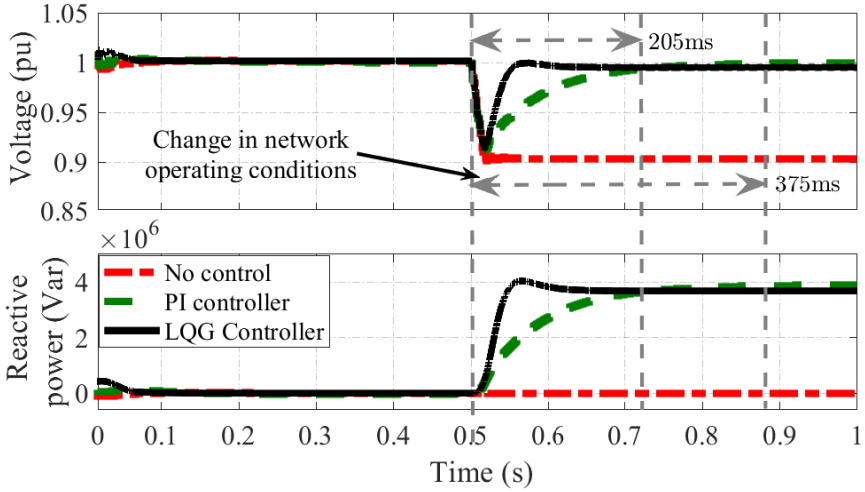

Figure 4.10: Voltage profile and reactive power response at node 9 in *Scenario 2* for the DS equipped with PI and LQG controllers, and the open-loop system response.

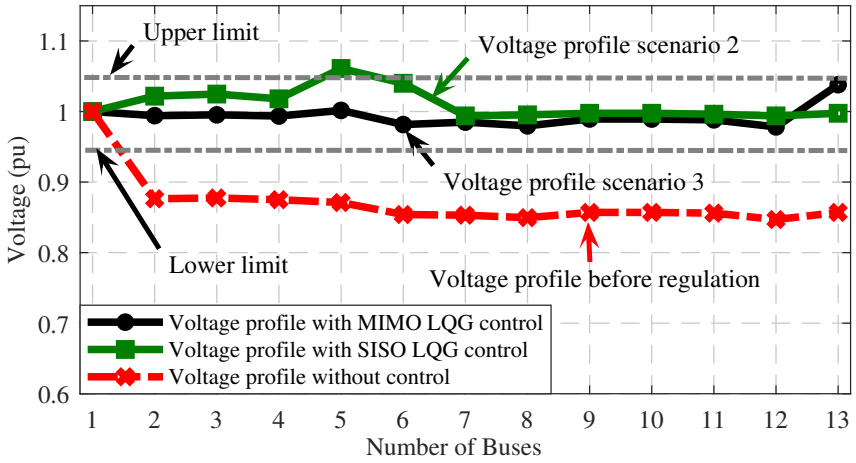

Figure 4.11: Voltage profile for *Scenarios 2* and *3* with respect to the open loop system response.

The voltage level dynamic response at all nodes along with the network, together with the reactive power injected by the parking lots are described in Fig. 4.17. Under nominal load conditions, the voltage level at all nodes is within the allowable standard limits [1]. When the 123-bus system is working in closed-loop and the inductive load at node 95 is increased up to 1.6MVar at $0.25s$, the hierarchical controller coordinates the reactive power injection at all parking lots to quickly improve the voltage profile, reaching the stable state in less than $100ms$, as displayed in Figs. 4.17(a)-(b). These results highlight the robustness of the system facing significant changes in the operating point, since the ER-based system identification process is driven regarding the nominal operation.

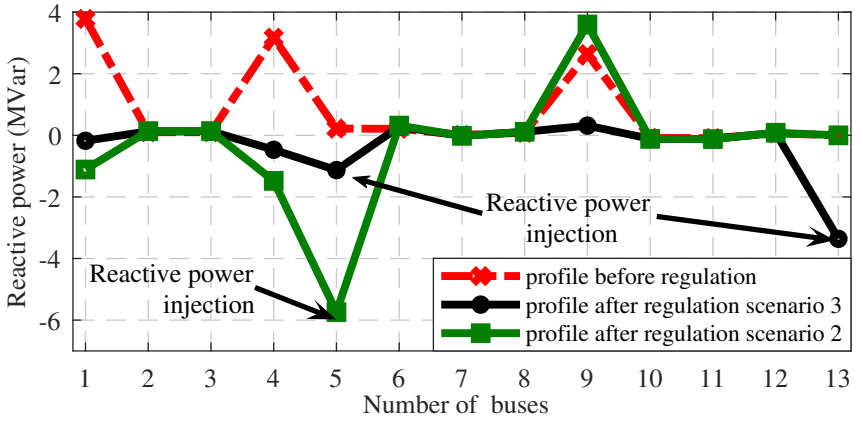

Figure 4.12: Reactive power behavior for *Scenarios 2* and *3* with respect to the open loop system response.

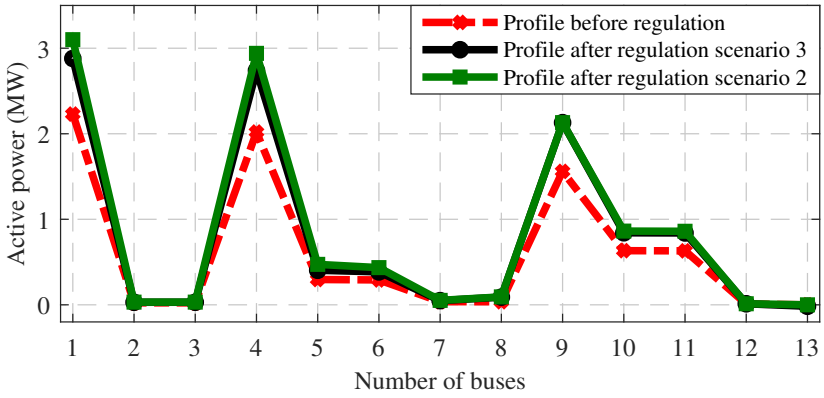

Figure 4.13: Active power profile for *Scenarios 2* and *3* with respect to the open loop system response.

Figure 4.18 exhibits the grid voltage dynamic response to the presence of a 3-cycle three-phase fault. At 0.25s, the fault event starts reducing the voltage level over the 123 nodes in the entire network. When the fault is present, the grid voltage remains below the allowed operating limits, and the controller reacts by increasing the reactive power injected into the grid up to its operating limit (1.8MVar) to mitigate the voltage level reduction, as depicted in Fig. 4.18(b). However, the magnitude of the fault prevents compensation from being effective. When the fault ends, the voltage level increases. Still, the controller outputs remain saturated at its maximum operating level causing a 10% increase in the voltage level for approximately 35ms, as shown in Fig 4.18(a). The closed-loop system remains stable under significant three-phase faults, evidencing the complete recovery of the system after

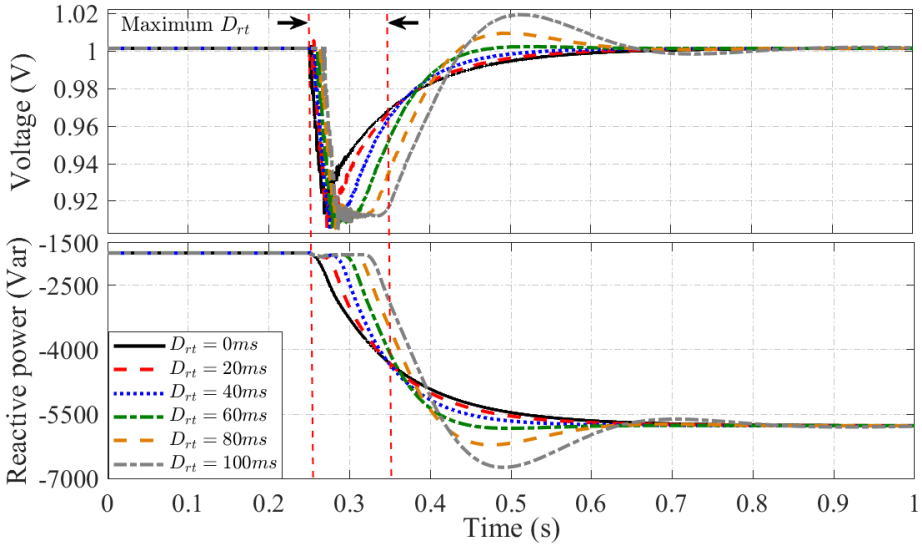

Figure 4.14: Dynamic response of the voltage level and reactive power in closed-loop at node 9 in *Scenario 3* as a function of round-trip delay or latency variation from $0ms$ to $100ms$.

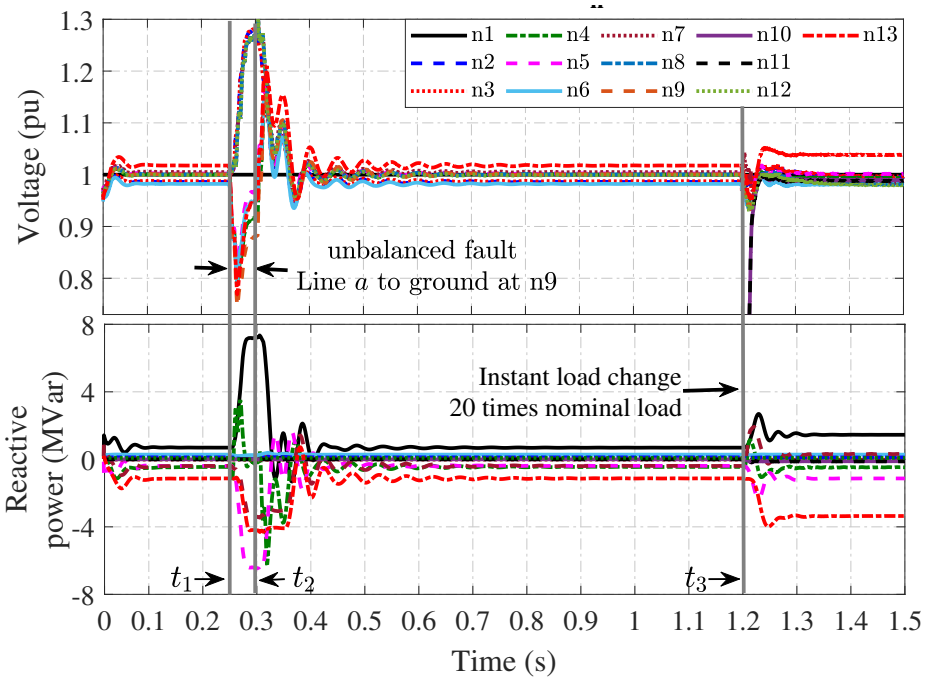

Figure 4.15: Dynamic response of the voltage level and reactive power in closed-loop in *Scenario 3* in the presence of an unbalanced fault in the line a with respect to ground at node 9 and severe change of the network load ($\times 20$).

failure and the robustness of the proposed controller.

The comparison between the traditional OLTC-based control scheme and the hierarchical controller proposed is observed in Figs. 4.19(a)-(d), evidencing the time response when the inductive load at node 95 is increased up to 1.6MVar. The OLTC is modeled with 8 discrete tap changes, with additional voltage per tap of 0.040pu, representing the transformer between nodes 67 and 160 in Fig. 4.16. In the requirements for tap changers in the IEEE Std. C57.131-2012 [75], it is reported that the total time for changing one tap position lasts from $1s$ to $10s$. In this way, the tap position discretely behaves varying the transformer ratio every $1.6s$ until reaching the voltage set point of 1 per unit, as can be seen in Figs. 4.19(a)-(b). Notice that if the load increases when the proposed hierarchical control system is deactivated and the OLTC makes the full control effort, then a reduction of the voltage magnitude is caused at the monitored node, at t = $3s$, and the OLTC attempts to improve the voltage profile every $1.6s$, completing its regulation $6s$ after the disturbance occurs, as detailed in Figs. 4.19(a)-(b). It is notorious that every tap change yields voltage undershoots of significant magnitude, as displayed in Fig. 4.19(b). In contrast, when the OLTC and the proposed hierarchical control system work together in Fig. 4.19(c)-(d), a precise voltage regulation is executed in less than 100ms. The response speed of the off-board EV chargers allows that the proposed control approach carries out the control effort in a fraction of the time that

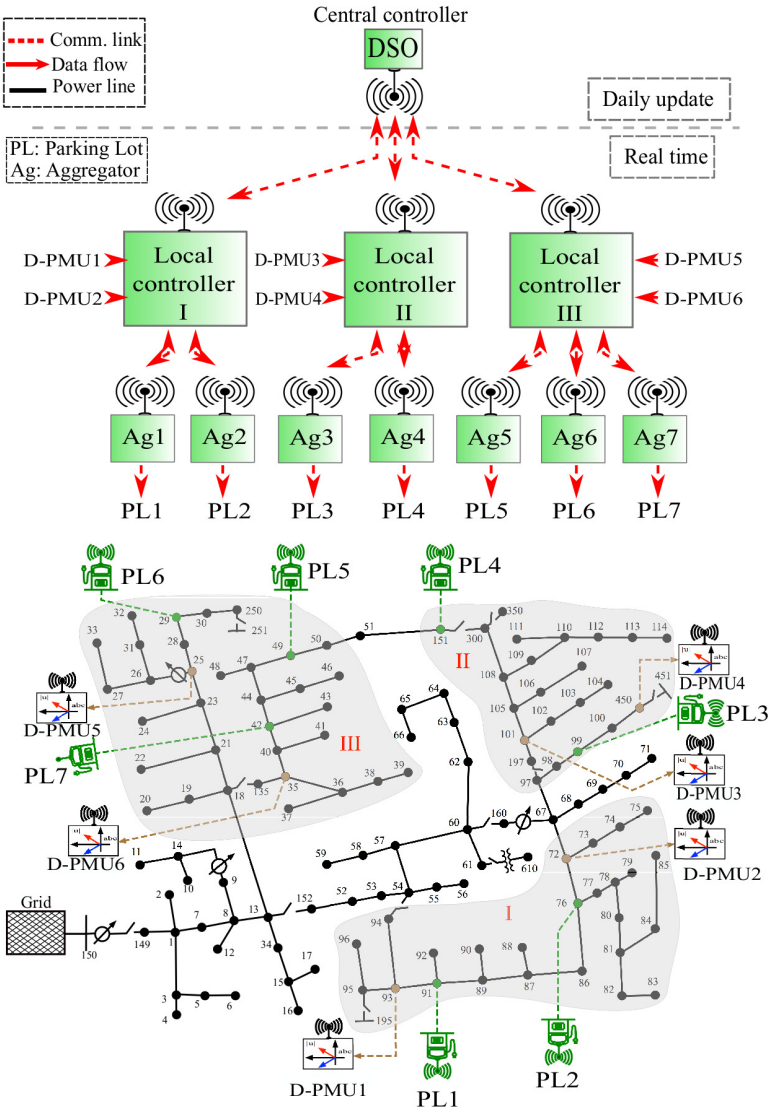

Figure 4.16: IEEE 123-node test feeder [4, 5] in Scenario 4.

the OLTC takes. Consequently, the D-PMUs and EV chargers-based VVC can effectively interact with traditional control methods such as OLTCs to improve the grid voltage profile, contributing to fast and accurate regulation.

4.4 Case 2: Decongestion of ADGs via Control of Reactive Power Injection

This section presents an application of the proposed hierarchical controller to increase

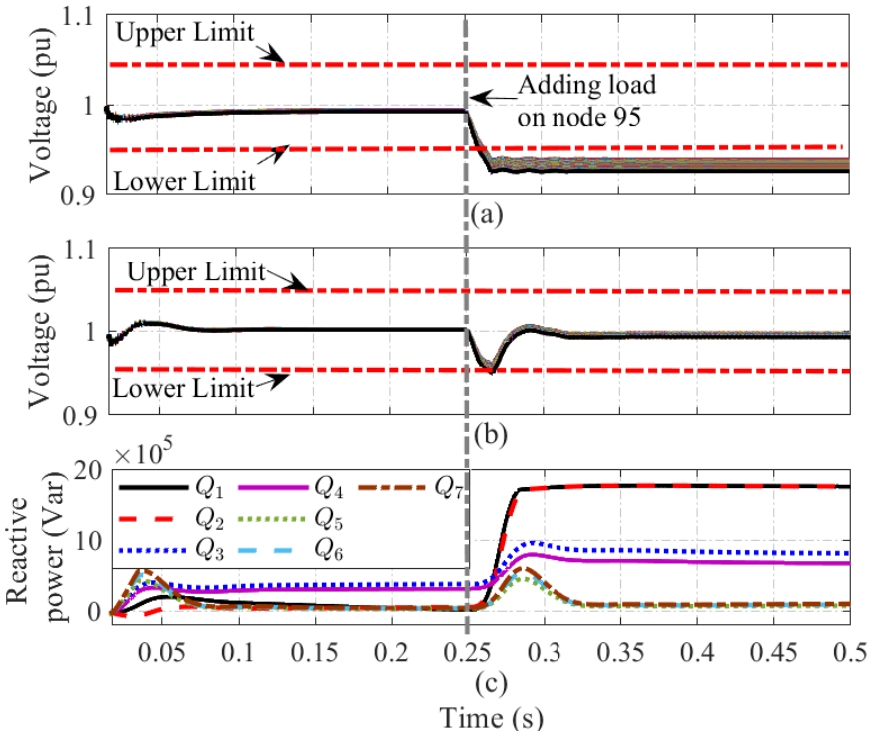

Figure 4.17: Dynamic voltage response in the 123-node distribution grid when the load is added at node 95. (a) In open-loop. (b) In closed-loop. (c) Reactive power injected by 7 parking lots (Scenario 4).

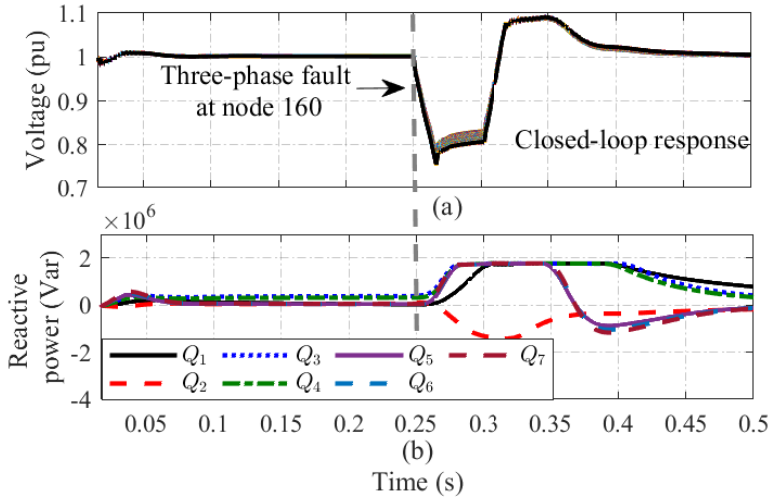

Figure 4.18: Dynamic voltage response in the 123-node network when a three-phase fault takes place at node 160. (a) In closed-loop. (b) Reactive power injected by 7 parking lots (Scenario 4).

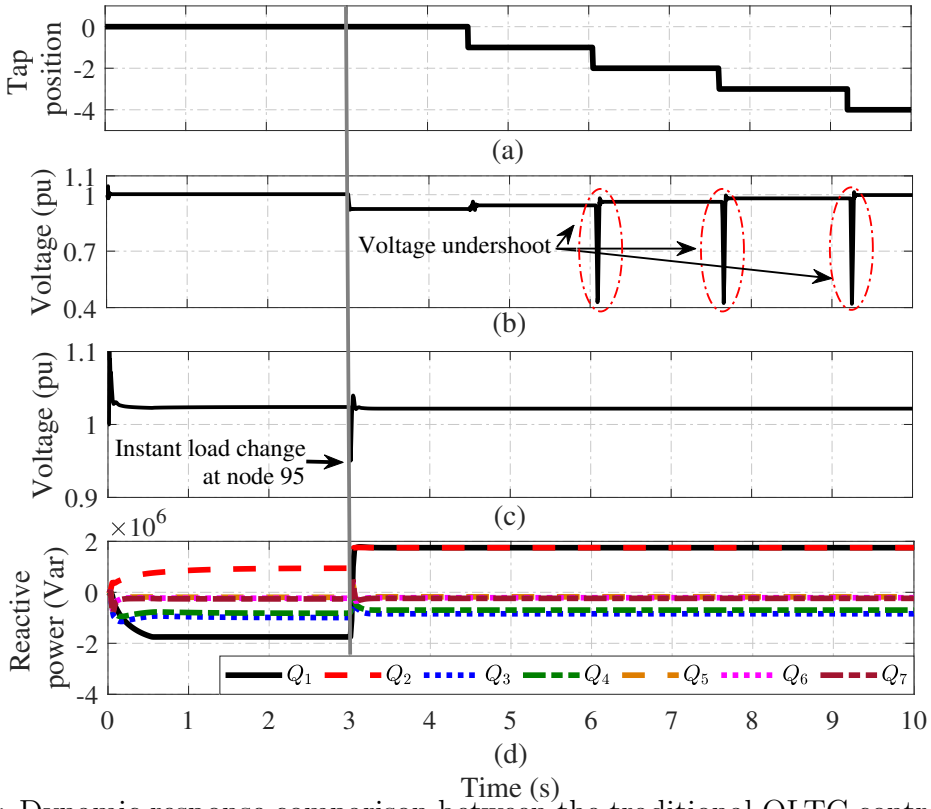

Figure 4.19: Dynamic response comparison between the traditional OLTC controller and the proposed controller in the 123-node distribution feeder at node 160. (a) Tap position. (b) Dynamic voltage response with the OLTC controller. (C) Dynamic voltage response with the OLTC and proposed controller. (d) Reactive power injected by 7 parking lots.

the operational flexibility of active distribution grids by exploiting the potential of electric vehicle chargers. EV chargers are flexible resources available in modern DGs with the ability to decongest and increase grid capacity by using a grid-side controller to coordinate reactive power injection. Therefore, this work demonstrates that an intelligent management of reactive power injection allows voltage regulation and increases operational flexibility of the grid. The feasibility of the proposal is demonstrated using simulated scenarios on the IEEE 13-node test feeder. The results presented in this manuscript section are based on the book chapter reported in [76].

The hardware of each EVs battery chargers, summarized in Fig 2.2. The topology and the controller were explained in section 4.1.

4.4.1 System description

The straightforward implementation for the coordinated hierarchical active power decongestion scheme that interfaces the DS in Fig. 4.20 is established through the block

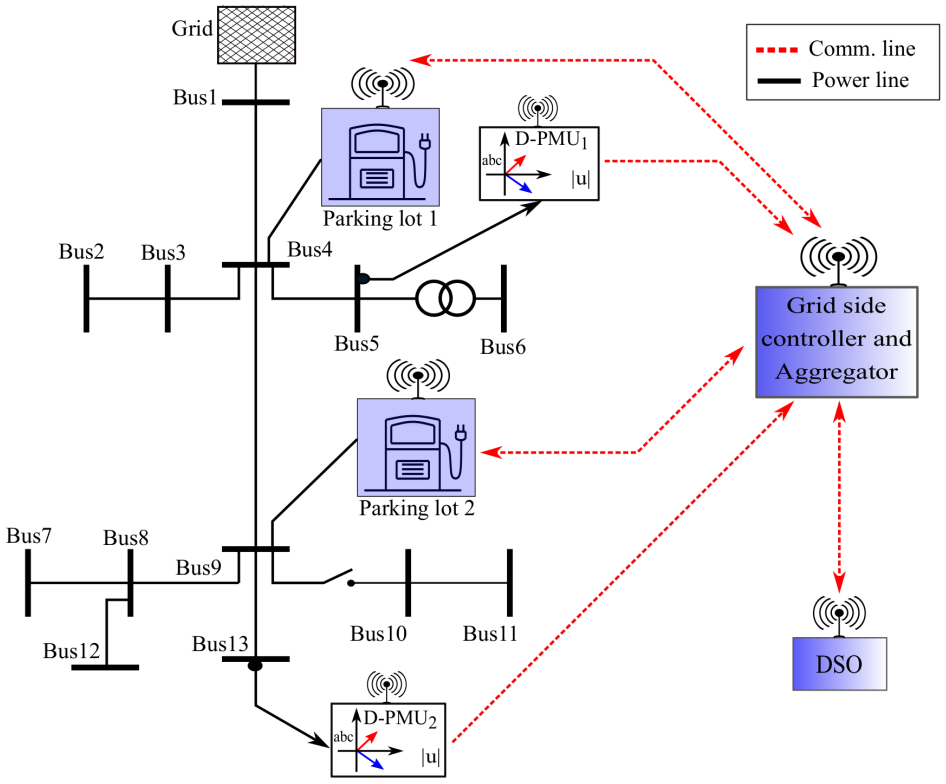

Figure 4.20: IEEE 13-nodes test feeder in *Scenarios 1-3* [3].

diagram in Fig. 4.3.

The IEEE 13-node test feeder depicted in Fig. 4.20 is used to demonstrate the feasibility and effectiveness of the proposed hierarchical control structure. The system is implemented in [3]. As stated by Section 4.1, every charger is equipped by a VSC and a DAB as displayed in Fig. 2.2, whose PI controllers are tuned by using the pole location method. Both VSC and DAB are implemented in accordance with the parameters in Table 4.3.

For the simulation analysis, four scenarios are managed. They include two D-PMUs and two parking lots. In these cases, the switch installed between bus 9 and bus 10 closes at 0.5s, adding the loads connected on buses 10 and 11 to the network. The parking lot 1 can inject up to 5.2MVA (upon request) based on the connection of 15 EV-chargers in shunt connection. Similarly, the parking lot 2 comprises 10 EV-chargers with the capacity to provide up to 3.5MVA (upon request). Each charger installed at the parking lots can supply 350kVA at $420V_{LL}$. The parameters for each charger are presented in Table 4.3. At the PCC, a step-up power transformer adapts the voltage levels from $420V_{LL}$ up to $4160V_{LL}$, between the parking lots and the network feeder.

4.4.2 Scenarios description

Scenario 1. In this case, both parking lots and both D-PMUs are used as actuators and sensors for the control system, respectively (Fig. 4.20). Simulation is performed with the MIMO LQG controller acting in closed-loop with the network in comparison with the system response in open-loop.

Scenario 2. A comparison of the performance between PI and SISO LQG controllers closing the control loop with respect to the system response in open-loop is devoted in this scenario. Parking lot 1 and D-PMU$_2$ represent the actuator and the sensor for the control system, respectively. Parking lot 2 and D-PMU$_1$ are not considered in this case (Fig. 4.20).

Scenario 3. This case includes both parking lots and both D-PMUs. The simulation is carried out with the MIMO LQG controller, and it is contrasted with the open-loop system response.

Scenario 4. In this case, the resistive load connected at node 9 is increased linearly. The simulation is performed with the open-loop controller and in closed-loop with the MIMO LQG controller.

In *Scenarios 2, 3*, and *4*, the load connected at bus 10 is increased 20 times to verify the efficiency of the proposed control system for regulating the network voltage in the presence of extreme load disturbances.

Table 4.3: Simulation parameters for each EV charger.

Parameter	***Value***
Nominal voltage and rated battery capacity	380V, 5.4x70Ah
DC link reference voltage (v_{dcref})	800V
DC link capacitor bank (C)	3600μF
DAB leakage inductance (L_t)	1.5 μH
DAB transformer ratio	400/800 V_{rms}
VSC inductance filter (L)	600 μH $X3$
Grid side transformer ratio	480/4160 V_{rms}
Simulation sample time	50μs

4.4.3 Results

The network voltage profile for the conditions in *Scenario 1* is presented in Fig. 4.21. When the system operates in open-loop, all buses except the source indicate lower voltage amplitudes than one suggested by the standard ANSI C84.1 [1], as exhibited by the dotted red line. When the closed-loop controller is enable, the voltage profile improves significantly, settling its amplitude within the limits established by the standard ANSI C84.1 [1]. In fact, the voltage amplitude almost attains 1pu at the smart measurement location (D-PMUs installed at nodes 5 and 13).

Figure 4.22 points out the reactive power profile for all buses in the network. The reactive power is injected at nodes 4 and 9, as depicted in Fig. 4.20, causing that the reactive power in those buses becomes greater than that of the other buses. Simultaneously, the controlled injection of reactive power increases the network capacity to distribute active power, improving the power factor, as indicated at buses 4 and 9 in Figs. 4.23 and 4.24, and implying active power decongestion.

The dynamic response comparison for the PI and the SISO LQG controllers concerning the DS open-loop response, with a significant change in load, is displayed in Fig. 4.25. At 0.5 s, the breaker is closed changing the operating conditions of the network by adding capacity. Without a controller, the system operates outside the reliability enforcing limits established in the ANSI C84.1 standard (below 0.95 pu) [1], as shown by the black dotted line measuring at bus 13. At full load, a voltage drop of 14% is noticed. In contrast, the closed-loop system responses, when the PI and LQG controllers are incorporated, illustrated by the red and blue lines, respectively. With both controllers, the system returns to the desired operating value (1 pu). Nonetheless, the LQG controller exhibits a faster response than the PI controller. The LQG controller takes 205 ms to reach the steady-state; in comparison, the PI controller takes 445 ms. Simultaneously, the controlled reactive power injection increases the capacity in the network to distribute active power, improving the power factor, as shown at buses 4

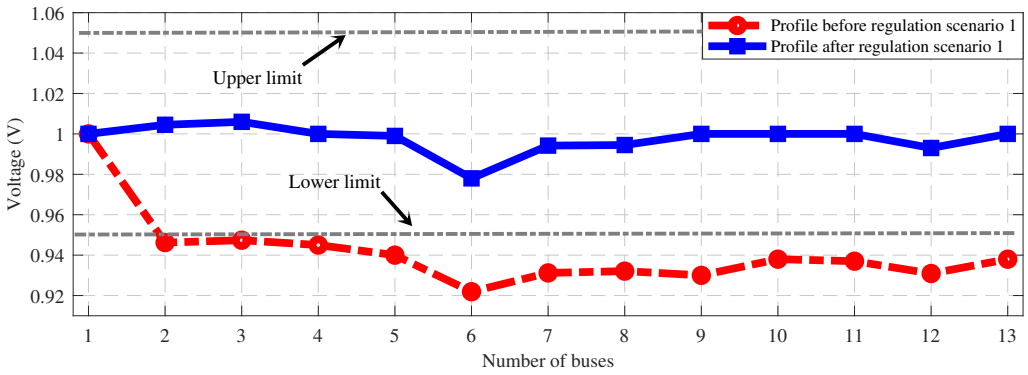

Figure 4.21: Voltage profile in *Scenario 1* for the closed-loop with MIMO LQG controller and open-loop system responses.

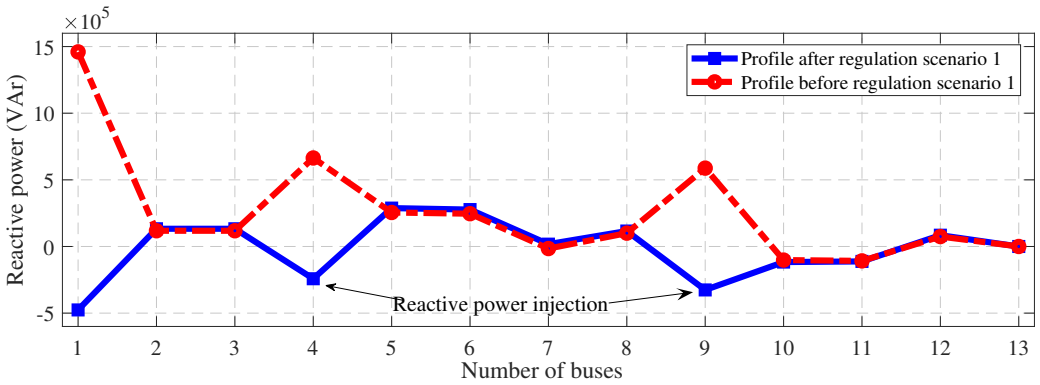

Figure 4.22: Reactive power profile before and after regulation in *Scenario 1*.

and 9 of Fig. 4.26.

The voltage and reactive power at all buses during the highest load condition are depicted in Figs. 4.27 and 4.28, respectively. Under open-loop system conditions (red dotted line), the voltage profile throughout the network is below the limits established by the ANSI C84.1 standard [1], exhibiting high levels of reactive power at bus 9. This is a consequence of the connected loads on the adjacent branches. Whereas, the voltage profile in *Scenarios 2* and *3*, when the system operates in closed-loop with LQG controllers, is ostensibly improved by injecting reactive power from both parking lots. However, the LQG controller in case 2 only injects reactive power into the node 4 supporting the voltage magnitude. The MIMO control strategy used in *Scenario 3* is more useful to improve the network voltage profile (about 1 pu), injecting reactive power at buses 4 and 9.

In *Scenario 4*, the power absorbed by the resistive load connected to bus 9 is linearly

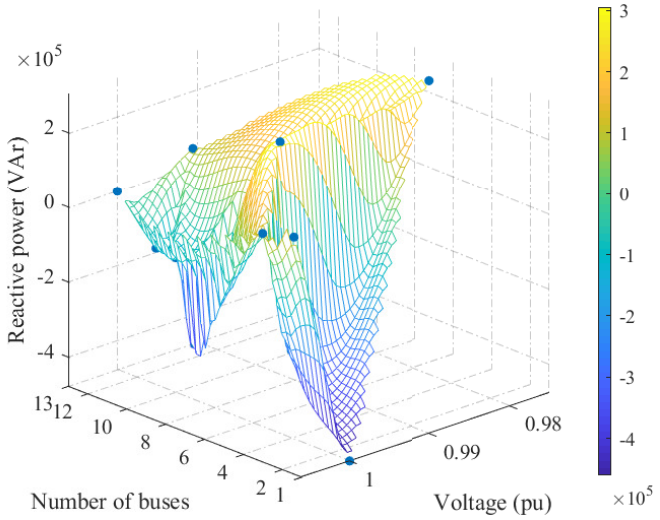

Figure 4.23: Reactive power impacts on the voltage profile in *Scenario 1*.

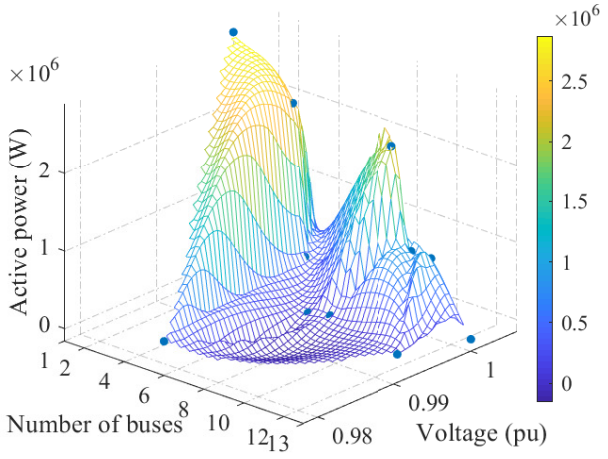

Figure 4.24: Active power decongestion in *Scenario 1*.

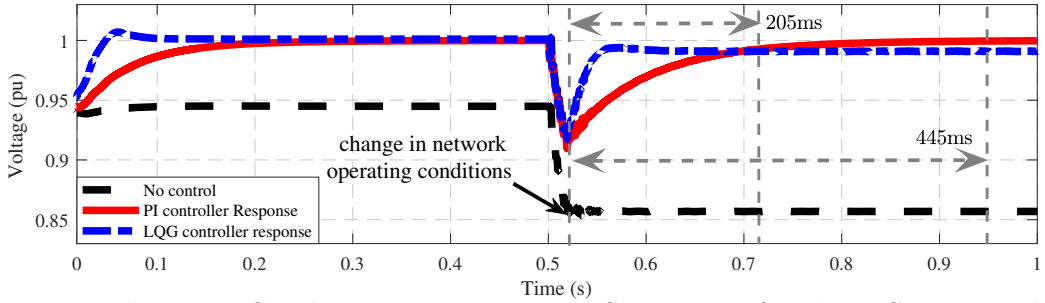

Figure 4.25: Voltage profile dynamic response in *Scenario 2* for the DS equipped with PI and LQG controllers, and the open-loop system response.

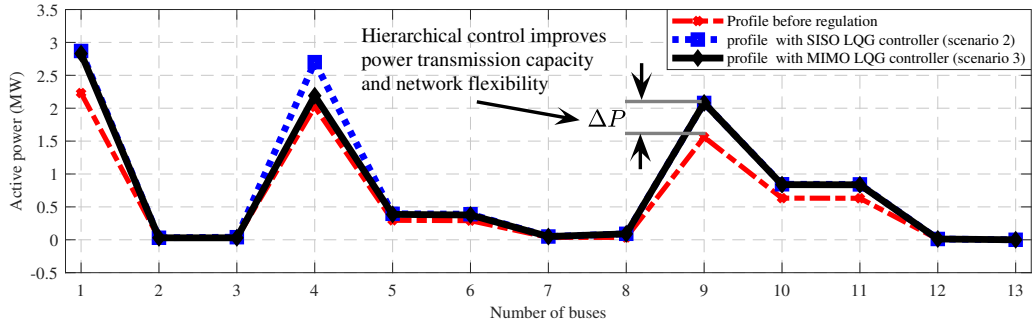

Figure 4.26: Active power profile for *Scenarios 2* and *3* with respect to the open loop system response.

increased from 1 kW to 7 MW to analyze grid flexibility via the network decongestion in open-loop and closed-loop with the MIMO LQG controller. Such variations along the transferred power between nodes 4 and 9, and the voltage level at node 9 with respect to the change in resistive load connected at node 9, are closely analyzed in Fig. 4.29. In the open-loop behavior, the voltage level is reduced to 0.51 pu, whereas the load increases up to 6 MW, affecting the voltage profile of the entire network. Meanwhile, in closed-loop, the

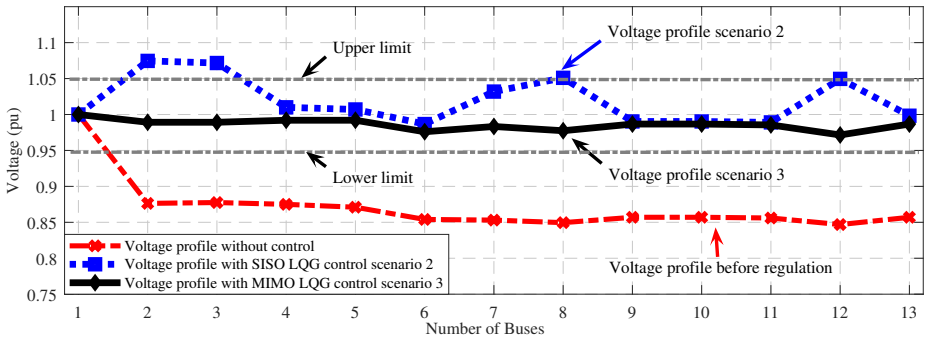

Figure 4.27: Voltage profile for *Scenarios 2* and *3* with respect to the open loop system response.

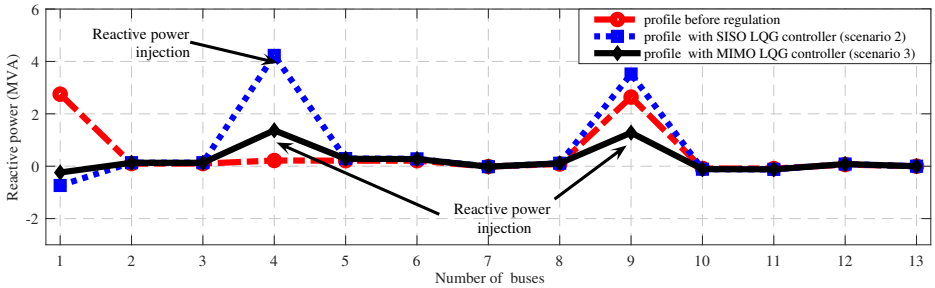

Figure 4.28: Reactive power behavior for *Scenarios 2* and *3* with respect to the open loop system response.

voltage level remains close to 1 pu and the active power transmission capacity is significantly increased, i.e., the active power transported by the line increases from 9.85 MW to 17.47 MW for the same load level, which in turn enables to quantitatively increasing the flexibility of the distribution grid.

Similar results are observed in the active power flowing between nodes 1 and 4, and the voltage at node 4 (Fig. 4.30). In the open-loop condition, the voltage level is reduced to 0.77 pu, when the load increases up to 5.5 MW. The closed-loop system does that the voltage behaves close to 1 pu. In this test, the capacity to transport active power increases from 10.3 MW to 16.5 MW, when the load increases up to 5.5 MW.

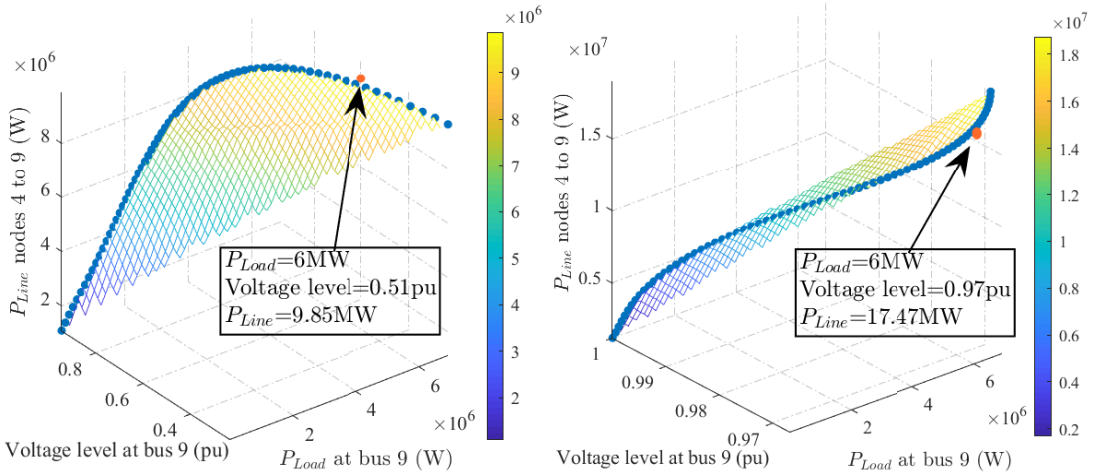

(a) Open-loop (b) Closed-loop

Figure 4.29: Bus 9 active power decongestion comparison in open-loop vs closed-loop *Scenario 4*.

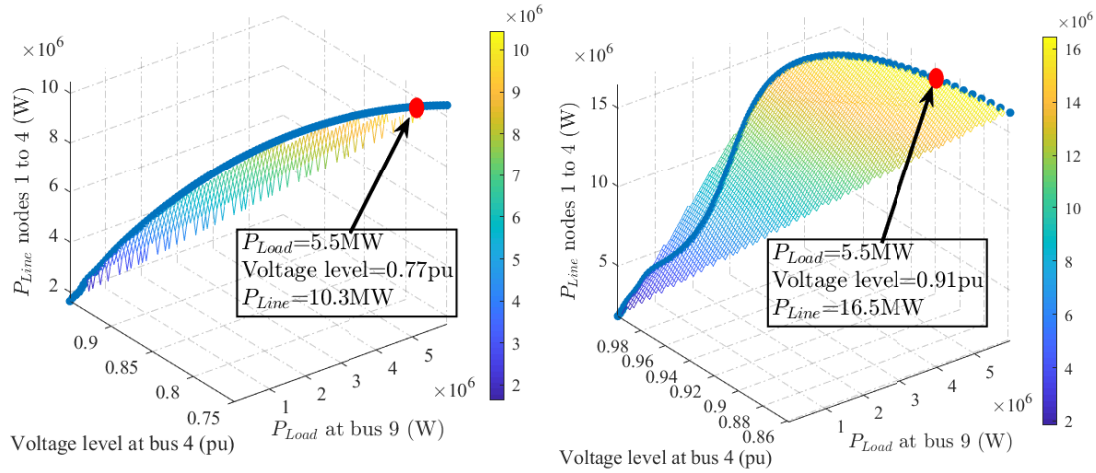

(a) Open-loop (b) Closed-loop

Figure 4.30: Bus 4 active power decongestion comparison open-loop vs closed-loop *Scenario 4*.

4.5 Summary

This chapter introduced the optimal hybrid control framework to improve the voltage profile and increase the operational flexibility of highly unbalanced distribution grids by the coordination of reactive power injection from multiple electric vehicle chargers. This scheme

exploits the advantages of time-synchronized measurements, centralized control and local controllers integrated in a hierarchical and scalable scheme, coordinated by the distribution system operator. The proposed control framework is powered by the system identification technique based on the ERA, a linear quadratic Gaussian controller, the distribution-level phasor measurement units, and a new aggregator agent that manages the power injection of electric vehicle chargers to accurately and timely regulate the dynamic voltage response in each subarea or the entire distribution grid. The robustness and feasibility of the proposal are demonstrated by employing simulated scenarios with unbalanced faults, communication latency, and highly unbalanced load conditions on the 13-node and 123-node IEEE test feeders, compensating for voltage variations accurately within 205 ms. The promising result of this study suggests a novel application for an emerging measurement-based control system in the operation of modern active distribution grids. This chapter is based on the results and theoretical concepts published in [8].

Chapter 5

Conclusions, contributions and Future Works

5.1 Conclusions

In this investigation a novel real-time optimal and hierarchical control framework is presented to provide voltage regulation in distribution networks or frequency/voltage support for transmission networks by exploiting the fast power injection of battery-based power systems. Simulation results demonstrated that the proposed controller is effective for frequency and voltage support on a millisecond scale, contributing to increase the stability of the power system.

Tests carried out under extreme conditions of unbalanced three-phase faults, significant load changes, noise and communication latency demonstrated the suitable dynamic performance of the proposed hierarchical control scheme to support the frequency and voltage of transmission grids. The results also illustrate the robustness and reliability of the proposed approach, even when controller tuning and system identification are performed at rated operating conditions.

The proposed controller is effective for frequency and voltage support in less than 450ms, even in the presence of a load increase of up to 125%. The dynamic performance and stability of the proposed hierarchical optimal controller is maintained despite events such as three-phase faults and significant load changes take place. The results also reveal that the proposed control structure prioritizes power injection from the BESSs installed in the area where the contingency takes place, mitigating power imbalances locally with minimal disturbance to the dynamics of the rest of the power grid.

The proposed Volt/Var control framework for the operation in distribution systems

coordinates the reactive power injection from the EV-chargers grouped in parking lots to improve the voltage profile and provide ancillary services to the distribution networks. In this conditions, the proposed technique contributes to voltage support of DGs, even in the presence of significant disturbances of up to 14%, recovering the voltage profile in less than 205ms, and protecting sensitive equipment connected to the DG. The results show that the suitable reactive power injection from EV chargers allows the active power transport capacity to be expanded, making the grid more flexible.

5.2 Contributions

The most significant contributions of this dissertation are summarized below:

i. A novel real-time, optimal and hierarchical control framework to provide voltage regulation in distribution networks and frequency/voltage support in transmission networks with very fast response time (milliseconds) is proposed in this work. This control approach can smartly cluster the battery systems geographically close, working in a symbiotic cooperation with the power system operator to establish the optimal control action in a multiple-input multiple-output structure. This approach can be extended to networks of many areas under highly unbalanced loads, communication latency, noise in measurement signals and unbalanced faults.

ii. This work develops a new aggregator agent that incorporates logical rules in the hierarchical controller for the formulation of the active and reactive power commands for the battery systems according to the operating constraints, the individual injection capacity of every battery system and the estimated optimal control action. The scheme reduces the utilization of the battery systems and locally mitigates the imbalances between supply and demand in the area where the contingency takes place, reducing disturbances to the neighboring areas. At the same time, the proposed logical architecture reduces the latency and computational burden of the conventional central controller.

iii. This proposal introduce the eigensystem realization system to identify the power distribution networks with a high penetration of electronic power converters, by exploiting the smart measurements acquired from D-PMUs and extending its applicability by automatically executing the model identification routines with the regularity programmed by the power system operator with small system disturbances.

5.3 Publications

Products emanating from this research conducted during my doctoral studies and reported in this dissertation include **3** publications in refereed journals, **1** book chapter, and **2** publications in peer-reviewed conferences.

5.3.1 Publications in Refereed Journals

J1. Gabriel E. Mejia-Ruiz, R. Cardenas-Javier, M. R. Arrieta Paternina, J. R. Rodriguez-Rodriguez, J. M. Ramirez and A. Zamora-Mendez, "Coordinated Optimal Volt/Var Control for Distribution Networks via D-PMUs and EV Chargers by Exploiting the Eigensystem Realization," in IEEE Transactions on Smart Grid, vol. 12, no. 3, pp. 2425-2438, May 2021, doi: 10.1109/TSG.2021.3050443, IF=8.26.

J2. Gabriel E. Mejia-Ruiz, Mario R. Arrieta Paternina, Felix Rafael Segundo Sevilla, Petr Korba, "Fast Hierarchical Coordinated Controller for Distributed Battery Energy Storage Systems to Mitigate Voltage and Frequency Deviations", Applied Energy, Jul 2022, IF= 11.45.

J3. Gabriel E. Mejia-Ruiz, Mario R. Arrieta Paternina, Felix Rafael Segundo Sevilla, Petr Korba, "Real-Time Co-simulation of a Transmission-Distribution Network Integrated with Distributed Energy Resources and a Frequency-Voltage Optimal Controller", Applied Energy, Submitted Sep 2022, IF= 11.45.

5.3.2 Book Chapters

Ch1. Gabriel E. Mejia-Ruiz, et al. Flexibility in Electric Power Distribution Networks. Chapter: Decongestion of Active Distribution Grids via D-PMUs-based Reactive Power Control and Electric Vehicle Chargers. Taylor and Francis. ISBN 9780367641412-July 16, 2021. https://doi.org/10.1201/9781003122326.

5.3.3 Publications in Refereed Conferences

C1. Gabriel E. Mejia-Ruiz, et al., A. Paternina, J. R. Rodriguez, A. Zamora, G. Bolivar-Ortiz and C. Toledo-Santos, "A Bidirectional Isolated Charger for Electric Vehicles in V2G Systems with the Capacity to Provide Ancillary Services," 2020 52nd North American Power Symposium (NAPS), 2021, pp. 1-6, doi: 10.1109/NAPS50074.2021.9449674, Arizona, USA.

C2. Gabriel. E. Mejia-Ruiz, R. Cardenas, M. R. A. Paternina, A. Zamora and C. Toledo-Santos, "Phasor-Based Optimal Voltage Control for Distribution Grids Through D-

PMUs and EV Battery Charger," 2021 North American Power Symposium (NAPS), 2021, pp. 1-6, doi: 10.1109/NAPS52732.2021.9654753.

5.4 Future Works

The implementation of the proposed control strategy in a real-time simulation environment with power-hardware-in-the-loop methodologies, emulating battery-based systems or distributed energy resources, makes up a key future work. These simulations will be able to study the system response when the grid has a high penetration of renewable sources. Test scenarios in this environment will demonstrate the real effects of communication noise and latency on controller performance and grid code compliance.

Future works also include the addition of new logical rules for the operation of battery-based systems, considering financial aspects or market rules. For example, in addition to minimizing the error and energy used by the actuators to provide frequency and voltage support, the hierarchical control scheme could also maximize the operational economic profit by incorporating cost-optimization functions and logic rules that consider the financial aspects of the operation.

Since this research dealt with battery-based systems and their electronic converters as actuators in the control loops, then further studies will explore the feasibility in taking advantage of the reactive power remaining injection capacity of other voltage source converter-based distributed energy sources, such as wind or solar generation sources. All these power injection sources coordinated in a hierarchical scheme.

References

[1] N. E. M. Association et al., "American national standards institute (ansi) c84.1, voltage ratings for electric power systems and equipment," Rosslyn, VA, 2016.

[2] Kundur, Power System Stability And Control, ser. EPRI power system engineering series. McGraw-Hill, 1994.

[3] I. Sharma, C. Cañizares, and K. Bhattacharya, "Smart charging of pevs penetrating into residential distribution systems," IEEE Trans. Smart Grid, vol. 5, no. 3, pp. 1196–1209, 2014.

[4] Graham Dudgeon. Ieee 123 node test feeder in simscape power systems. MATLAB Central File Exchange. Retrieved October 19, 2020. [Online]. Available: https://www.mathworks.com/matlabcentral/fileexchange/66599-ieee-123-node-test-feeder-in-simscape-power-systems

[5] K. P. Schneider, B. A. Mather, B. C. Pal, C. . Ten, G. J. Shirek, H. Zhu, J. C. Fuller, J. L. R. Pereira, L. F. Ochoa, L. R. de Araujo, R. C. Dugan, S. Matthias, S. Paudyal, T. E. McDermott, and W. Kersting, "Analytic considerations and design basis for the ieee distribution test feeders," IEEE Transactions on Power Systems, vol. 33, no. 3, pp. 3181–3188, 2018.

[6] Z. Yuan, A. Zecchino, R. Cherkaoui, and M. Paolone, "Real-time control of battery energy storage systems to provide ancillary services considering voltage-dependent capability of dc-ac converters," IEEE Transactions on Smart Grid, vol. 12, no. 5, pp. 4164–4175, 2021.

[7] O. J. Guerra, D. A. Tejada, and G. V. Reklaitis, "Climate change impacts and adaptation strategies for a hydro-dominated power system via stochastic optimization," Applied Energy, vol. 233-234, pp. 584–598, 2019.

[8] G. E. Mejia-Ruiz, R. Cardenas-Javier, M. R. Arrieta Paternina, J. R. Rodriguez-Rodriguez, J. M. Ramirez, and A. Zamora-Mendez, "Coordinated optimal volt/var control for distribution networks via d-pmus and ev chargers by exploiting the eigensystem realization," IEEE Transactions on Smart Grid, vol. 12, no. 3, pp. 2425–2438, 2021.

[9] E. Ekomwenrenren, Z. Tang, J. W. Simpson-Porco, E. Farantatos, M. Patel, and H. Hooshyar, "Hierarchical coordinated fast frequency control using inverter-based resources," IEEE Transactions on Power Systems, vol. 36, no. 6, pp. 4992–5005, 2021.

[10] S.-J. Lee, J.-H. Kim, C.-H. Kim, S.-K. Kim, E.-S. Kim, D.-U. Kim, K. K. Mehmood, and S. U. Khan, "Coordinated control algorithm for distributed battery energy storage systems for mitigating voltage and frequency deviations," IEEE Transactions on Smart Grid, vol. 7, no. 3, pp. 1713–1722, 2016.

REFERENCES

[11] S. Wogrin, D. Tejada-Arango, S. Delikaraoglou, and A. Botterud, "Assessing the impact of inertia and reactive power constraints in generation expansion planning," Applied Energy, vol. 280, p. 115925, 2020.

[12] V. A. Evangelopoulos, P. S. Georgilakis, and N. D. Hatziargyriou, "Optimal operation of smart distribution networks: A review of models, methods and future research," Electric Power Systems Research, vol. 140, pp. 95 – 106, 2016. [Online]. Available: http://www.sciencedirect.com/science/article/pii/S0378779616302437

[13] Y. Wang, K. T. Tan, X. Y. Peng, and P. L. So, "Coordinated control of distributed energy-storage systems for voltage regulation in distribution networks," IEEE Trans. Power Delivery, vol. 31, no. 3, pp. 1132–1141, 2016.

[14] F. Calero, C. A. Cañizares, and K. Bhattacharya, "Dynamic modeling of battery energy storage and applications in transmission systems," IEEE Transactions on Smart Grid, vol. 12, no. 1, pp. 589–598, 2021.

[15] U. Datta, A. Kalam, and J. Shi, "Battery energy storage system to stabilize transient voltage and frequency and enhance power export capability," IEEE Transactions on Power Systems, vol. 34, no. 3, pp. 1845–1857, 2019.

[16] IEEE, "Technical report: Dynamic models for turbine-governors in power system studies," IEEE Power & Energy Society, pp. 1 –117, 2013.

[17] S. Wang, Z. Y. Dong, C. Chen, H. Fan, and F. Luo, "Expansion planning of active distribution networks with multiple distributed energy resources and ev sharing system," IEEE Transactions on Smart Grid, vol. 11, no. 1, pp. 602–611, 2020.

[18] F. Calero, C. A. Cañizares, and K. Bhattacharya, "Aggregated bess dynamic models for active distribution network studies," IEEE Transactions on Smart Grid, vol. 12, no. 3, pp. 2077–2088, 2021.

[19] M. Kesler, M. C. Kisacikoglu, and L. M. Tolbert, "Vehicle-to-grid reactive power operation using plug-in electric vehicle bidirectional offboard charger," IEEE Trans. Industrial Electronics, vol. 61, no. 12, pp. 6778–6784, 2014.

[20] U. Datta, A. Kalam, and J. Shi, "Battery energy storage system control for mitigating pv penetration impact on primary frequency control and state-of-charge recovery," IEEE Transactions on Sustainable Energy, vol. 11, no. 2, pp. 746–757, 2020.

[21] V. Rallabandi, O. M. Akeyo, N. Jewell, and D. M. Ionel, "Incorporating battery energy storage systems into multi-mw grid connected pv systems," IEEE Transactions on Industry Applications, vol. 55, no. 1, pp. 638–647, 2019.

[22] W. Wang, X. Fang, H. Cui, F. Li, Y. Liu, and T. J. Overbye, "Transmission-and-distribution dynamic co-simulation framework for distributed energy resource frequency response," IEEE Transactions on Smart Grid, pp. 1–1, 2021.

[23] Z. Wu, D. W. Gao, H. Zhang, S. Yan, and X. Wang, "Coordinated control strategy of battery energy storage system and pmsg-wtg to enhance system frequency regulation capability," IEEE Transactions on Sustainable Energy, vol. 8, no. 3, pp. 1330–1343, 2017.

[24] L. Shang, X. Dong, C. Liu, and Z. Gong, "Fast grid frequency and voltage control of battery energy storage system based on the amplitude-phase-locked-loop," IEEE Transactions on Smart Grid, vol. 13, no. 2, pp. 941–953, 2022.

[25] R. Chakraborty, A. Chakrabortty, E. Farantatos, M. Patel, H. Hooshyar, and A. Darvishi, "Hierarchical frequency and voltage control using prioritized utilization of inverter based resources," 2021. [Online]. Available: https://arxiv.org/abs/2109.03446

[26] M. Ghazavi Dozein, O. Gomis-Bellmunt, and P. Mancarella, "Simultaneous provision of dynamic active and reactive power response from utility-scale battery energy storage systems in weak grids," IEEE Transactions on Power Systems, vol. 36, no. 6, pp. 5548–5557, 2021.

[27] Y. Zuo, Z. Yuan, F. Sossan, A. Zecchino, R. Cherkaoui, and M. Paolone, "Performance assessment of grid-forming and grid-following converter-interfaced battery energy storage systems on frequency regulation in low-inertia power grids," Sustainable Energy, Grids and Networks, vol. 27, p. 100496, 2021. [Online]. Available: https://www.sciencedirect.com/science/article/pii/S2352467721000679

[28] J. Tan and Y. Zhang, "Coordinated control strategy of a battery energy storage system to support a wind power plant providing multi-timescale frequency ancillary services," IEEE Transactions on Sustainable Energy, vol. 8, no. 3, pp. 1140–1153, 2017.

[29] J. D. Boles, Y. Ma, J. Wang, D. Osipov, L. M. Tolbert, and F. Wang, "Converter-based emulation of battery energy storage systems (bess) for grid applications," IEEE Transactions on Industry Applications, vol. 55, no. 4, pp. 4020–4032, 2019.

[30] V. Calderaro, V. Galdi, F. Lamberti, and A. Piccolo, "A smart strategy for voltage control ancillary service in distribution networks," IEEE Trans. Power Systems, vol. 30, no. 1, pp. 494–502, 2015.

[31] G. Buja, M. Bertoluzzo, and C. Fontana, "Reactive power compensation capabilities of v2g-enabled electric vehicles," IEEE Trans. Power Electron., vol. 32, no. 12, pp. 9447–9459, 2017.

[32] X. Chen, K. Leung, A. Y. S. Lam, and D. J. Hill, "Online scheduling for hierarchical vehicle-to-grid system: Design, formulation, and algorithm," IEEE Trans. Veh. Techn., vol. 68, no. 2, pp. 1302–1317, 2019.

[33] A. Kulmala and S. Repo, "Coordinated voltage control in distribution networks including several distributed energy resources," IEEE Trans. Smart Grid, vol. 5, no. 4, pp. 2010–2020, 2014.

[34] V. B. Pamshetti, S. Singh, and S. P. Singh, "Combined impact of network reconfiguration and volt-var control devices on energy savings in the presence of distributed generation," IEEE Systems Journal, vol. 14, no. 1, pp. 995–1006, 2020.

[35] D. Barros, W. L. A. Neves, and K. M. Dantas, "Controlled switching of series compensated transmission lines: Challenges and solutions," IEEE Trans. Power Delivery, vol. 35, no. 1, pp. 47–57, 2020.

[36] J. Wang, G. R. Bharati, S. Paudyal, O. Ceylan, B. P. Bhattarai, and K. S. Myers, "Coordinated electric vehicle charging with reactive power support to distribution grids," IEEE Trans. Ind. Inform., vol. 15, no. 1, pp. 54–63, 2019.

[37] S. C. Dhulipala, R. V. A. Monteiro, and R. F. d. Silva Teixeira, "Distributed model-predictive control strategy for distribution network volt/var control: A smart-building-based approach," IEEE Transactions on Industry Applications, vol. 55, no. 6, pp. 7041–7051, 2019.

[38] S. Amamra and J. Marco, "Vehicle-to-grid aggregator to support power grid and reduce electric vehicle charging cost," IEEE Access, vol. 7, pp. 178 528–178 538, 2019.

[39] G. Cavraro and R. Carli, "Local and distributed voltage control algorithms in distribution networks," IEEE Trans. Power Systems, vol. 33, no. 2, pp. 1420–1430, 2018.

[40] M. Restrepo, C. A. Cañizares, and M. Kazerani, "Three-stage distribution feeder control considering four-quadrant ev chargers," IEEE Trans. Smart Grid, vol. 9, no. 4, pp. 3736–3747, 2018.

[41] I. Kamwa, "A minimal realization approach to reduced-order modeling and modal analysis for power sytems response signals," IEEE Trans. Power Syst., vol. 8, no. 3, pp. 1020–1029, 1993.

REFERENCES

[42] J. Dobrowolski, F. Segundo, M. Paternina et al., "Inter-area oscillation control based on eigensystem realization approach," in IEEE ROPEC. IEEE, 2018, pp. 1–6.

[43] Y. Liu, L. Wu, and J. Li, "D-pmu based applications for emerging active distribution systems: A review," Electric Power Systems Research, vol. 179, p. 106063, 2020.

[44] J. Machowski, J. Bialek, J. Bumby, and J. Bumby, Power System Dynamics and Stability. Wiley, 1997.

[45] P. Sauer, M. Pai, and J. Chow, Power System Dynamics and Stability: With Synchrophasor Measurement and Power System Toolbox, ser. IEEE Press. Wiley, 2017.

[46] G. Wang, G. Konstantinou, C. D. Townsend, J. Pou, S. Vazquez, G. D. Demetriades, and V. G. Agelidis, "A review of power electronics for grid connection of utility-scale battery energy storage systems," IEEE Transactions on Sustainable Energy, vol. 7, no. 4, pp. 1778–1790, 2016.

[47] M. Stecca, L. R. Elizondo, T. B. Soeiro, P. Bauer, and P. Palensky, "A comprehensive review of the integration of battery energy storage systems into distribution networks," IEEE Open Journal of the Industrial Electronics Society, vol. 1, pp. 46–65, 2020.

[48] G. E. Mejia-Ruiz, N. Muñoz, and J. B. Cano, "Modeling, analysis and design procedure of lcl filter for grid connected converters," in 2015 IEEE Workshop on Power Electronics and Power Quality Applications (PEPQA), 2015, pp. 1–6.

[49] G. E. Mejia-Ruiz, M. R. Arrieta-Paternina, P. Korba, and F. R. Segundo Sevilla, "Fast hierarchical coordinated controller for distributed battery energy storage systems to mitigate voltage and frequency deviations," "Applied Energy", p. 26, 2022.

[50] M. Tariq, A. I. Maswood, C. J. Gajanayake, and A. K. Gupta, "Modeling and integration of a lithium-ion battery energy storage system with the more electric aircraft 270 v dc power distribution architecture," IEEE Access, vol. 6, pp. 41 785–41 802, 2018.

[51] H. Qin and J. W. Kimball, "Generalized average modeling of dual active bridge dc-dc converter," IEEE Trans. on Power Electron., vol. 27, no. 4, pp. 2078–2084, 2012.

[52] G. E. Mejia-Ruiz, J. R. Rodriguez, M. R. A. Paternina, N. Munoz-Galeano, and A. Zamora, "Grid-connected three-phase inverter system with lcl filter: Model, control and experimental results," in IEEE ISGT Latin America, 2019, pp. 1–6.

[53] J. Bay, Fundamentals of Linear State Space Systems, ser. Electrical Engineering Series. WCB/McGraw-Hill, 1999.

[54] F. Wilches-Bernal, R. H. Byrne, and J. Lian, "Damping of inter-area oscillations via modulation of aggregated loads," IEEE Trans. Power Systems, vol. 35, no. 3, pp. 2024–2036, 2019.

[55] M. R. Arrieta-Paternina, C. Franco, A. Zamora-Mendez, G. E. Mejia-Ruiz, F. Zelaya, R. E. Correa, P. Korba, and F. R. Segundo Sevilla, "Enhancing wide-area damping controllers via data-assisted power system linear models," "SSRN", p. 20, 2022.

[56] T. Duriez, S. L. Brunton, and B. R. Noack, Machine learning control-taming nonlinear dynamics and turbulence. Springer, 2017.

[57] Khamies, "Optimal model predictive and linear quadratic gaussian control for frequency stability of power systems considering wind energy," IEEE Access, vol. 9, pp. 116 453–116 474, 2021.

[58] D.-I. Stroe, V. Knap, M. Swierczynski, A.-I. Stroe, and R. Teodorescu, "Operation of a grid-connected lithium-ion battery energy storage system for primary frequency regulation: A battery lifetime perspective," IEEE Transactions on Industry Applications, vol. 53, no. 1, pp. 430–438, 2017.

REFERENCES

[59] Department of Energy. Global energy storage database. Department of Energy, USA. Retrieved November 5, 2021. [Online]. Available: https://sandia.gov/ess-ssl/gesdb/public/projects.html

[60] S. Chai, N. Z. Xu, M. Niu, K. W. Chan, C. Y. Chung, H. Jiang, and Y. Sun, "An evaluation framework for second-life ev/phev battery application in power systems," IEEE Access, vol. 9, pp. 152 430–152 441, 2021.

[61] E. Hossain, D. Murtaugh, J. Mody, H. M. R. Faruque, M. S. Haque Sunny, and N. Mohammad, "A comprehensive review on second-life batteries: Current state, manufacturing considerations, applications, impacts, barriers and potential solutions, business strategies, and policies," IEEE Access, vol. 7, pp. 73 215–73 252, 2019.

[62] D. Strickland, L. Chittock, D. A. Stone, M. P. Foster, and B. Price, "Estimation of transportation battery second life for use in electricity grid systems," IEEE Transactions on Sustainable Energy, vol. 5, no. 3, pp. 795–803, 2014.

[63] A. Eggli, S. Karagiannopoulos, S. Bolognami, and G. Hug, "Stability analysis and design of local control schemes in active distribution grids," IEEE Trans. Power Systems, vol. 11, no. 4, pp. 1–10, 2020.

[64] K. E. Antoniadou-Plytaria, I. N. Kouveliotis-Lysikatos, P. S. Georgilakis, and N. D. Hatziargyriou, "Distributed and decentralized voltage control of smart distribution networks: Models, methods, and future research," IEEE Transactions on Smart Grid, vol. 8, no. 6, pp. 2999–3008, 2017.

[65] M. Badoni, A. Singh, B. Singh, and H. Saxena, "Real-time implementation of active shunt compensator with adaptive srlmmn control technique for power quality improvement in the distribution system," IET Generation, Transmission Distribution, vol. 14, no. 8, pp. 1598–1606, 2020.

[66] N. Duan and E. M. Stewart, "Frequency event categorization in power distribution systems using micro pmu measurements," IEEE Trans. Smart Grid, vol. 11, no. 4, pp. 3043–3053, 2020.

[67] H. H. MÃ¼ller, "Allocation of pmu channels at substations for topology processing and state estimation," IET Generation, Transmission Distribution, vol. 14, no. 11, pp. 2034–2045, 2020.

[68] M. Saleh, Y. Esa, and A. Mohamed, "Impact of communication latency on the bus voltage of centrally controlled dc microgrids during islanding," IEEE Transactions on Sustainable Energy, vol. 10, no. 4, pp. 1844–1856, 2019.

[69] J. L. Gutierrez-Rivas, J. Lopez-Jimenez, E. Ros, and J. Diaz, "White rabbit hsr: A seamless subnanosecond redundant timing system with low-latency data capabilities for the smart grid," IEEE Transactions on Industrial Informatics, vol. 14, no. 8, pp. 3486–3494, 2018.

[70] Y. Du, H. Tu, H. Yu, and S. Lukic, "Accurate consensus-based distributed averaging with variable time delay in support of distributed secondary control algorithms," IEEE Transactions on Smart Grid, vol. 11, no. 4, pp. 2918–2928, 2020.

[71] M. Shahraeini, M. H. Javidi, and M. S. Ghazizadeh, "Comparison between communication infrastructures of centralized and decentralized wide area measurement systems," IEEE Transactions on Smart Grid, vol. 2, no. 1, pp. 206–211, 2011.

[72] The MathWorks,Inc. Ieee 13 node test feeder. MATLAB. Retrieved October 26, 2020. [Online]. Available: https://la.mathworks.com/help/physmod/sps/ug/ieee-13-node-test-feeder.html

[73] Tesla Manufacture. Transphorm: Gallium nitride (gan) power devices. [Online]. Available: https://www.tesla.com/supercharger

[74] ABB Manufacture. High power charging infrastructure. [Online]. Available: https://new.abb.com/ev-charging/products/car-charging/high-power-charging

[75] IEEE, "Ieee standard requirements for tap changers," IEEE Std C57.131-2012 (Revision of IEEE Std C57.131-1995), pp. 1–73, 2012.

[76] G. E. Mejia-Ruiz, M. R. Arrieta Paternina, J. M. Ramirez, Rodriguez-Rodriguez, J. R., R. Cardenas-Javier, and A. Zamora-Mendez, Decongestion of Active Distribution Grids via D-PMUs-based Reactive Power Control and Electric Vehicle Chargers. Flexibility in Electric Power Distribution , CRC Press, 2021.